



# Kondo effect and detection of a spin-polarized current in a quantum point contact

Deung Jang Choi

## ► To cite this version:

Deung Jang Choi. Kondo effect and detection of a spin-polarized current in a quantum point contact. Other [cond-mat.other]. Université de Strasbourg, 2012. English. NNT: 2012STRAE029. tel-00862415

**HAL Id: tel-00862415**

**<https://theses.hal.science/tel-00862415>**

Submitted on 16 Sep 2013

**HAL** is a multi-disciplinary open access archive for the deposit and dissemination of scientific research documents, whether they are published or not. The documents may come from teaching and research institutions in France or abroad, or from public or private research centers.

L'archive ouverte pluridisciplinaire **HAL**, est destinée au dépôt et à la diffusion de documents scientifiques de niveau recherche, publiés ou non, émanant des établissements d'enseignement et de recherche français ou étrangers, des laboratoires publics ou privés.

# Kondo effect and detection of a spin-polarized current in a quantum point contact

Thèse présentée par

Deung-Jang CHOI

Pour obtenir le titre de Docteur de l'Université de Strasbourg

1 Juin 2012

Commission d'examen:

Prof.	Nicolás Lorente	Rapporteur externe
Prof.	Jörg Kröger	Rapporteur externe
Dr.	Hélène Bouchiat	Examineur
Prof.	Mario Ruben	Examineur
Prof.	Jean-Pierre Bucher	Directeur de thèse
Dr.	Marc Drillon	President du Jury
Dr.	Laurent Limot	Invité

Institut de Physique et Chimie des Matériaux de Strasbourg















# Résumé

Au début des années trente, un comportement singulier fût mis en évidence dans la résistance électrique d'un métal alors qu'il était refroidi en dessous d'une certaine température. A l'époque il était bien établi que l'interaction électron-phonon et l'interaction électron-électron étaient progressivement figées à température décroissante, la résistance d'un métal étant alors essentiellement gouvernée par une contribution résiduelle et constante due à des défauts et des impuretés. L'augmentation de résistance observée pour un métal d'or présentant des impuretés de fer était donc fort surprenante [1]. Ce n'est qu'en 1964 que Jun Kondo proposa une explication pour ce phénomène [2, 3]. En utilisant un modèle comprenant l'interaction d'échange entre le spin de l'impureté magnétique et les spins des électrons de conduction du métal hôte, il démontra par un traitement perturbatif au second ordre que la résistivité d'un métal devait augmenter logarithmiquement en dessous d'une température critique. Aujourd'hui cet effet porte le nom d'effet Kondo. L'augmentation logarithmique de la résistivité est associée à un écrantage de l'impureté magnétique par les spins des électrons de conduction du métal hôte et est donc un phénomène à N-corps impliquant des corrélations électron-électron. L'effet Kondo a été également mis en évidence par des mesures de susceptibilité et de chaleur spécifique, ou par des mesures thermoélectriques [4].

En 1998 l'effet Kondo a été observé pour la première fois dans un objet individuel, plus précisément dans une boîte quantique. Une boîte quantique est une nanostructure semi-conducteur détenant un nombre pair ou impair d'électrons [5, 6]. Le fort confinement tridimensionnel des porteurs de charges dans une boîte quantique conduit notamment à l'observation d'une densité d'états électroniques discrète, ainsi une boîte quantique est souvent considérée comme un "atome artificiel". Lorsqu'une boîte quantique interagit avec des électrodes métalliques, l'effet Kondo peut se manifester dans le transport électronique par l'émergence dans la densité d'états électroniques d'une résonance au niveau de Fermi, connue sous le nom de résonance d'Abrikosov-Suhl-Kondo (ASK). Cette résonance est associée à un nombre impair d'électrons présent dans

la boîte, l'électron non apparié produisant l'effet Kondo avec les électrons de conduction des électrodes. C'est aussi en 1998 que l'effet Kondo a été observé sur un atome individuel adsorbé sur une surface en exploitant un microscope à effet tunnel (STM) [7, 8]. L'amplitude de la résonance ASK est maximale lorsque la pointe du STM est positionnée au dessus de l'atome magnétique, mais disparaît lorsque la pointe est positionnée au dessus de la surface métallique non-magnétique.

L'effet Kondo observé dans des objets individuels constitue un système modèle pour l'étude de corrélations électroniques. Ces dernières jouent un rôle moteur dans le domaine émergent de l'électronique de spin (ou spintronique) où l'utilisation d'atomes issus des terres rares et des métaux de transition est incontournable. Dans ce contexte, l'étude de l'interaction d'une impureté Kondo avec des électrodes ferromagnétiques [9] ou avec d'autres impuretés magnétiques [10] peut donc s'avérer fondamental pour la spintronique. L'effet Kondo d'une impureté est sensible à son environnement magnétique car en présence d'interactions magnétiques la résonance ASK se dédouble. Dans une certaine mesure, la résonance ASK agit comme un niveau atomique discret doublement dégénéré qui subit un dédoublement Zeeman en présence d'un champ magnétique ou plus généralement d'un champ magnétique effectif. Inversement, la détection d'un dédoublement Zeeman indique l'existence d'un champ magnétique. Dans une boîte quantique, le couplage de la boîte avec les deux électrodes est en général faible ainsi la largeur de la résonance ASK est de l'ordre de quelques meV. Beaucoup d'études de l'effet Kondo en présence d'interactions magnétiques ont été menées sur les boîtes quantiques, grâce notamment au contrôle qui peut être exercé sur la résonance ASK, mais aussi grâce au faible élargissement de la résonance qui peut alors être dédoublée avec un champ magnétique de l'ordre de 10 Tesla ou moins. A ces études, s'ajoutent de nombreux travaux similaires menés avec des dispositifs tels des jonctions cassées comprenant une molécule individuelle jouant le rôle de l'impureté magnétique [11]. En revanche, peu d'études de ce type ont été consacrées aux atomes individuels. Cela est dû à l'hybridation plus marquée entre l'impureté atomique et la surface comparée aux boîtes quantiques, qui entraîne une largeur typique de 10 meV ou plus pour la résonance ASK. Un champ magnétique d'environ 100 T ou plus est alors nécessaire afin le dédoublement de la résonance. Ceci est donc en pratique difficile à mettre en œuvre.

Cette thèse est consacrée précisément à l'étude via un STM de l'interaction entre un atome Kondo et son environnement magnétique. Une nouvelle stratégie est adoptée ici par rapport aux études antérieures de ce genre. Tout d'abord, nous éliminons la barrière tunnel en établissant un contact pointe-atome. Nous formons ainsi un point de contact quantique comprenant

une seule impureté Kondo. Deuxièmement, nous utilisons des pointes ferromagnétiques. Le contact pointe-atome permet de sonder l'influence du ferromagnétisme sur l'impureté Kondo via l'observation de la résonance ASK. La géométrie du point de contact permet tout particulièrement de produire une densité de courant polarisée en spin suffisamment élevée pour qu'elle entraîne un dédoublement de la résonance ASK. Ce dédoublement constitue la première observation à l'échelle atomique d'un phénomène connu sous le nom d'accumulation de spin, laquelle se trouve être une propriété fondamentale de la spintronique.

Le plan de ce mémoire est le suivant :

**Le Chapitre 1** est consacré à l'effet Kondo. Après une introduction générale de l'effet Kondo, nous nous focalisons sur l'impact que peut avoir un environnement magnétique sur cet effet. Nous rappelons ensuite quelques résultats expérimentaux obtenus avec des boîtes quantiques ou des jonctions cassées en présence d'un champ magnétique ou d'électrodes ferromagnétiques. Enfin, nous concluons le chapitre en présentant brièvement l'effet Kondo pour un système à deux impuretés Kondo, en montrant comment le couplage magnétique entre impuretés peut affecter la résonance ASK.

**Le Chapitre 2** présente une description générale du STM : son principe de fonctionnement, l'imagerie et la spectroscopie. Nous montrons aussi brièvement comment nous avons préparé les pointes et les échantillons utilisés au cours de cette thèse. Dans la deuxième partie du chapitre, nous revenons sur l'existence d'une interférence de Fano dans les mesures STM et montrons comment interpréter la forme de la résonance ASK. Enfin nous verrons pourquoi le STM est une technique adéquate pour sonder les propriétés des deux impuretés Kondo couplées magnétiquement.

**Le Chapitre 3** met l'accent sur les points de contacts quantiques, c'est-à-dire des jonctions métalliques comprenant un seul atome. Après une brève présentation du transport quantique dans les contacts comprenant un seul atome, nous explorons la façon de construire ce type de jonction avec le STM. Nous détaillons ensuite le premier résultat marquant de cette thèse obtenu en utilisant une jonction comprenant un atome de Co en contact avec une pointe à sommet en cuivre et une surface de Cu(100). Une résonance ASK est mise en évidence dans la conductance différentielle, dont la largeur varie de façon exponentielle avec le courant balistique



et indépendamment de la structure de la pointe utilisée. Par une description théorique basée sur le modèle d'Anderson, nous montrons que l'effet Kondo et la conductance de la jonction sont liés via les relaxations atomiques présentes dans le proche environnement de l'atome de cobalt.

**Le Chapitre 4** présente le résultat central de la thèse. Une pointe ferromagnétique est employée afin d'étudier comment la résonance ASK d'un atome de Co évolue en présence d'un courant polarisé en spin et d'un couplage direct ferromagnétique. Tout d'abord, nous éliminons le couplage direct ferromagnétique entre l'atome et la pointe magnétique, en introduisant un espaceur de cuivre non magnétique entre les deux. La jonction ainsi formée correspond donc à un dispositif à magnetorésistance géante (GMR). L'observation du dédoublement de la résonance ASK démontre la présence d'accumulation de spin sur le site de Co. Par contre, le dédoublement de la résonance ASK disparaît lorsqu'on élimine l'espaceur de cuivre. Bien que le couplage direct ferromagnétique renforce en principe le dédoublement de la résonance Kondo, nous montrons que la nature chimique du couplage entre le cobalt et la pointe magnétique entraîne une diminution conséquente de l'accumulation de spin. Ainsi, le ferromagnétisme et l'accumulation de spin ne suffisent plus à dédoubler la raie Kondo, et une "restauration" de l'effet Kondo a donc lieu via les relaxations atomiques. Par cette étude, nous apportons ainsi des nouveaux éléments permettant une meilleure compréhension des travaux récents de Calvo et al. [12]. Ces derniers avaient démontré l'existence de l'effet Kondo dans des contacts ferromagnétiques de taille atomique.

**Le Chapitre 5** est plus prospectif. Nous nous intéressons dans ce chapitre à une pointe fonctionnalisée par une molécule afin de montrer son intérêt potentiel pour la physique Kondo. Récemment, des pointes de ce genre construites avec des molécules telles que CO ou H<sub>2</sub> ont été employées afin d'améliorer la résolution spatiale du STM [12]. Nous présentons ici une des premières études spectroscopiques réalisées avec une pointe moléculaire. Nous montrons comment le tunneling entre une pointe de C<sub>60</sub> et les états de surface de Shockley de Cu(111) peuvent produire une conductance différentielle négative (NDC), dont l'amplitude peut être contrôlée par l'épaisseur de la barrière tunnel ou l'orientation du C<sub>60</sub>. L'orientation affecte la NDC via des règles de sélection dictées par la symétrie du C<sub>60</sub> et les états électroniques de surface. Avec le savoir-faire acquis, nous montrons ensuite comment ces pointes moléculaires peuvent être utilisées afin de détecter l'effet Kondo en régime tunnel et en régime de contact.





# Contents

<b>Introduction</b>	<b>1</b>
<b>1 Kondo effect and magnetism</b>	<b>5</b>
1.1 Kondo effect of an atomic impurity . . . . .	6
1.2 Kondo effect in a quantum dot . . . . .	11
1.3 Kondo effect and magnetic interactions . . . . .	14
1.3.1 Zeeman splitting . . . . .	14
1.3.2 The proximity of ferromagnetic leads . . . . .	16
1.3.3 Two-Kondo impurity problem . . . . .	18
Summary and conclusions . . . . .	22
<b>2 Scanning tunneling microscopy and spectroscopy</b>	<b>25</b>
2.1 Experimental setup . . . . .	25
2.1.1 STM in UHV . . . . .	26
2.1.2 Tip and sample preparation . . . . .	28
2.2 Principle . . . . .	30
2.3 Spectroscopy . . . . .	34
2.4 Detection of the Kondo resonance with STM . . . . .	36
2.4.1 Kondo effect of adsorbed magnetic atoms . . . . .	37
2.4.2 Kondo effect with two atoms . . . . .	42
Summary and conclusions . . . . .	43
<b>3 Conductance-driven Kondo effect in a single cobalt atom</b>	<b>45</b>
3.1 Quantum point contacts . . . . .	45
3.1.1 Conductance of a single atom using STM . . . . .	49

3.2	Atomic relaxations near point contact . . . . .	52
3.3	Conductance-driven change of the Kondo effect . . . . .	56
3.3.1	Contact conductance over a Co adatom on Cu(100) . . . . .	57
3.3.2	Evolution of the Fano line shape . . . . .	59
3.3.3	The relation between $T_K$ and $G$ . . . . .	60
3.3.4	Heating effects . . . . .	66
	Summary and conclusions . . . . .	70
<b>4</b>	<b>Spin-polarized currents at a single Kondo impurity</b>	<b>71</b>
4.1	Spintronics: a brief overview . . . . .	72
4.2	Spin injection and detection with a Kondo impurity . . . . .	77
4.2.1	Junction fabrication . . . . .	78
4.2.2	Spin- versus structure-related properties . . . . .	79
4.2.3	Role of the RKKY interaction . . . . .	83
4.2.4	Ferromagnetism and chemistry . . . . .	84
4.2.5	Model calculation: Equation of motion . . . . .	86
4.3	Comparison with previous studies . . . . .	89
	Summary and conclusions . . . . .	92
<b>5</b>	<b>Kondo effect in a molecular junction</b>	<b>95</b>
5.1	The $C_{60}$ terminated tip . . . . .	96
5.2	Spectroscopy with a molecular tip: Controlling NDC . . . . .	101
5.2.1	Influence of molecular orientation . . . . .	102
5.2.2	WKB simulation and selection rules . . . . .	106
5.3	Evolution of the Kondo resonance in a $C_{60}$ -Co contact . . . . .	109
5.3.1	Conductance of the $C_{60}$ -Co junction . . . . .	110
5.3.2	Impact of the molecular tip on the Kondo resonance . . . . .	112
	Summary and conclusions . . . . .	114
	<b>Conclusion and perspectives</b>	<b>117</b>
	<b>Bibliography</b>	<b>121</b>
	<b>List of figures</b>	<b>137</b>

<b>Curriculum Vitae</b>	<b>141</b>
<b>List of publications</b>	<b>143</b>
<b>List of presentations</b>	<b>145</b>



# Introduction

In the early thirties, an electrical resistance of a metal was shown to have a singular behavior while it was cooled down beyond a certain temperature. At the time, it was well understood that atomic vibrations are progressively frozen in a metal when the temperature is reduced, showing a decrease of a resistance and finally a residual resistance due to structural defects and impurities. An increase in a resistance with decreasing temperature was instead observed in a gold metal with iron impurities [1]. This is the first experimental observation of an upturn in the resistance at low temperature in a metal with embedded magnetic impurities. In 1964, Jun Kondo theoretically solved this observation [2, 3]. He gave an explanation with a  $s$ - $d$  model which includes the exchange interaction between the spin of the magnetic impurity and the spins of the conduction electrons of the host metal. The model proposed a logarithmic increase of the resistivity below a critical temperature in a second order perturbation theory. Nowadays this effect is the so-called Kondo effect. The logarithmic increase of the resistivity is associated to the screening of the magnetic impurity by the spins of the conduction electrons in the host metal and is therefore a many-body phenomenon involving electron-electron correlations. The Kondo effect was also evidenced by studying not only the resistivity but also the susceptibility, the specific heat, and the thermoelectric power of a non-magnetic host metal with magnetic impurities [4].

In 1998, the first experimental observation of the Kondo effect in a single object was obtained using a quantum dot (QD), a so-called artificial atom which is a semiconductor box holding even or odd number of electrons [5, 6]. The Kondo effect of a QD bridging two metallic leads is detected through transport measurements and corresponds to a zero-bias resonance, also known as an Abrikosov-Suhl-Kondo (ASK) resonance. The QD is controlled by the voltage on the gate electrodes which allows adjusting the number of electrons and therefore the parameters related to the ASK resonance. When an odd number of electrons is in the dot, the unpaired electrons can form a singlet state with the free conduction electrons in the leads and produce



the ASK resonance. In the same year, the ASK resonance was observed for the first time in a single magnetic atom adsorbed on a non-magnetic surface by scanning tunneling microscopy (STM) [7, 8]. The amplitude of the resonance is maximum when positioning the tip above the center of the single atom and is progressively lost when moving away laterally.

The Kondo effect of these single objects represents a model system to study electron correlations, which are nowadays of importance in relation to the emerging field of spin electronics, also known as spintronics, where chemical elements with partially filled  $d$  or  $f$  shells play a central role. Also of particular interest to spintronics is the interaction of single Kondo impurities with ferromagnetic leads [9] or with other magnetic impurities [10]. A Kondo impurity is in fact sensitive to its magnetic environment as the ASK resonance is usually split into two resonances in the presence of magnetic interactions. To some extent, the ASK resonance acts as a two-fold degenerate energy level of an atom which undergoes a Zeeman splitting in the presence of an effective magnetic field. Conversely, the detection of a Zeeman splitting indicates the existence of a magnetic field. In a QD, the coupling of the QD to the two leads is very weak in general, and the Kondo resonance is in the range of a few meV. Many studies focusing on magnetic interaction have been carried out on QDs, due to the high control that can be extended to the ASK resonance and its low energy range, allowing to split the resonance with a magnetic field of  $\sim 10$  T. Similar work has also been carried out in single-molecule or lithographically-defined devices [11].

Although STM is an ideal tool to study the Kondo effect of single atoms, there is still a strong lack of experimental studies concerning atoms in the presence of magnetic interactions. This is partly due to the stronger impurity-metal hybridization compared to QDs, which places the ASK width in the range of 10 meV. An effective magnetic field of  $\sim 100$  T would be needed to split the resonance. The present Thesis is devoted precisely at studying the interaction between a single Kondo impurity with its magnetic environment through STM. A new strategy is adopted here compared to former studies of this kind. Firstly, we contact a single-magnetic atom on a surface with a STM tip thereby eliminating the vacuum barrier. Secondly, we use ferromagnetic tips. The contact with a single atom allows probing the influence of ferromagnetism on the Kondo impurity *i. e.* its ASK resonance. But most importantly, the contact geometry produces sufficiently high current densities compared to the tunneling regime, so that the ASK resonance becomes sensitive to the presence of a spin-polarized current. This constitutes the first atomic scale detection of a spin-polarized current with a single Kondo impurity.

The outline of the thesis is as follows:

**Chapter 1** includes a general introduction of the Kondo effect, with a particular emphasis on how the magnetic surroundings of an impurity may impact its ASK resonance. We also present the well-known results obtained on QDs and recall studies with external magnetic fields and ferromagnetic leads. We will also briefly introduce the two-Kondo impurity problem.

**Chapter 2** introduces the experimental setup used and briefly shows how we prepare the tips and samples. The basic concepts of STM including its working principle, image acquisition and spectroscopy are then presented. In the spectroscopy section, we particularly focus on how the ASK resonance is detected in STM. Here, we present the model of Fano interference and recall some recent STM results obtained for two-Kondo impurity coupled magnetically.

**Chapter 3** will focus on quantum point contacts. After a brief presentation of the quantum transport in single atom contacts, we explore how to build these types of junctions with STM. We then detail the first important result of this Thesis in relation to the Kondo effect. We will deal with a junction comprising a Co atom bridging a copper-coated W tip and a Cu(100) surface. An ASK resonance is evidenced in the differential conductance of Co and its width is shown to vary exponentially with the ballistic conductance regardless of the tip structure. Using a theoretical description based on the Anderson model, we show that the Kondo effect and the conductance are related through the atomic relaxations affecting the environment of the Co atom.

**Chapter 4** presents the central results of the Thesis. A ferromagnetic tip is brought into contact with a single Co atom on Cu(100) in order to monitor how the ASK resonance changes in the presence of a spin-polarized current and ferromagnetism. Before using the ferromagnetic tip, we first cover the magnetic tip with a non-magnetic material in order to eliminate the ferromagnetic direct coupling between the atom and the tip apex. The junction formed with such a tip corresponds to a rudimentary giant magneto-resistance (GMR) structure. The splitting of the Kondo resonance observed with this tip is then assigned to a spin-polarized current flowing across the non-magnetic material. This phenomenon corresponds to spin accumulation, which is a fundamental property of spintronics. The ASK resonance is instead “restored” using a pristine ferromagnetic tip. We will show in fact that spin accumulation decreases dramatically when the Co atom is in direct contact with the magnetic tip, and that the ferromagnetic coupling is not sufficient to split the ASK resonance. These results shed some light on recent work by Calvo *et al.* [12] showing how Kondo physics can survive in a ferromagnetic atomic contact.

**Chapter 5** is more prospective. We focus here on a functionalized molecular C<sub>60</sub> tip and show how it may be potentially interesting for probing a Kondo system. Recently, functionalized

tips built by picking up molecules such as CO or H<sub>2</sub> have been employed to obtain an enhanced resolution in STM images [13, 14]. After presenting how to prepare and characterize a C<sub>60</sub> tip, we detail one of the first spectroscopic studies carried out with this kind of tip. Tunneling between a C<sub>60</sub> tip and the Shockley surface states of copper is shown to produce negative differential conductance (NDC) that can be tuned through barrier thickness or C<sub>60</sub> orientation up to complete extinction. The orientation dependence of NDC is a result of a symmetry matching between the molecular tip and the surface states. With the know-how acquired, we then show how a C<sub>60</sub>-terminated tip can be used to detect and alter the Kondo effect of Co on Cu(100). This work is a prerequisite for studying molecular point contacts exhibiting a Kondo effect.

## CHAPTER 1

# Kondo effect and magnetism

Noble metals, like copper and gold, remain conducting and have a constant finite resistance, even at the lowest accessible temperatures. The value of the low-temperature resistance depends on the number of defects in the material. However, this behavior changes dramatically when magnetic atoms, such as cobalt, are added. Rather than saturating, the electrical resistance increases as the temperature is lowered further [1]. The so-called Kondo temperature —the temperature at which the resistance starts to increase again— completely determines the low-temperature electronic properties of the material. Since the 1930s there have been many observations of an anomalous increase in the resistance of metals at low temperature. Yet it took until 1964 for a satisfactory explanation to appear.

In this chapter, we introduce the Kondo effect by briefly recalling the Anderson and Kondo models describing the electronic properties of a magnetic impurity embedded in a host non-magnetic metal (Section 1.1). The second part of this Chapter is dedicated to experimental results of the Kondo effect obtained on single objects interacting with a magnetic environment. More specifically, we focus on the detection of the so-called Abrikosov-Suhl-Kondo (ASK) resonance in the conductance of quantum dots or of single molecules coupled to metallic leads (Section 1.2). Results obtained with the Scanning Tunneling Microscope will instead be detailed in Chapter 2. The impact of magnetism on the Kondo effect is described in Section 1.3. Changes induced by an external magnetic field on the Kondo resonance are presented in Section 1.3.1, while the role of ferromagnetism and of magnetic interactions are outlined in Sections 1.3.2 and 1.3.3, respectively.

## 1.1 Kondo effect of an atomic impurity

The theoretical framework for understanding the Kondo effect emerged in the late 1960s from the work of P. W. Anderson on magnetic impurities in metals [15]. If a dilute alloy is formed by dissolving a small number of magnetic atoms in a metallic matrix, it is often found that the impurity has a net magnetic moment arising from the  $d$ -shell valence electrons of the impurity. The impurity has a localized magnetic state and affects the electronic properties of alloy. To describe this phenomenon, Anderson proposed a simple mechanism, namely the  $s - d$  mixing. Assuming a local magnetic moment exists on the impurity in a metal, Anderson introduced a single  $d$ -orbital level of energy  $\epsilon$  for a magnetic impurity below the Fermi level ( $E_F$ ) which is filled with a  $S = 1/2$  spin-up electron [Fig. 1.2(b)]<sup>1</sup>. A spin-down electron which would like to occupy the same level sees the repulsive Coulomb interaction,  $U$ , of the spin-up electron already occupying the level. Therefore only an  $\epsilon + U$  level is available for the spin-down electron. As long as this level is above  $E_F$ , the impurity has a net magnetic moment as shown in Fig. 1.1(a), but this can change due to the hybridization of the  $d$ -shell with the metal  $s$ -states. In the Anderson model, the Hamiltonian for a single localized  $d$  orbital with the conduction band is then given as following

$$H_{Anderson} = H_{cond} + H_{imp} + H_{kd} = \sum_{k\sigma} \epsilon_k c_{k\sigma}^\dagger c_{k\sigma} + \sum_{\sigma} \epsilon d_{\sigma}^\dagger d_{\sigma} + U n_{d\uparrow} n_{d\downarrow} + \sum_{k\sigma} \left( V_{kd} d_{\sigma}^\dagger c_{k\sigma} + V_{kd}^* c_{k\sigma}^\dagger d_{\sigma} \right). \quad (1.1)$$

The first term, corresponding to  $H_{cond}$ , is the unperturbed energy of the free-conduction electrons in a metal,  $\epsilon_k$  is the energy of the free-electron state of momentum  $k$ , and  $c_{k\sigma}$  ( $c_{k\sigma}^\dagger$ ) denotes the destruction (creation) operator for momentum  $k$  and spin  $\sigma$ . The second and third terms for  $H_{imp}$  are the unperturbed energy of a  $d$  state of the magnetic impurity;  $\epsilon$  is the one-electron energy of a localized  $d$  orbital and  $d_{\sigma}$  ( $d_{\sigma}^\dagger$ ) accounts for the destruction (creation) operator for spin  $\sigma$ . The third term represents the Coulomb repulsion between opposite-spin electrons on the  $d$  orbital. The last term,  $H_{kd}$ , is for the  $s - d$  interaction describing the tunneling from the  $s$  band of the free electrons to a  $d$  orbital of the impurity and vice versa. The strength of  $s - d$  coupling,  $V_{kd}$ , mixes the electron in the localized magnetic level with the conduction electrons in a metal resulting in a shift and a broadening of the spin-up and

<sup>1</sup>This model has been generalized to apply to the more realistic case where there are many degenerate  $d$  levels present, although, for simplicity, the orbital angular momentum has usually been assumed to be completely quenched.

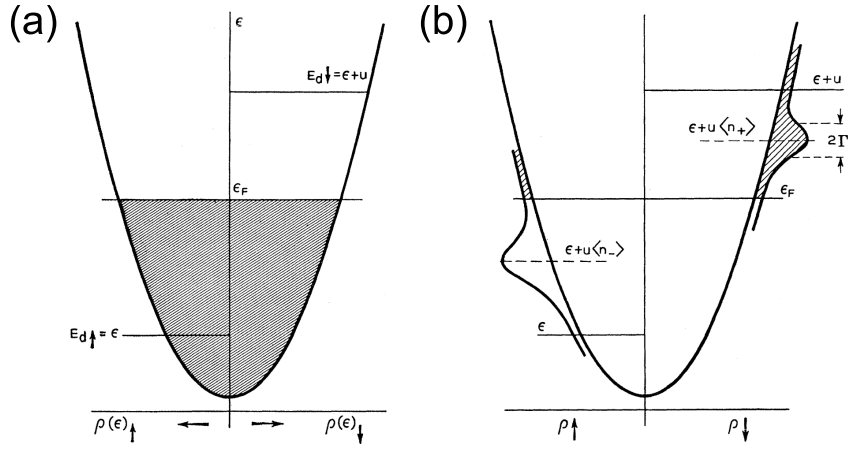


Figure 1.1: The energy levels without and with  $s-d$  mixing. (a) The unperturbed energy level without  $s-d$  admixture. The shaded area corresponds to the occupied states. (b) The density of states with  $s-d$  mixing. The localized spin-up and down magnetic levels have a width of  $2\Gamma$  and are shifted. The broadening decreases the occupation of the spin-up  $d$ -level (unoccupied area, dashed on figure), while it increases the occupation of the spin-down  $d$ -level [15].

spin-down energy levels [Fig. 1.1(b)]. The half width at half maximum of the impurity  $d$  state,  $\Gamma$ , due to the hybridization with the conduction electrons of the host metal is given as

$$\Gamma = \pi \rho_0 |V_{kd}|_{av}^2 \quad (1.2)$$

for the average over  $k$  states at  $E_F$ ;  $\rho_0$  is the density of state (DOS) of the metal at  $E_F$ . Due to  $s-d$  mixing, the spin-up high-energy tail is pushed above  $E_F$ , thereby reducing the occupation level, while the spin-down level sees its occupancy increase. If the  $s-d$  mixing is strong enough to align the spin-up and spin-down energy levels, the local magnetic moment no longer exists.

In 1964, J. Kondo introduced the  $s-d$  exchange-interaction model to explain the Kondo effect, which includes a scattering from a magnetic impurity interacting with the conduction electrons of a host metal [2, 3]. The Kondo Hamiltonian is written as

$$H_{Kondo} = H_{cond} + H_{imp} + H_{ex}, \quad (1.3)$$

where the  $s-d$  mixing term  $H_{kd}$  in the Anderson model is replaced by the exchange interaction Hamiltonian  $H_{ex}$ . Assigning a spin  $\mathbf{S}$  to the magnetic impurity, the  $H_{ex}$  term can be expressed

as

$$H_{ex} = JS \cdot \mathbf{s} = -\frac{J}{2N} \sum_{k,k'} \left[ (c_{k'\uparrow}^\dagger c_{k\uparrow} - c_{k'\downarrow}^\dagger c_{k\downarrow}) S_z + c_{k'\uparrow}^\dagger c_{k\downarrow} S_- + c_{k'\downarrow}^\dagger c_{k\uparrow} S_+ \right] \quad (1.4)$$

where  $J$  is the amplitude of the effective  $s-d$  exchange interaction, which is antiferromagnetic.  $\mathbf{s}$  is the spin density operator of the conduction electrons and  $\mathbf{S}$  denotes for the spin-1/2 impurity. Using a destruction (creation) operator of conduction electrons,  $c_{k\sigma}$  ( $c_{k\sigma}^\dagger$ ), a matrix containing  $N$  atoms can be written as well where  $k$  and  $k'$  are the initial and final momenta of the exchange interacting electrons and  $S_\pm$  are the raising or lowering operators of  $\mathbf{S}$ . The  $S_+$  operator changes the spin of the magnetic impurity from a down to an up state, while the  $c_{k'\downarrow}^\dagger c_{k\uparrow}$  operator changes the spin of a conduction electron from up to down. The  $S_-$  operator changes instead the spin of the magnetic impurity from an up to down state, while the  $c_{k'\uparrow}^\dagger c_{k\downarrow}$  operator changes the spin of a conduction electron from down to up. The exchange term  $H_{ex}$  therefore describes a spin-flipping process between the local moment carried by the impurity and the spins of the  $N$  electrons. By applying a many-body perturbation theory [16], the Kondo Hamiltonian leads to a new electron state below a certain temperature now known as Kondo or Suhl-Abrikosov temperature ( $T_K$ ). The relation between  $J$  and  $T_K$  is then  $T_K \simeq (E_F/k_B) \exp(-1/|J|\rho_i)$  where  $\rho_i$  is the DOS of  $i$ -th spin in a host metal at  $E_F$ . The many-body ground state comprises the impurity spin and a correlated “cloud” of conduction electrons screening a magnetic moment of the impurity. The ground state is doubly degenerate and can be expressed as a linear combination  $1/\sqrt{2}(|\downarrow, \uparrow\rangle - |\uparrow, \downarrow\rangle)$  of the two states  $|\downarrow, \uparrow\rangle$  and  $|\uparrow, \downarrow\rangle$  [Fig. 1.2(a)], where  $\uparrow$  and  $\downarrow$  are the spin orientations of the impurity, while  $\uparrow$  and  $\downarrow$  are the spin orientation of the conduction electrons. The typical extension of the cloud is  $\lambda_F E_F / (k_B T_K)$  ( $\lambda_F$ : Fermi wavelength), which then varies with the nature of the impurity and of the host metal—it is around 40 nm for Co in copper [17–19]. Although the Kondo cloud has never been observed in experiments, it is however responsible for raising electron scattering below  $T_K$  and for the associated logarithmic increase of the resistance.

In 1966, J. R. Schrieffer and P. A. Wolff introduced a canonical transformation in the limit of small  $s-d$  mixing to link the Anderson and Kondo models [20]. By a canonical transformation, the  $H_{kd}$  term of the Anderson Hamiltonian can be transformed to the  $H_{ex}$  term of the Kondo model. Assuming  $\Gamma/\epsilon \ll 1$ , the relation between  $J$  and  $V_{kd}$  is then

$$\frac{J}{N} = -2 \left[ \frac{|V_{kd}|_{av}^2 U}{(|\epsilon| \cdot |\epsilon + U|)} \right]. \quad (1.5)$$

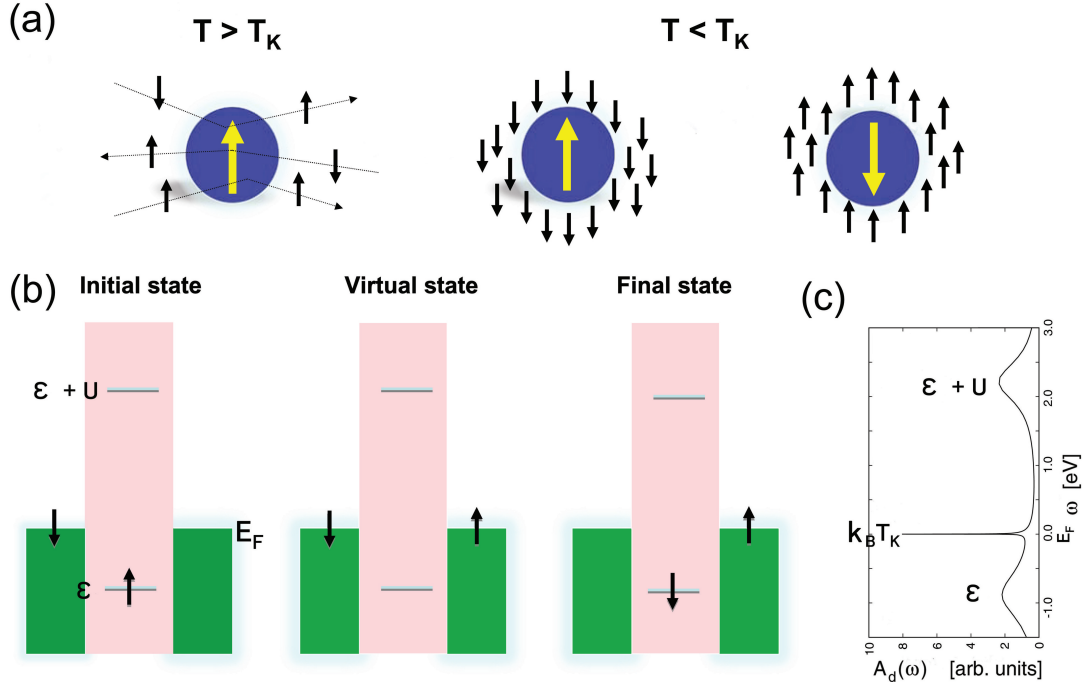


Figure 1.2: Schematics of the Kondo ground state and spin-flip process (a) Electron scattering by a magnetic impurity without screening above  $T_K$  and with screening below  $T_K$ . (b) Schematics of the Anderson model explaining how the spin of a magnetic impurity flips. The occupied  $d$  energy state  $\epsilon$  and unoccupied  $\epsilon + U$  are separated by the Coulomb repulsion  $U$  (adapted from [23]). (c) DOS of a magnetic impurity which contains occupied and unoccupied  $d$ -energy levels as well as the Kondo resonance at the Fermi level (adapted from [24]).

$J$  is  $\sim 1$  eV [21] and has negative value ( $J < 0$ ) due to the antiferromagnetic coupling between the magnetic impurity and the conduction electrons. In 1978, F.D.M. Haldane introduced  $T_K$  using the parameters from the Anderson model by a scaling theory [22]. The scaling theory applied to the Anderson model gives  $T_K$  as

$$T_K = \sqrt{\Gamma U/2} \exp \left[ -\frac{\pi \epsilon (\epsilon + U)}{2\Gamma U} \right]. \quad (1.6)$$

The Kondo ground state results also in the emergence of a resonance in the DOS at the impurity site, which is also known as the Abrikosov-Suhl-Kondo (ASK) resonance [Fig. 1.2(c)]. This resonance may be interpreted as follows. The conduction electrons in a metal pair up with the spin of the local magnetic moment through spin-flip events. These occur in a three-step



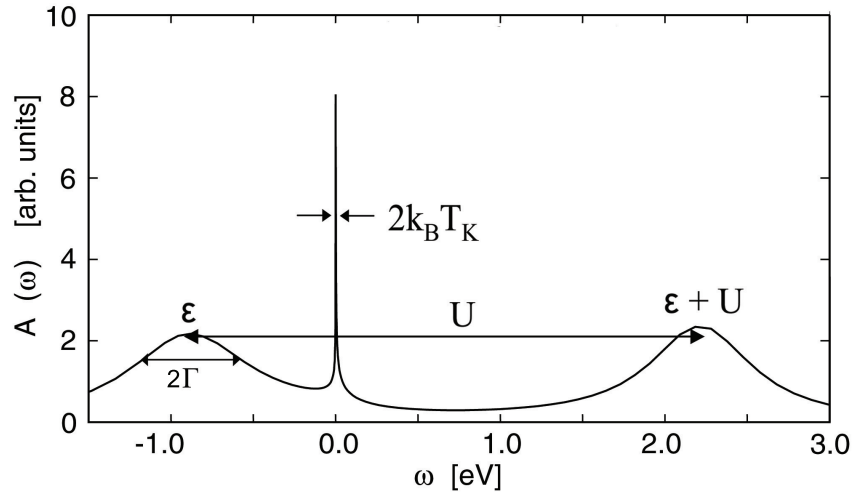


Figure 1.3: The spectral function of a Kondo impurity at  $T = 4$  K [24]. The occupied level lies at  $\epsilon$  ( $\epsilon < 0$ ) and has a broadening of  $2\Gamma$  due to the hybridization with the conduction band. The unoccupied level is at  $\epsilon + U$ . The Kondo resonance is shown near  $E_F$  with a width of  $2k_B T_K$ .

procedure depicted in Fig. 1.2(b), which sketches the spin-1/2 Anderson model. Classically, it is forbidden to the conduction electrons to jump from the impurity site to the conduction band states as  $\epsilon < E_F$ . However, in quantum mechanics, Heisenberg's uncertainty principle allows this excitation in the time scale of  $\hbar/\epsilon$ . Within this time scale, another electron from the Fermi sea must tunnel into the impurity site to fill the spin vacancy. Then, a virtual state is formed. In many quantum processes a virtual state is an intermediate state, sometimes described as "imaginary" in a multi-step process that mediates otherwise forbidden transitions. The spins are located on a virtual energy level near  $E_F$  and must anti-align to obey Hund's rule. As a result, the final spin state is opposite to the initial one, the spin of the impurity has flipped. The spin exchange processes necessarily produce an antiferromagnetic screening of the local magnetic moment as anticipated above for the sign of the coupling  $J$ . The ASK resonance in the impurity DOS corresponds to the spectral signature of the virtual discrete energy level hosting the two spins within the time scale  $\hbar/\epsilon$ . Figure 1.3 shows the spectral function of a magnetic impurity in a host metal. The Kondo resonance is located near  $E_F$  with a width of  $2k_B T_K$ . The left and right resonance correspond to the  $d$  (or  $f$ ) shells of the Anderson impurity [see Fig. 1.1] with broadening  $2\Gamma$  due to the hybridization with the conduction electrons.

The experimental observation of the Kondo effect in alloys with localized magnetic impurities

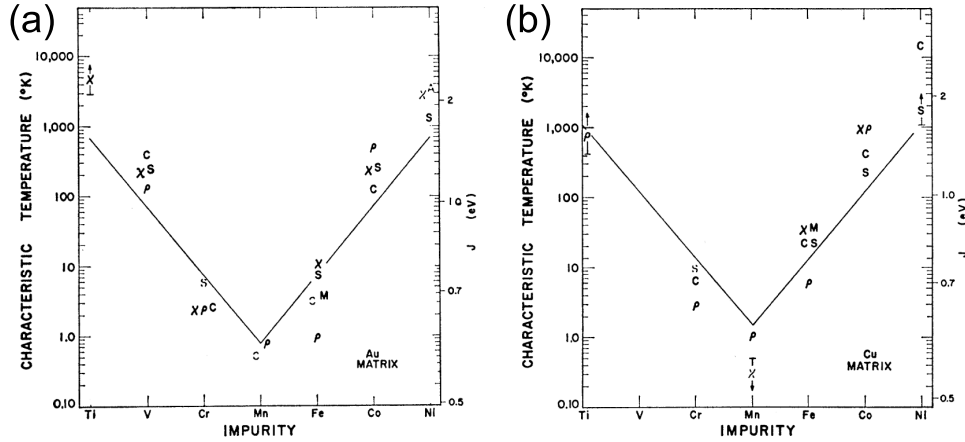


Figure 1.4: Characteristic Kondo temperature (left) and  $J$  (right) of transition elements in gold and copper. The Kondo temperature extracted from measurements of  $\chi$  (susceptibility),  $\rho$  (resistivity),  $C$  (specific heat),  $S$  (thermoelectric power),  $M$  (Mössbauer),  $A$  (infrared adsorption) are designated by a different symbol.  $J$  is calculated from  $T_K$  using  $\rho_0 = 0.15 \text{ eV}^{-1} \text{ atom}^{-1}$ . The line is obtained from Eq. (1.6). (a)  $T_K$  and  $J$  for transition elements diluted in gold, and (b) in copper [4].

are usually obtained by measuring the resistivity, the susceptibility or the specific heat. Figure 1.4 presents the striking experimental results of  $T_K$  with the first row transition elements diluted in gold or copper [4]. In this Thesis, we will deal exclusively with Co atoms on Cu surfaces which have a  $T_K \simeq 500 \text{ K}$  or lower.

## 1.2 Kondo effect in a quantum dot

Although thermodynamic and transport properties were studied in dilute alloys, there was no success in studying single molecular or atomic scale objects. However, thanks to developments in nanoscience, the experimental study of Kondo physics was revived in the late 1990s. The possibility of fabricating microscale or nanoscale devices allowed pioneering fundamental physics with artificial systems. The Kondo effect has been observed in devices such as lithographically defined quantum dots [5, 6], carbon nanotubes [25], and single molecules [26–30] coupled to metallic electrodes.

In 1998, the Kondo effect was observed for the first time in a quantum dot (QD) by two different groups. A QD is a nanoscale artificial semiconducting box in contact with metallic

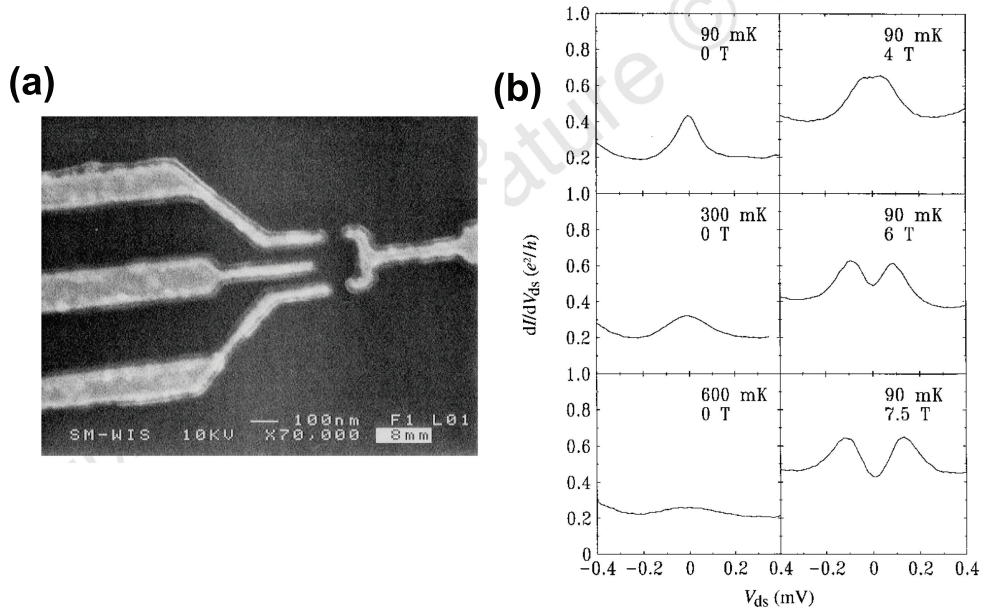


Figure 1.5: Schematic of a single-electron transistor and the zero-bias ASK resonance. (a) Top view image of a single-electron transistor. The dot is formed in the middle of the electrodes. The right electrode and the left lower and upper electrodes control the tunnel barrier of two-dimensional electron gas. The number of electrons in the droplet are adjusted through the gate electrodes (source and drain electrodes at the top and the bottom are not shown). The left middle electrode is used to change the energy of the dot. (b) The temperature (left) and magnetic field (right) dependence of the Kondo resonance. As the temperature increases, the resonance is progressively suppressed; when the magnetic field raises, the Kondo resonance is split into two peaks [5].

leads. A two-dimensional electron gas is confined in the dot and produces a DOS with discrete energy levels. The number of electrons in a QD can be adjusted by applying voltage to a gate electrode, so that the number of confined electrons in the dot can be controlled as odd or even. In the case of an odd number of electrons, the net spin of the dot is non zero. Goldhaber-Gordon *et al.* observed a Kondo effect in a single-electron transistor containing a GaAs/AlGaAs heterostructure [5]. Figure 1.5(a) shows a scanning electron micrograph of such a transistor. When a voltage is applied to the gate electrode, the conductance shows a periodic spacing of the peaks indicating a quantized number of electrons in the dot. When the number of electrons is odd in the droplet, an ASK resonance is detected near  $E_F$ . This indicates that a localized magnetic moment is present in the dot and that it interacts with the free conduction electrons in

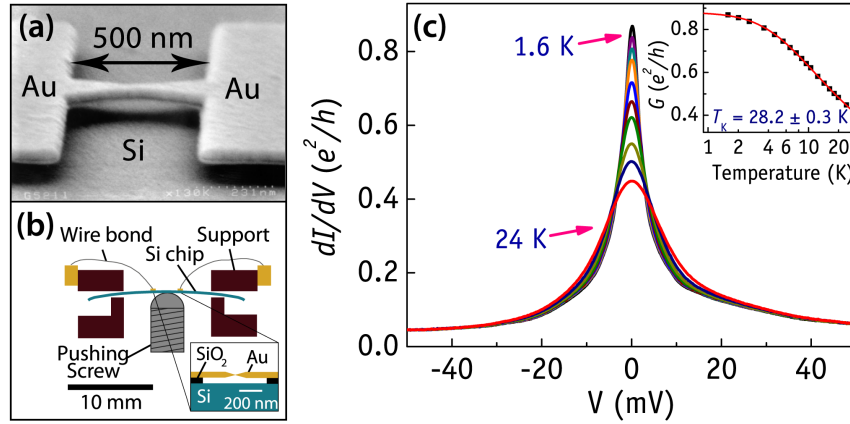


Figure 1.6: Schematics of a break junction and  $dI/dV$  spectra at various temperatures. (a) Scanning electron micrograph of Au electrodes suspended 40 nm above a Si substrate. (b) Schematic of the break junction apparatus. (c)  $dI/dV$  spectra at different temperatures. The inset shows a fit using Eq. (1.7) that yields  $T_K = 28.2 \pm 0.3$  K [29].

the leads. The QD therefore closely mimics the Kondo effect of a magnetic impurity embedded in a metal. Goldhaber-Gordon *et al.* also showed that the ASK resonance is suppressed when the temperature is increased, and that an external magnetic-field can produce a Zeeman splitting of the resonance [Fig. 1.5(b)]. As we show here after, these effects are both expected for the Kondo effect. Right after releasing this work, Cronenwett *et al.* also published the study of the Kondo effect in a QD [6]. By adjusting the number of electrons in the QD, they switched the Kondo effect on and off. They studied the temperature and the magnetic-field dependence and showed the influence of magnetic anisotropy by rotating the external magnetic field.

The width of a Kondo resonance in a QD is very narrow near  $E_F$  due to the low  $T_K$  which is normally a few hundred millikelvin. The observation of the ASK resonance in a QD requires a higher bias resolution compared to single molecule devices where  $T_K \sim 10$  K [Figs. 1.6(a) and 1.6(b)]. The reason of the lower  $T_K$  in a QD compared to single-molecule devices is due to the weaker confinement of electrons, which in turn decrease the Coulomb repulsion  $U$ , and following Eq. (1.6), also  $T_K$ . The Kondo temperature of all these systems remains, however, sufficiently low to study the temperature evolution of the ASK resonance. When the temperature is raised above  $T_K$ , thermal fluctuations wash out the spin coherence needed to produce spin-flip scattering events. Figure 1.6(c) presents the differential conductance at different temperatures in a Au-C<sub>60</sub>-Au mechanical controllable break junction, where the Kondo

effect is carried by the  $C_{60}$  molecule. The Kondo effect is progressively lost when increasing the temperature, which translates in a broadening of the ASK resonance and in a decreased resonance amplitude. Changes in amplitude with temperature can be expressed as [31]

$$G(T) = \frac{2e^2}{h} t \left[ 1 + \frac{T^2}{T_K^2} (2^{1/s} - 1) \right]^{-s} + G_{el} \quad (1.7)$$

with  $s = 0.22$ , while  $G_{el}$  accounts for a constant background. The free parameters  $T_K$ ,  $t$  and  $G_{el}$  are found by fitting the experimental data as shown in the inset of Fig. 1.6(c). As for the broadening, assuming a Lorentzian resonance, the full width at half maximum  $\Delta_K$  is approximately [32, 33]

$$\Delta_K = \sqrt{(\alpha k_B T)^2 + (2k_B T_K)^2} \quad (1.8)$$

where  $k_B$  is the Boltzmann constant,  $T$  is the working temperature and  $\alpha = 5.4$  [33]. When  $T \ll T_K$ , then  $\Delta_K \simeq 2k_B T_K$ .

## 1.3 Kondo effect and magnetic interactions

In recent years, the influence of magnetic interactions on the Kondo effect has been a great attraction for the researchers interested in studying spin-resolved phenomena, especially in relation to spin transport. The Kondo effect is in fact sensitive to the magnetic environment surrounding the impurity. We briefly present hereafter results obtained for the Kondo effect in the presence of an external magnetic field, of ferromagnetic leads, and for interacting magnetic impurities.

### 1.3.1 Zeeman splitting

The Kondo ground state is degenerate for spin up and down states. When an external magnetic field is applied to the Kondo system in a same direction as  $\uparrow$ , the spin of the impurity aligns with the external field so that the  $|\uparrow, \downarrow\rangle$  ground state is energetically favored with respect to  $|\downarrow, \uparrow\rangle$ . The twofold degeneracy is lifted and the Kondo resonance is split into two peaks by a Zeeman interaction. The two peaks are separated by  $\Delta_Z$ , which for a spin-1/2 impurity can be expressed by ( $\Delta_Z \ll T_K$ ):

$$\Delta_Z = 2g\mu_B H, \quad (1.9)$$

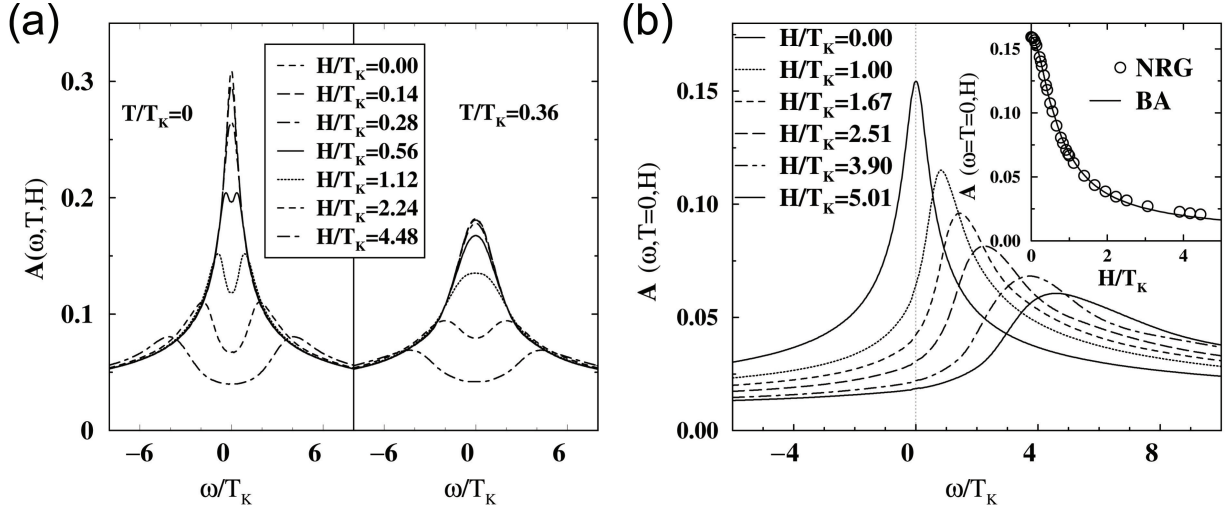


Figure 1.7: Calculated splitting of the Kondo resonance from Ref. [34]. (a) Evolution of the Kondo resonance with different magnetic fields for  $T/T_K = 0$  (left) and  $T/T_K = 0.36$  (right).  $A$  corresponds to the impurity spectral density function. While the Kondo resonance clearly splits apart at  $T = 0$ , the splitting is not detected at  $T/T_K = 0.36$  due to the broadened width of the resonance by the increased temperature [Eq. (1.8)]. (b) The spin-down component of the Kondo resonance at  $T = 0$  for different magnetic fields. The inset shows the comparison of numerical renormalization group (NRG) and Bethe-Ansatz (BA) calculations.

where  $g$  is the gyromagnetic factor,  $\mu_B$  is the Bohr magneton and  $H$  is the magnetic field [35]. Figure 1.7(a) presents the Kondo resonance-splitting with increasing magnetic field at given temperatures [34]. The Zeeman splitting is only discernible under critical values of temperature and magnetic field ( $H_c$ ). T.A. Costi found that  $H_c$  is approximately half of  $T_K$  at  $T = 0$ , *i.e.*  $H_c(T = 0) \approx 0.5T_K$  and is increasing linearly with temperature  $H_c \approx 3T$  at  $T > 0$ . When  $H$  is increased, the line shape of the resonance becomes asymmetric as shown in Fig. 1.7(b) for the spin down component of the Kondo resonance. As an example of an experimental realization, we present in Fig. 1.8(a) the Kondo effect of a molecular break junction device [26]. In this study, Park *et al.* showed that a Co ion bonded to polypyridyl ligands with the different lengths of insulating tethers,  $[\text{Co}(\text{tpy}-(\text{CH}_2)_5\text{-SH})_2]^{2+}$  and  $[\text{Co}(\text{tpy-SH})_2]^{2+}$ , presents a Zeeman-split ASK resonance with an external magnetic field in the  $dI/dV$ . The splitting amplitude may be tuned by changing the magnetic moment of the molecule via the gate electrode [Fig.1.8(b)], while changes of  $\Delta_Z$  with  $H$  yield a  $g$  factor close to 2 [Fig.1.8(c)].

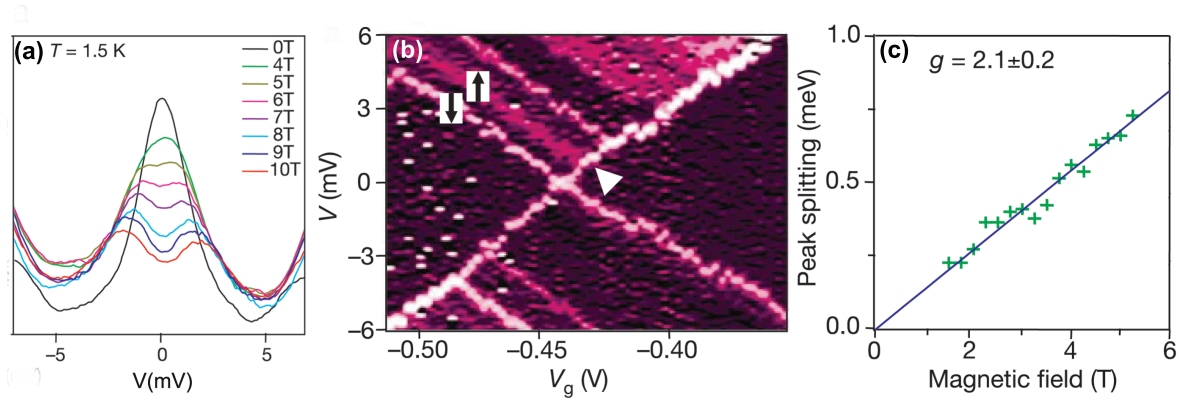


Figure 1.8: Zeeman splitting of a molecular Kondo device from Ref. [26]. (a)  $dI/dV$  spectrum with increasing magnetic field. The Kondo peak splits linearly with the magnetic field. (b)  $dI/dV$  plot as a function of bias  $V$  and gate bias  $V_g$  at  $B = 6$  T. (c) The peak splitting as a function of magnetic field.

### 1.3.2 The proximity of ferromagnetic leads

As outlined in the previous sections, the Kondo effect is a model system for understanding correlated-electron physics. Another well-known correlated system is itinerant electron ferromagnetism. These two in principle compete each other. In the Kondo ground state, the localized spin is screened by the conduction electrons, which then tend to suppress any magnetic interaction of the impurity with its environment. In a ferromagnetic ground state instead, spin degeneracy is broken and, accordingly, the Kondo ground state is no longer degenerate and may even be suppressed [36]. In a pioneering work, Pasupathy *et al.* studied how the Kondo effect evolves in the presence of ferromagnetic electrodes [9]. They used a  $C_{60}$  molecule to mimic a Kondo impurity and placed it between two ferromagnetic Ni electrodes by electromigration [Fig. 1.9(a)]. The two electrodes were given different geometrical shapes in order to ensure that they undergo magnetic reversal at different values of the external magnetic field. This then allows controlling the relative direction of the lead magnetizations. Figure 1.9(b) shows the schematics of the junction for parallel alignment of the lead magnetizations ( $\uparrow\uparrow$ ) and antiparallel alignment ( $\uparrow\downarrow$ ). The splitting of the Kondo resonance was observed in some of these devices [Fig. 1.9(c)]. The peak splitting amounts to 18 mV for the  $\uparrow\uparrow$  configuration, but for the  $\uparrow\downarrow$  case, only one peak was observed. A Zeeman splitting is not sufficient to explain the splitting at zero bias for the  $\uparrow\uparrow$  configuration because the width of the peak splitting corresponds to

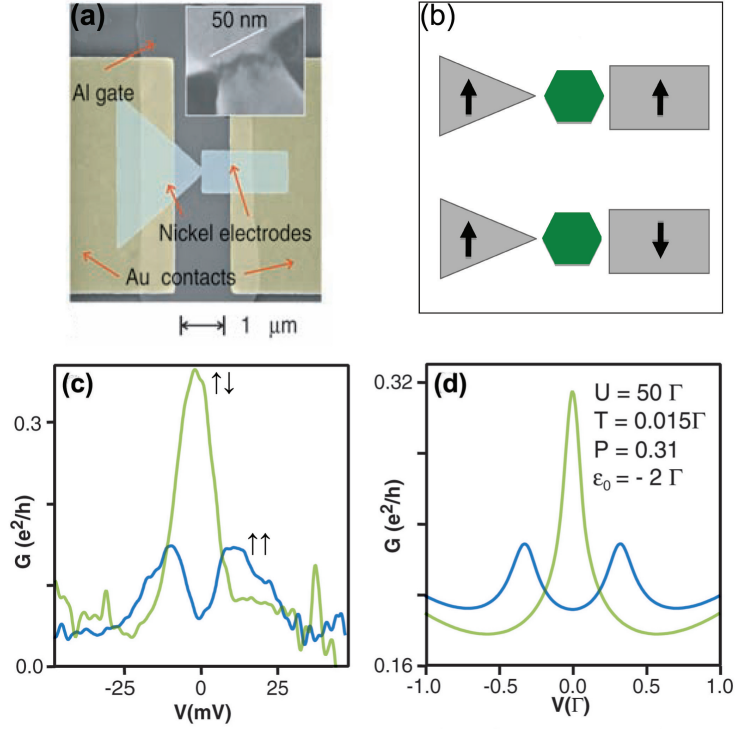


Figure 1.9: Schematics and conductance curves of a Ni-C<sub>60</sub>-Ni break junction at  $T = 1.5$  K from Ref. [9]. (a) Scanning electron microscope image of a Ni break junction. The inset shows a close-up view of the break-junction region after electromigration. (b) Schematics of  $\uparrow\uparrow$  and  $\uparrow\downarrow$  configuration of the junction. (c) Bias-dependence of the differential conductance for the  $\uparrow\uparrow$  configuration (blue line) at  $B = -250$  mT and the  $\uparrow\downarrow$  configuration (green) magnetizations at  $B = 15$  mT. (d) Theoretical simulation using the numerical renormalization group technique.

an effective magnetic field of 70 T. The peak splitting  $\Delta$  can be rationalized by the following model [37]

$$\Delta = 2a \sum_{r=L,R} P_r \Gamma_r, \quad (1.10)$$

where  $a$  is a constant of order unity depending on the charging energy  $U$ , the position of the Anderson energy level  $\epsilon$ , and the band structure.  $P$  is the polarization of the electrodes and defined as  $P = (\Gamma_{\uparrow} - \Gamma_{\downarrow})/(\Gamma_{\uparrow} + \Gamma_{\downarrow})$ , which is equivalent to  $P = (\rho_{\uparrow} - \rho_{\downarrow})/(\rho_{\uparrow} + \rho_{\downarrow})$ .  $\Gamma_{\uparrow(\downarrow)}$  is  $\pi \rho_{\uparrow(\downarrow)} |V_{kd}|_{av}^2$  [see Eq. (1.2)], and  $\rho_{\uparrow(\downarrow)}$  is the spin dependent DOS for spin-up (down) at  $E_F$ , respectively. The resonance splitting for the two configurations is then

$$\Delta_{\uparrow\uparrow} = 2aP (\Gamma_L + \Gamma_R), \quad (1.11)$$



$$\Delta_{\uparrow\downarrow} = 2aP(\Gamma_L - \Gamma_R),$$

where it is assumed that the polarization of a Ni electrode is  $P = P_L = P_R = 0.31$  for the  $\uparrow\uparrow$  configuration and  $P_L = -P_R = P$  for the  $\uparrow\downarrow$  configuration. If the coupling is same for both left and right electrodes ( $\Gamma_L = \Gamma_R$ ), no resonance splitting can be expected in the  $\uparrow\downarrow$  configuration, while a resonance splitting is observed in the  $\uparrow\uparrow$  configuration as shown in Fig. 1.9(c). We note that a similar result was also obtained with a carbon nanotube bridging two Ni electrodes [38].

To understand the origin of the resonance splitting, it is essential to focus on the electronic and magnetic coupling of the Kondo impurity with the ferromagnetic leads. The electronic coupling is assumed to be sufficiently weak so that electrons tunnel from the leads into the Kondo impurity. Due to the strong spatial confinement of  $d$  electron orbitals, the contribution of electrons from  $d$  subbands to transport across the tunnel barrier can be neglected. The role of  $s$  electrons is then dual. On the one hand, the interaction of the impurity spin with the tunneling  $s$  electrons produces the Kondo effect. On the other hand,  $s$  electrons establish an indirect ferromagnetic interaction between the leads and the impurity. The  $s$  electrons are in fact spin polarized due to the ferromagnetic leads and produce at the impurity site an effective molecular field which correlate the impurity spin with the magnetization of the leads. When the molecular field produced by the two leads is the same ( $\uparrow\uparrow$  configuration), the twofold degeneracy of the Kondo ground state is lifted. When the fields compensate ( $\uparrow\downarrow$  configuration), the Kondo ground state is preserved. A strict treatment of the problem was carried out by Martinek *et al.* using the numerical renormalization group (NRG) technique [37, 39, 40]. Figure 1.9(d) presents a numerical equation of motion (EOM) simulation using the parameters:  $\Gamma = 30$  meV,  $\epsilon = -2\Gamma$ , and  $U = 50\Gamma$ , which correctly reproduces the experimental observations.

For transport across the Kondo resonance, the conductance  $G$  can be amplified by turning the electrode magnetization from parallel to antiparallel. In fact the Kondo resonance occurs closer to the Fermi energy when the magnetization of the leads is antiparallel ( $G_{\uparrow\uparrow} < G_{\uparrow\downarrow}$  at zero bias). In this respect, the Kondo resonance serves as an indicator of the relative orientation of the two lead magnetizations.

### 1.3.3 Two-Kondo impurity problem

A Kondo impurity can also exchange and interact with neighboring magnetic impurities, which may possess same or different Kondo temperature. The interaction can occur in several ways. The interaction is direct when it is carried by the Coulomb interaction among  $d$  or  $f$  shell

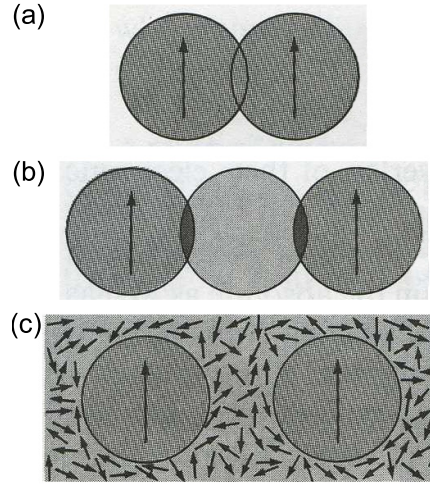


Figure 1.10: Schematics of magnetic interactions. (a) Direct exchange through the overlapping of  $d$  or  $f$  shells. (b) Superexchange is mediated by overlapping of the charge distribution with a non-magnetic atoms. (c) Indirect exchange interaction is carried by the conduction electrons [44].

electrons [Fig. 1.10(a)]. If two magnetic moments are separated by a nonmagnetic atom and interact through the  $s$  and  $p$  shell electrons of the nonmagnetic atom, then the spins are coupled by superexchange interaction [Fig. 1.10(b)]. Generally speaking, the interaction is instead indirect when  $d$  or  $f$  shells of the impurities interact via the  $s$  and  $p$  conduction electrons [Fig. 1.10(c)]. An example was given in Section 1.3.2 where the Ni electrode and the  $C_{60}$  molecule magnetically interact via  $s$  electrons. Another important example is when the magnetic impurities are embedded in a non-magnetic host metal. The impurities can then interact with each other through the conduction electrons of the host metal. This is the so-called Ruderman-Kittel-Kasuya-Yosida (RKKY) interaction [41–43]. The RKKY interaction is a long range interaction and the coupling  $I_{RKKY}$  is

$$I_{RKKY}(r) \propto \frac{\cos(2k_F r)}{(2k_F r)^D} \quad (1.12)$$

where  $r$  is the propagating distance in space,  $k_F$  is the Fermi wave vector and  $D$  is the dimensionality of the system. The oscillatory dependence of the distance with the wave length  $\pi/k_F$  changes the interaction from ferromagnetic (FM) to antiferromagnetic (AFM) or vice versa.

There have been open questions on the competition between the Kondo effect and magnetic

interactions. In a bulk system, this competition can lead to complex magnetic states such as spin glasses [45]. Exchange interactions (direct or indirect) between magnetic impurities can also suppress and split the Kondo resonance. Theorists worked actively on the simplified case of two interacting Kondo impurities, also called the two-Kondo impurity problem [46–51]. Several experimental observations of the two-Kondo problem have been reported for QDs and, as we show in the next Chapter, also for impurities adsorbed on metal surfaces. These studies include the direct interaction between spins on two QDs [52, 53] and the indirect RKKY interaction of two QDs separated by a larger dot [54]. The Hamiltonian describing the two-Kondo problem can be written as [55]

$$H = H_0 + J_1 \mathbf{S}_1 \cdot \mathbf{s}_1 + J_2 \mathbf{S}_2 \cdot \mathbf{s}_2 + I \mathbf{S}_1 \cdot \mathbf{S}_2, \quad (1.13)$$

where  $H_0 = H_{cond} + H_{imp1} + H_{imp2}$  accounts for the unperturbed conduction electrons and for the unperturbed  $d$  states of the two impurities [see Eq. (1.1)]. The following two terms describe the interaction between the spin of the conduction electrons and the spin  $\mathbf{s}_{1(2)}$  carried by each impurity. The last term accounts for the magnetic interaction among the two impurities, where  $I$  can be any kind of exchange interaction, either direct or indirect.

One relevant aspect for the Kondo effect described by this Hamiltonian is the sign of the interaction  $I$ . We consider first a ferromagnetic interaction (FM,  $I > 0$ ). The strength between the FM interaction and the two Kondo scales — $T_K^1$  for the first impurity,  $T_K^2$  for the second impurity —leads to various scenario. For small  $I$ , *i.e.*  $I \ll T_K^1, T_K^2$  or  $T_K^2 < I < T_K^1$ , two spin-1/2 impurities independently have their own Kondo cloud and therefore their own Kondo resonance. In the case of  $I \gg T_K^1, T_K^2$ , the spins of two impurities sum up to form a triplet state ( $S = 1$ ). At very low temperature ( $T \rightarrow 0$ ), the  $S = 1$  state is totally screened and a Kondo resonance emerges. A new Kondo ground state with temperature  $T_K^* \approx \max(T_K^1, T_K^2)^2/I$  is then defined [47].

The other case is for  $I < 0$ , which describes the antiferromagnetic coupling (AFM). Here, the competition between the exchange interaction and the Kondo effect can define a quantum critical point at  $(|I|/T_K)_c = \frac{4}{\pi}(1 + \frac{T_K^2}{T_K^1})$  [56–58]. As shown in Eq. (1.6),  $T_K$  depends exponentially on the coupling  $\Gamma$  of the impurity to the metal. A crude approximation consists in assuming  $T_K \sim e^{-\epsilon/\Gamma}$  and supposing that  $\epsilon_1 = \epsilon_2$ . Differences between  $T_K^1$  and  $T_K^2$  are then governed by even small differences in the coupling  $\Gamma_1$  and  $\Gamma_2$ . The critical value (Inset of Fig. 1.11) can vary from 2.54 ( $\Gamma_1 = \Gamma_2$ ), to 1.27 ( $\Gamma_1 = 0$ ) where only an impurity has a Kondo ground

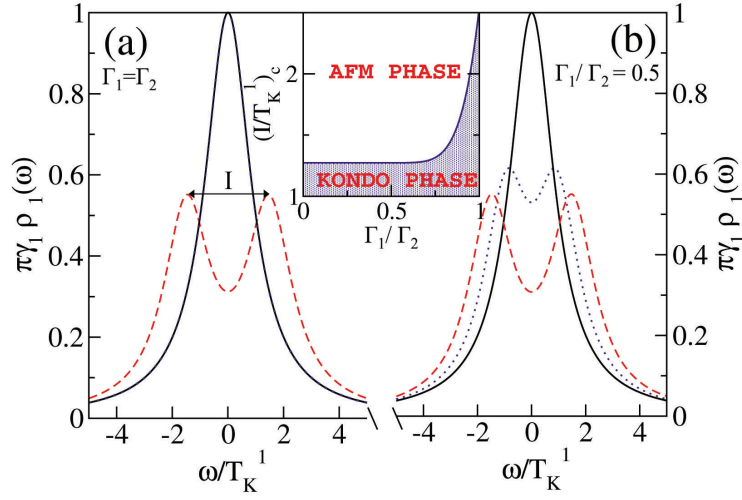


Figure 1.11: The DOS in the case of an AFM interaction among two Kondo impurities. (a) DOS of the symmetric case for  $|I|/T_K^1 = 1$  (solid line), 2 (dotted line) and 3 (dashed line). The resonance splitting by the AFM interaction arises when  $|I|/T_K^1 > 2.54$ . (b) DOS for the asymmetric case ( $\Gamma_2 = \Gamma_1/2$ ,  $T_K^2 \ll T_K^1$ ) for  $|I|/T_K^1 = 1$  (solid line), 2 (dotted line) and 3 (dashed line). The inset shows the critical boundary between the Kondo phase and the AFM phase as a function of the relative hybridizations of the two impurities with the host metal.

state. When the Kondo temperature overcomes the interaction i.e.  $|I|/T_K < (|I|/T_K)_c$ , each impurity forms its own Kondo ground state. For  $|I|/T_K > (|I|/T_K)_c$ , the two impurities are instead combined into a singlet state ( $S = 0$ ). The Kondo resonance is then split into two peaks located at  $\pm I/2$  as shown in Fig. 1.11(a). If the magnetic impurities have different  $T_K^1 \neq T_K^2$ , the critical point changes. Figure 1.11(b) presents the DOS for the  $T_K^1 \neq T_K^2$  case where the resonance splitting is in principle detectable at even lower values of  $|I|/T_K^1$  compared to the symmetric  $T_K^1 = T_K^2$  ( $\Gamma_1 = \Gamma_2$ ) case.

An instructive example of how magnetic interactions affect the Kondo physics was given by Heersche *et al.* [10], who studied the Kondo effect in the presence of an RKKY interaction. In their experiment, a gold grain acts as a QD with a Kondo ground state, while magnetic impurities in the leads produce the RKKY interaction [Fig. 1.12(a)]. The sign of the RKKY interaction can clearly be determined from their measurements. When  $|I| > k_B T_K$  and  $|eV| < |I|$ , the AFM or FM interactions suppress the each of Kondo ground state. When the coupling is AFM, a singlet state ( $S = 0$ ) is energetically favored with respect to a triplet state ( $S = 1$ ) as sketched in Fig. 1.12(b). The Kondo resonance is then split into two peaks apart by  $I \approx 2$  mV

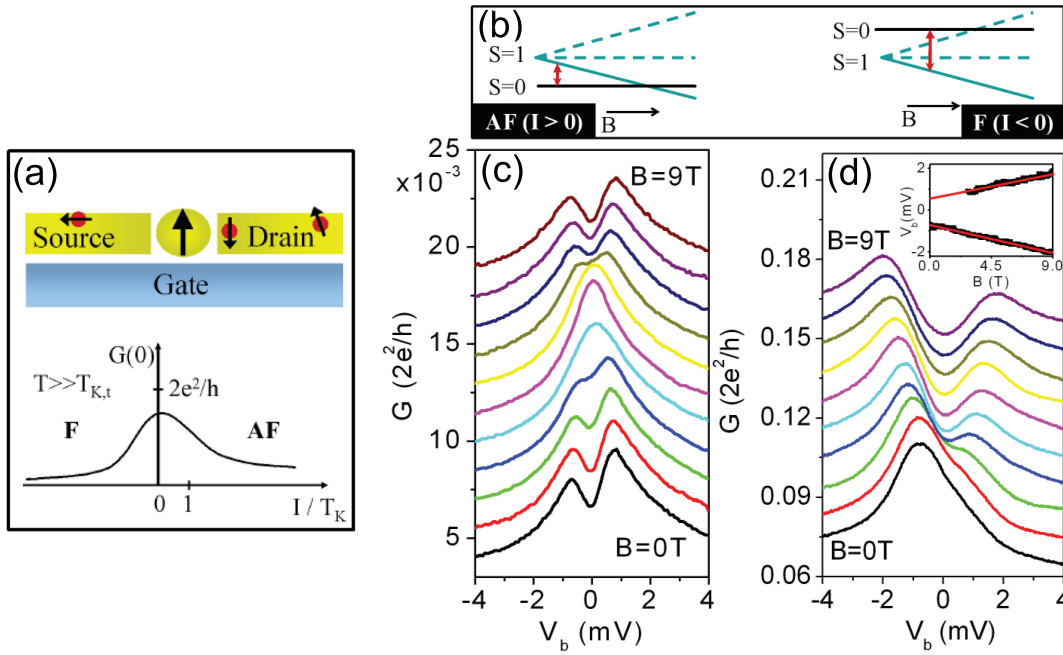


Figure 1.12: Resonance splitting and restoring in a magnetic field. (a) Schematic of the device where the magnetic QD interacts with other magnetic impurities embedded in the leads. (b) The singlet-triplet transition energy for the AFM and FM interactions. (c)-(d)  $dI/dV$  versus bias  $V$  with a magnetic field of 0 T to 9 T by steps of 0.9 T ( $T = 250\text{mK}$ ): (c) AFM interaction, (d) FM interaction [10].

[Fig. 1.12(c)], but can be restored to a single peak by applying an external magnetic field  $H$ . Formally, this corresponds to adding a Zeeman term in Eq. (1.13). As  $H$  increases, the triplet state is lowered until the Kondo resonance is fully restored at  $H = I/(2g\mu_B)$  where the Kondo ground state switches from a singlet to a triplet state. As  $H$  is further increased, the resonance undergoes a Zeeman splitting as mentioned in Section 1.3.1 [55]. The simpler FM case is presented in Fig. 1.12(d). The triplet ground state produces a new Kondo resonance, which is then split apart by a Zeeman effect as  $H$  is increased. This textbook experiment clearly shows that by adjusting the sign and strength of the exchange interaction, the Kondo effect can be controlled with a high tunability. Conversely, the Kondo effect may be employed to learn something about the magnetic interactions between impurities. For example, it can be used to determine the sign and strength of the magnetic interaction.

## Summary and conclusions

In this Chapter, we briefly introduced the Kondo effect by recalling the Anderson and Kondo models describing a magnetic impurity in a host metal. The Kondo effect occurs when a localized magnetic moment is antiferromagnetically screened by the electronic spins of the host metal. Below  $T_K$ , this many-body interaction results in the emergence of a resonance in the DOS near  $E_F$ , the so-called ASK resonance. We have given some examples of how the Kondo effect can be detected in the conductance of single objects such as an artificial QD or a single molecule coupled to metallic leads.

We have also shown how the Kondo effect can be used to probe the magnetic surroundings of an impurity. First of all, we showed that a magnetic field produces a Zeeman splitting of the resonance. The observation of a Zeeman splitting is one of the ways to prove that a zero-bias anomaly in the conductance is indeed a Kondo resonance. Next, we presented pioneering results for a Kondo impurity coupled to ferromagnetic leads. We showed that the ferromagnetic leads act as an effective magnetic field that can split the Kondo resonance apart. The resonance splitting may be tuned by changing the magnetization of one of the ferromagnetic leads. Conversely, the presence or not of a resonance splitting is an indication of the magnetic status of the leads. As a last topic, we discussed how the Kondo effect changes when two impurities are magnetically coupled. Depending on the sign and strength of the interaction, the Kondo resonance can split apart (AFM) or not (FM). The Kondo effect is therefore a powerful probe for detecting the nature and strength of magnetic interactions at the atomic scale.



## CHAPTER 2

# Scanning tunneling microscopy and spectroscopy

It has become possible to explore the world at the molecular and even at the atomic scale thanks to recent advances in nanoscience and nanotechnology. Among these advances is the scanning tunneling microscope (STM). Atomic-scale information can be gathered with such a microscope through topographical images and through the differential conductance acquired at precise locations above the surface. The first part of the Chapter is devoted to introducing the ultra-high vacuum (UHV) setup and the low-temperature STM used in this Thesis, followed by a description of the tip and sample preparation (Section 2.1). The operating principle of STM (Section 2.2) and spectroscopy (STS) (Section 2.3) are then introduced. The second part of this Chapter is focused on the detection of the Kondo resonance through STS (Section 2.4) where in particular it is shown that the Kondo resonance in STM experiments is observed as a Fano interference. This Section ends by showing how STM allows exploring the magnetic interactions among atoms possessing a Kondo ground state.

### 2.1 Experimental setup

The studies presented in this Thesis focus on the investigation of single objects such as atoms and molecules. Clean atomically well-defined samples are required to minimize the contamination and obtain reliable results. A ultra-high vacuum (UHV) system is therefore necessary for carrying out the experiments, including a careful *in situ* preparation of tip and sample. Since



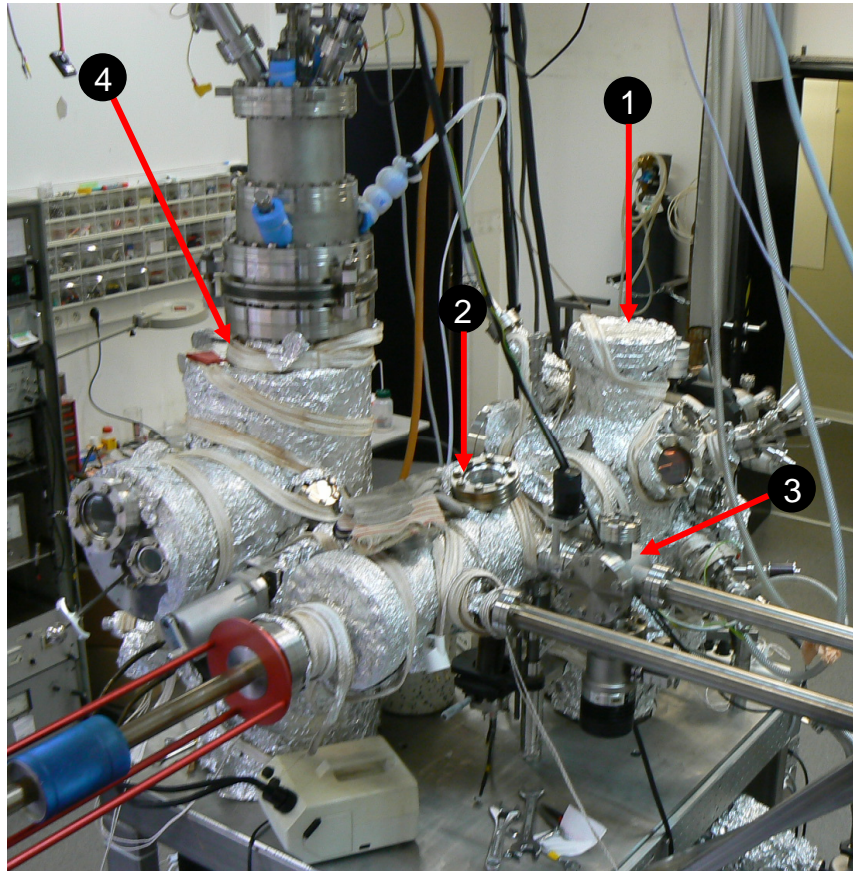


Figure 2.1: UHV system and facility. (1) Preparation chamber, (2) intermediary chamber, (3) load-lock chamber, and (4) STM chamber.

the energy scale of the Kondo effect is mostly in the meV range, a low enough temperature is needed to access this bias resolution in the experiments. Low temperature is also needed to stabilize atoms on the surface.

### 2.1.1 STM in UHV

Our facility consists of three chambers: a load-lock chamber, a preparation chamber and an STM chamber with a base pressure of  $P \leq 10^{-10}$  mbar (Fig. 2.1). The load-lock chamber is used for the transfer of samples and tips from ambient pressure to UHV and vice-versa. The preparation chamber is for sample and tip cleaning and preparation. The chamber is equipped with a sputtering ion gun to clean the sample (tip) and a heating filament to anneal

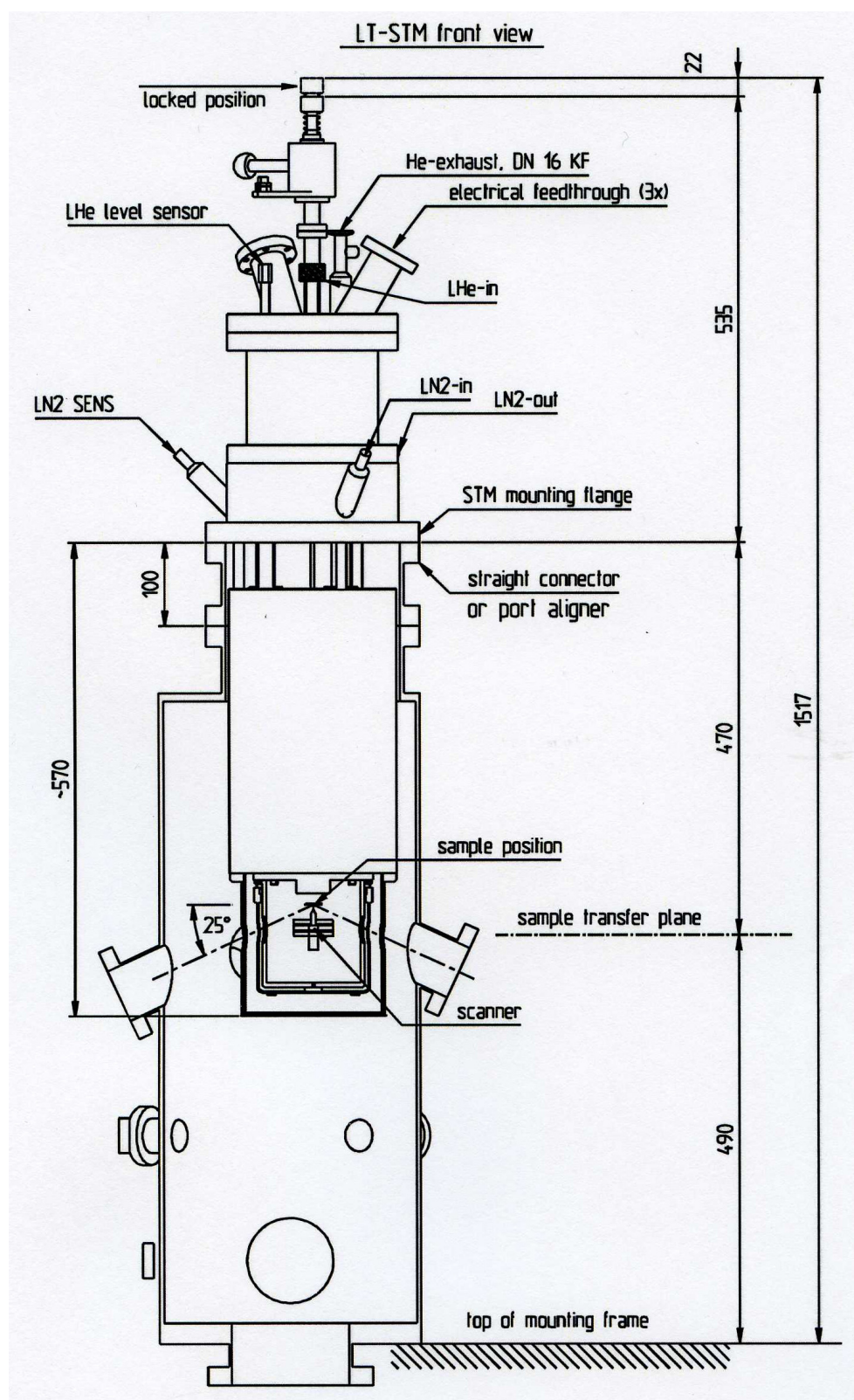


Figure 2.2: LT-STM schematic diagram.

the crystal. Another filament is used to flash the tip. There are two e-beam evaporators to deposit metallic materials such as Co, Cr, Fe, *etc.* and a homemade molecular evaporator to deposit the molecules on the surface. The STM chamber holds the STM and is separated from the preparation chamber by a gate valve in order to minimize contamination during the preparation of the sample (tip). The measurements were carried out with a commercial Omicron low temperature (LT)-STM operating in UHV conditions at 4.6 K. Figure 2.2 presents our LT-STM schematic diagram. The STM head is mounted on a liquid helium inner cryostat. A liquid nitrogen outer cryostat is necessary to shield the inner cryostat from infrared radiations and ensure a He standing time of 26 hours.

Once the chamber is exposed to air, the chamber should be baked to  $\geq 100^{\circ}\text{C}$  for at least 24 hours to get rid of water, vapor and residual gases on the wall. Each chamber is equipped with a scroll pump ( $P \geq 10^{-3}$  mbar), a turbo pump ( $P \geq 10^{-9}$  mbar), a Ti sublimation pump (TSP) and an ion pump ( $P \geq 10^{-11}$  mbar), which ensure a base pressure below than  $10^{-10}$  mbar. The scroll pump is used to pump the system from atmosphere to  $10^{-3}$  mbar, while the turbo pump covers the pressure range between  $10^{-3}$  and  $10^{-9}$  mbar. TSP is used typically to pump the reactive components such as CO, O<sub>2</sub>. The ion pump ionizes the gases by applying the electrical field between two electrodes and traps them in a strong magnetic field, and the ionized gases are then chemisorbed on the plate wall. The ion pump ensures the base pressure below  $10^{-10}$  mbar and is the only pump running during the measurements to favor a low-noise environment. Additionally cryo-pumping from the walls of the LT-STM allows attaining pressures below  $10^{-11}$  mbar, and no contamination is detectable on the sample surface for weeks.

## 2.1.2 Tip and sample preparation

### Tip preparation

All non-magnetic tips employed in this Thesis were made with a tungsten (W) wire, while magnetic tips were made with Ni and Fe wires. The wires were etched *ex situ* electrochemically using NaOH or H<sub>2</sub>SO<sub>4</sub> solutions in order to produce very small curvature radius of the tip apex ( $< 1\ \mu\text{m}$ ) [59]. The tip is then fixed in a tip holder and transferred into the UHV chamber. The transferred tip is cleaned *in vacuo* by argon-ion bombardment and flashed to  $800^{\circ}\text{C}$  to remove oxidized impurities in the tip. Once in the STM, the tip apex can be further treated by soft indentations into the surface to yield a tip with a monoatomic apex. As the tunneling

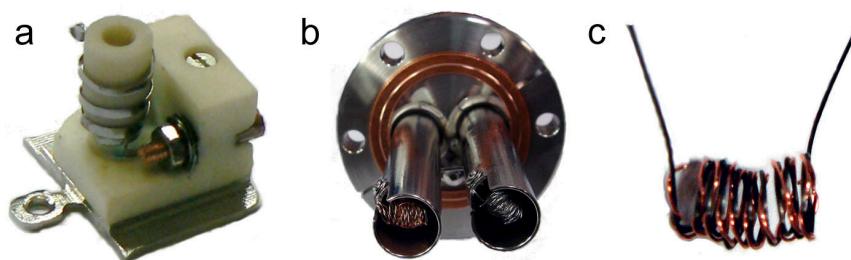


Figure 2.3: Homebuilt molecular and metal evaporators. (a) Molecular evaporator, (b) multiple-metal evaporator. (c) Zoom-in view of the wire used in (b).

current depends exponentially on tip-sample distance, STM images are extremely sensitive to the geometry of the tip apex. The usual and most convenient way to test for multiple tip apices is to image atomically sharp features on the surface. For example, a step edge or a single atom is imaged a multiple number of times when the tip has multiple apices. When a single adsorbed atom is imaged as a round protrusion and the step edges are sharp in the images, we may consider instead that a single atom terminates the tip apex. A controlled contact between such a tip and a pristine metal surface yields a conductance close to the quantum of conductance as predicted for a single-atom point contact [60]. The apex structure is then presumably a pyramid or a tetragon (this is the apex geometry used for DFT simulations). This tip treatment is also needed for scanning tunneling spectroscopy (STS) (Section 2.3) in order to minimize the tip electronic structure in the bias range of interest.

### Crystal preparation

Crystals such as Cu(100), Cu(111) and Ag(111) were cleaned *in vacuo* by repeated cycles of argon ion bombardment and annealing up to 400°C depending on crystal materials. After flowing given amounts of Ar gas ( $P \leq 10^{-6}$  mbar) in the preparation chamber, electrons are emitted from the filament of the ion gun and collide with the Ar gas producing  $\text{Ar}^+$  ions. An  $\text{Ar}^+$  ion beam is then focused onto the sample to bombard the crystal. Several layers of the crystal can be removed in this way. Once the sputtering is done on the crystal, annealing is necessary to heal the rough surface caused by the bombardment; a proper annealing procedure produces large ( $> 50 \text{ nm}^2$ ) terraces. Several repeated cycles of sputtering and annealing are necessary.



### Molecule deposition

A homebuilt evaporator shown in Fig. 2.3(a) is utilized for the deposition of  $C_{60}$  molecules. The substance powder is mounted in a ceramic crucible, which is heated by a current through a tantalum filament wound around the crucible. Temperatures up to  $600^{\circ}\text{C}$  can be reached in this way. Before deposition, the powder is degassed for 48 hours. Vacuum sublimated  $C_{60}$  99.9% pure powder was provided by MER CORPORATION;  $C_{60}$  was deposited at  $400^{\circ}\text{C}$ . A calibration of the deposition rate was done by a quartz-balance in order to have a well defined and reproducible coverage of molecules on the sample.

### Atom deposition

When atoms have a kinetic energy, they migrate to step edges or defect sites which are energetically more favorable. Therefore, atom deposition should be done at low temperature to eliminate diffusion on the surface ( $< 20\text{ K}$  : depending on crystal plane axis). A homebuilt metal evaporator was used to deposit the atoms as shown in Fig.2.3(b). A wire of Cu, Au, Co ( $> 99.99\%$  purity) *etc.* is wound around a tungsten filament (wire diameter:  $0.25\text{ mm}$ ; spiral diameter:  $\approx 5\text{ mm}$ ) as presented in Fig. 2.3(c). As a current passes through the tungsten wire and the points of contact between the wire and the tungsten spiral are heated, small amounts of the wire material are evaporated resulting in sub-monolayer coverage of atoms on the surface. The deposition was done to the pre-cooled sample by opening the liquid helium shield of the inner cryostat in STM chamber. The temperature of the sample varies from  $4.6\text{ K}$  to  $8\text{ K}$  due to the opening of the shield during the metal atoms evaporation and goes back to  $4.6\text{ K}$  after the deposition. After this procedure, no contamination was observed.

## 2.2 Principle

In 1986, the Nobel prize in physics was awarded to Gerd Binnig and Heinrich Rohrer who designed and invented the STM with Ch. Gerber and E. Weibel [61–63]. Thanks to their contributions, studies of nanostructures on surfaces have been carried fruitfully up to now. STM exploits the tunneling effect between a tip and a sample in vacuum. In particular, information about objects on surfaces is gathered through the tunneling current  $I$  and the differential conductance,  $dI/dV$ . Tersoff and Hamann suggested a simple theory of STM to bridge the  $I$ ,  $dI/dV$  measurements to fundamental properties of the system, which is based on the Bardeen's

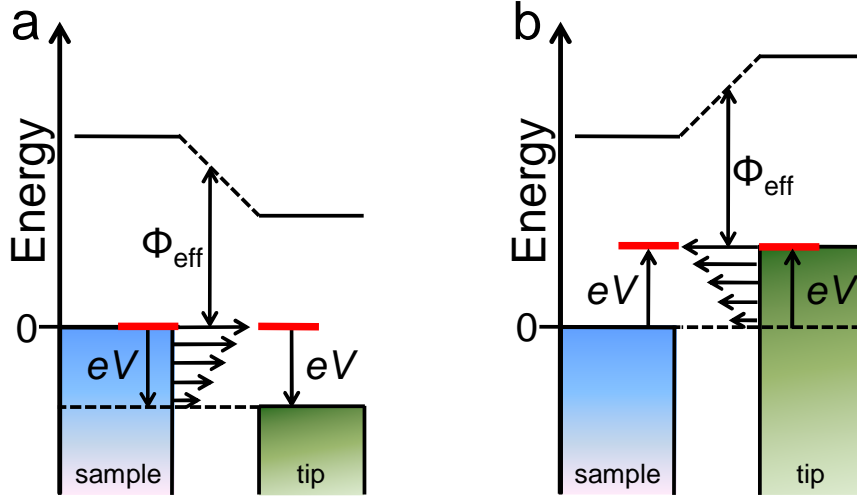


Figure 2.4: Energy diagram for positive and negative bias respect to the sample. (a) At negative bias, electrons are tunneling from occupied sample states to unoccupied tip states. (b) At positive bias, electrons are tunneling from occupied tip states to unoccupied sample states [70].

formalism [64]. Within the Tersoff-Hamann model, the tunneling current  $I$  can be derived as [65–67]

$$I(V, z) \propto \int_0^{eV} \rho_t(E - eV) \rho_s(E) [f_t(E - eV) - f_s(E)] T(E, eV, z) dE, \quad (2.1)$$

where  $\rho_{t,s}$  are the local density of state (LDOS) of tip and sample, respectively.  $V$  is the applied bias,  $E$  is the total energy,  $f_{t,s}$  are the Fermi-Dirac distributions of tip and sample, and  $z$  is the tip-sample distance. The transmission probability,  $T$ , is expressed as

$$T(E, eV, z) \equiv \frac{I(z)}{I(0)} = \exp \left( -2 \int_0^z \kappa(z) dz \right). \quad (2.2)$$

When the tunneling barrier is trapezoidal,  $T$  is given by a semiclassical Wentzel-Kramer-Brillouin (WKB) approximation,

$$T(E, eV, z) \propto \exp \left( -2z \sqrt{\frac{m}{\hbar^2} (2\Phi_{\text{eff}} + eV - 2E)} \right), \quad (2.3)$$

where  $\Phi_{\text{eff}} = (\Phi_t + \Phi_s)/2$ , and  $\Phi_{t,s}$  are the work functions of tip and sample, respectively [68,69]. Figure 2.4 shows the tunneling configuration when a negative and positive bias are applied to

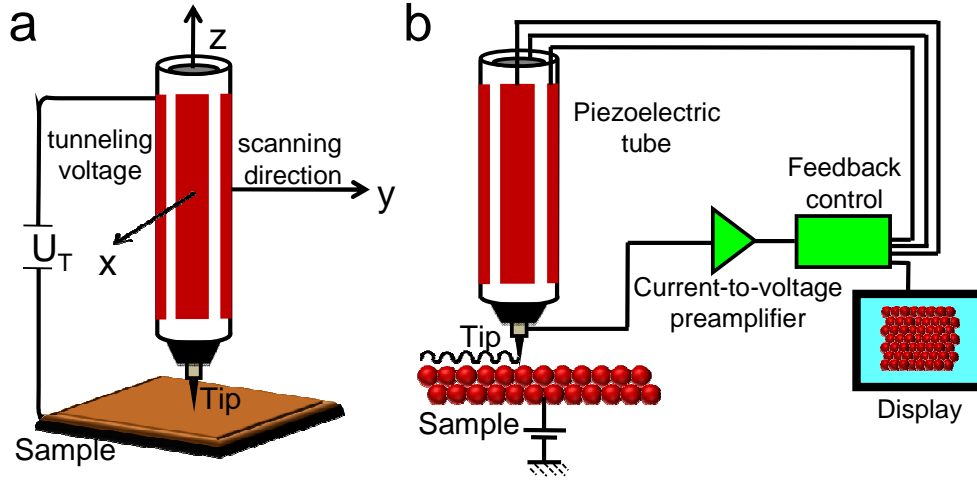


Figure 2.5: Schematics of the experiment setup. (a) Piezoelectric tube with four external electrodes (x, -x, y, -y) and one internal electrode (z). (b) Piezoelectric tube and feedback control for acquiring images.

the sample. When the negative bias is applied with respect to the sample [Fig.e 2.4(a)], the electrons of the sample in an occupied level between  $E_F - eV$  and  $E_F$  tunnel to the unoccupied tip states. On the other hand, at positive bias [Fig.e 2.4(b)], electrons of the tip occupied states from  $E_F$  up to  $E_F + eV$  tunnel to the empty sample states. Therefore, the occupied ( $eV < 0$  respect to the sample) or unoccupied ( $eV > 0$ ) integral LDOS of the sample are measured by sweeping the bias, assuming  $\rho_t$  is constant.

When  $k_B T \ll eV$ , the temperature dependence of the Fermi-Dirac distribution can be neglected and  $f_t - f_s \simeq 1$ . The current can then be written as,

$$I(V, z) \propto \int_0^{eV} \rho_t(E - eV) \rho_s(E) T(E, eV, z) dE. \quad (2.4)$$

With Eq. (2.3), the dependence of  $I$  on  $z$  can be deduced as

$$I(z) \propto \exp \left( -A \sqrt{\Phi_{\text{eff}}} z \right), \quad (2.5)$$

where  $A$  is  $2\sqrt{2m/\hbar^2} = 1.025 (eV)^{-1/2} \text{\AA}^{-1}$ . For a metallic surface,  $\Phi_{\text{eff}} \simeq 5 eV$ , therefore every  $1 \text{\AA}$ , the current decreases by one order of magnitude. At a distance of  $5 \text{\AA}$  from the surface, the current is of order  $1 \text{ nA}$  at  $1 \text{ V}$ .

Figure 2.5(a) shows the schematic of the STM junction. When data acquisition is per-

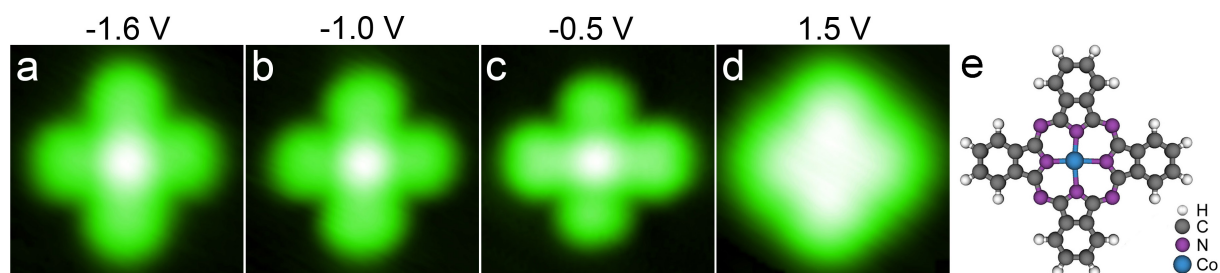


Figure 2.6: (a)-(d) Constant-current topographic images of a single CoPc molecule on Cu(111) at various biases ( $23 \times 23 \text{ \AA}^2$ , 0.5 nA). (e) Chemical structure of CoPc.

formed, the lateral as well as the vertical positions are controlled by a piezoelectric tube [71]. A feed-back loop allows adjusting the distance between tip and sample to maintain the current constant [see Fig. 2.5(b)]. These adjustments are recorded at every  $x$  and  $y$  coordinate of the surface in order to construct a topographic image. In other words, the current is held constant and the changes in  $z$  are recorded giving the direct electronic image of the objects on the surface. This so-called constant-current mode is commonly used for image acquisition without any limitations. The current-to-voltage preamplifier is consisted of a variable gain FEMTO DLPCA-200, while the STM controller is from Nanonis. When imaging a surface, there is also another mode available, known as constant-height mode. In this mode, the distance between the surface and the tip is kept constant and the current is measured during scanning. Since the feedback loop is open during these measurements, the signal-to-noise ratio is greatly improved. However, the constant-height mode is only applicable for the flat surfaces and small areas ( $5 \times 5 \text{ nm}^2$ ) because of the drift produced by the piezoelectric tube.

As an example, Figs. 2.6(a)–(d) show the constant-current topography of a single cobalt-phthalocyanine (CoPc) molecule at different biases. The images acquired reflect to some extent the spatial variation of the molecular orbitals, if the contribution of  $\rho_t$  in Eq. (2.4) is minimized. At negative bias, the topography is dominated by a  $d$ -like orbital centered on cobalt of CoPc. At positive bias, a clear contribution from the benzopyrrole rings is evidenced [72].



## 2.3 Spectroscopy

The differential conductance  $dI/dV$  can be derived from Eq. (2.4) as

$$\frac{dI}{dV}(V, z) \propto \rho_t(0)\rho_s(eV)T(eV, eV, z) + \int_0^{eV} \rho_t(E - eV)\rho_s(E) \frac{dT(E, eV, z)}{dV} dE, \quad (2.6)$$

when we assume that  $\rho_t$  is constant. The  $dI/dV$  is therefore proportional to the LDOS of the sample at a given height  $z$  if we assume that the second term in Eq. (2.6) is negligible:

$$\frac{dI}{dV}(V, z) \propto \rho_s(eV)T(eV, eV, z). \quad (2.7)$$

Spectral measurements are however prone to thermal and instrumental broadening. Formally, this may be expressed by the following convolution:

$$\left( \frac{dI}{dV} \right)_{\text{measured}} = \frac{dI}{dV} * \chi_T * \chi_M, \quad (2.8)$$

where  $\chi_T$  and  $\chi_M$  are the thermal and instrumental broadening functions (Fig. 2.7). The resolution of a spectrum ( $e\Delta V$ ) is then determined by the full width at half maximum of  $\chi_T$  and of  $\chi_M$  and amounts to [73]:

$$e\Delta V \approx \sqrt{(3.5k_B T)^2 + (1.7V_M)^2}. \quad (2.9)$$

The thermal broadening corresponding to  $0.3 \text{ meV K}^{-1}$  is caused by the smearing of the Fermi-Dirac distribution. As long as the width of spectral features is wider than  $3.5k_B T$ , we can neglect thermal broadening. In this Thesis, the working temperature is  $4.6 \text{ K}$ , yielding a thermal broadening of  $1.3 \text{ meV}$ .

The instrumental broadening is induced by the voltage modulation used for the lock-in detection. To probe the  $dI/dV$  signals, we use in fact a lock-in amplifier, which produces a much better signal-to noise ratio than the numerical differentiation of  $I(V)$ . For the lock-in detection, a bias modulation of amplitude  $V_M$  and frequency  $\omega$  is added to the bias  $V$ . The tunneling current  $I$  is then

$$I \equiv I(V + V_M \cos \omega t). \quad (2.10)$$

To obtain the  $dI/dV(V)$ , the first harmonic of  $I(V)$  should be recorded. However the bias

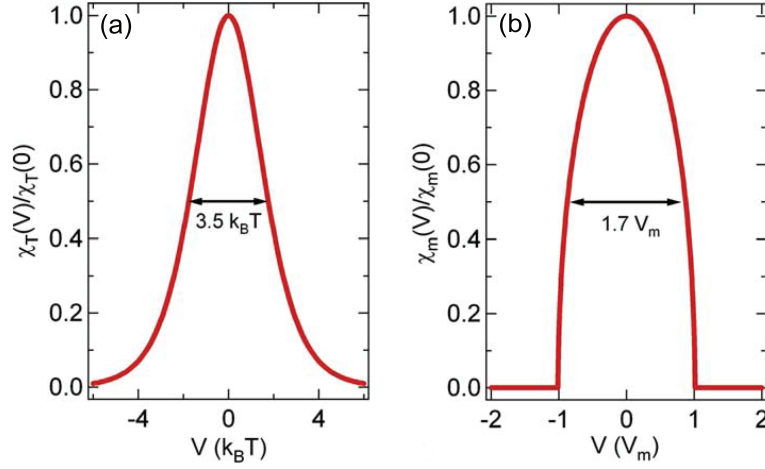


Figure 2.7: Broadening functions in STM. (a) Thermal broadening function caused by smearing of the Fermi-Dirac function. (b) Instrumental broadening induced by the lock-in amplifier [73].

resolution is limited by the modulation of the bias. The instrumental broadening varies linearly with the modulation amplitude resulting in a resolution of  $\sqrt{3}V_M = \sqrt{6}V_{rms}$ , where the  $V_{rms}$  is the root mean square (rms) of  $V_M$ . For the experiments presented in this thesis,  $V_{rms} = 1$  mV rms was used, which corresponds to a resolution of 2.4 mV. Since the width of the Kondo resonance of Co is  $\approx 20$  meV, we can neglect both the thermal broadening and the instrumental broadening in our studies.

STS measurements in this Thesis were always performed by fixing the lateral position of the tip. However, the  $dI/dV$  signal may also be recorded at every pixel of the image. The resulting image is called a  $dI/dV$  map, which visualizes the spatial distribution of the LDOS at a given bias. There are two ways to acquire a  $dI/dV$  map: in a constant-current mode and constant-height mode. In a constant-current mode, the  $dI/dV$  signal is measured at every single pixel and every time the tip is positioned on a pixel, the distance between a tip and a sample is re-adjusted to keep the current constant. With such a procedure, spectral and topographical informations are mixed as the tip-sample distance  $z$  changes from pixel to pixel [69, 74, 75]. On the other hand, the constant-height mode keeps a constant distance between the tip and the sample. In this case, the feed-back loop stays opened above every pixels of the area and only the  $dI/dV$  signals are detected. The signal-to-noise ratio and the intramolecular resolution are improved in this mode. As an example, we present in Fig. 2.8 images of a CoPc on Cu(111) acquired with the two modes. Figures 2.8(a)—(d) present the  $dI/dV$  maps acquired in constant-current

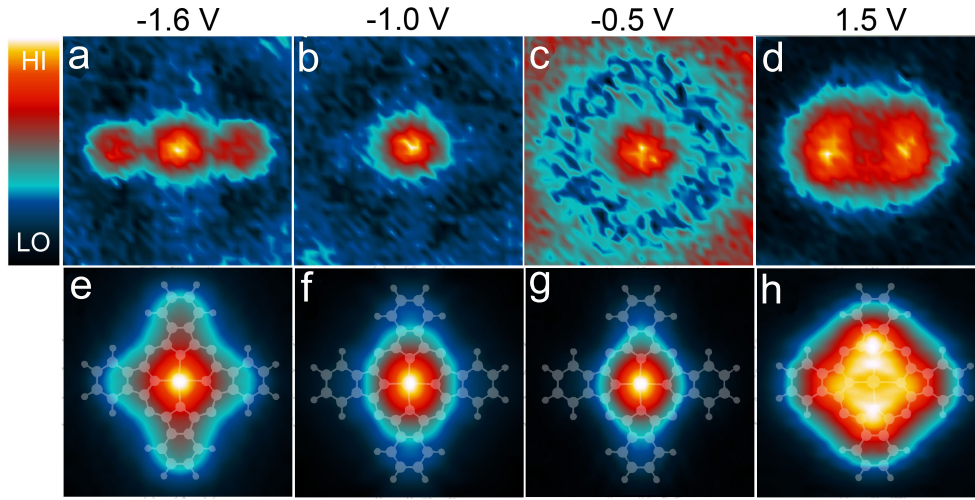


Figure 2.8: Constant-current mode and constant-height mode  $dI/dV$  maps of a single CoPc molecule on Cu(111) at various biases (image size:  $23 \times 23 \text{ \AA}^2$ ). (a)-(d) Constant-current  $dI/dV$  maps (feedback loop opened at 0.1 nA and 0.4 V). (e)-(h) Constant-height  $dI/dV$  maps (a scaled molecular scheme is superimposed to each map). The feedback was opened above the copper surface at 0.01 nA and at (e)  $-1.6 \text{ V}$ , (f)  $-1.0 \text{ V}$ , (g)  $-0.5 \text{ V}$ , and (h)  $1.5 \text{ V}$ , and was kept open during the image acquisition [72].

mode and Figs. 2.8(e)–(h) in constant-height mode. As shown, the constant-height mode yields an improved resolution of the spatial distribution of the LDOS [72].

## 2.4 Detection of the Kondo resonance with STM

The STM opened up an advanced avenue in Kondo physics. In 1998, the first observations with STM of the Kondo resonance above single-magnetic atoms on a metal surface were reported by two groups. Madhavan *et al.* showed that a narrow asymmetric feature near  $E_F$  appeared in the  $dI/dV$  of cobalt atoms on a Au(111) surface [7], while Li *et al.* observed a characteristic dip around  $E_F$  with Ce adatoms on Ag(111) [8]. When varying the lateral distance from the center of the atom, the ASK resonance was shown to decrease confirming that the effect is localized at the impurity site. It is well established today that the Kondo resonance can present an asymmetric lineshape in STM. The asymmetry varies depending on surface material and structure. Figure 2.9 shows for example the  $dI/dV$  spectra acquired above a Co atom on Cu(100), Cu(111) and Cu(110) [76, 77]. A step-like feature is found for Cu(100), while a dip is

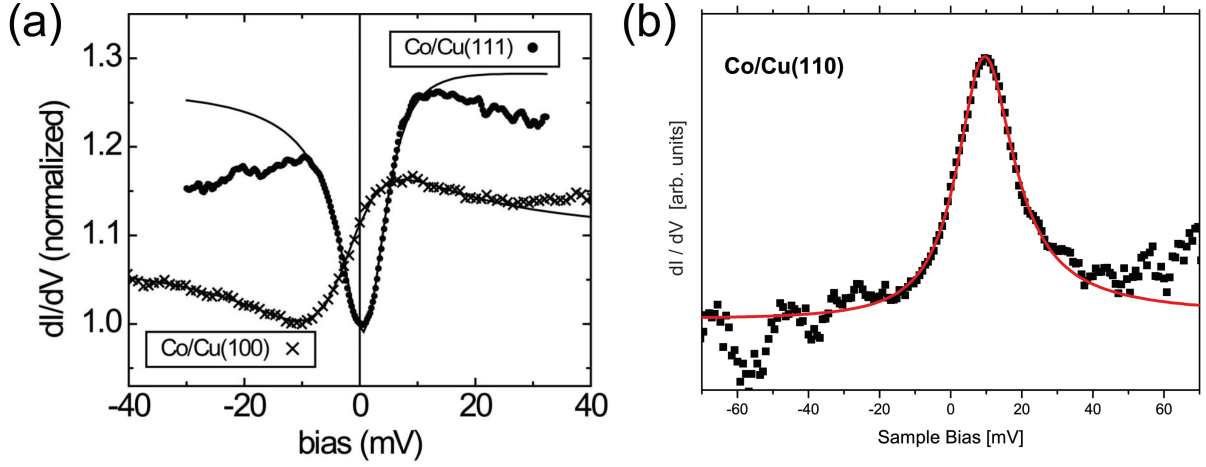


Figure 2.9:  $dI/dV$  spectra of a Co atom on various copper surfaces. (a)  $dI/dV$  spectra for Co/Cu(100) and Co/Cu(111) surfaces. The black lines are Fano fits [76]. (b)  $dI/dV$  spectrum above Co on Cu(110). The red line is a Fano fit [77].

observed on Cu(111) and a peak is detected on Cu(110). Another salient aspect is the value of the Kondo temperature which is lower compared to an impurity embedded in bulk. For example for cobalt,  $T_K$  is approximately 100 K on a copper surface while in bulk copper  $T_K$  is around 500 K. In the following, we give an explanation for these differences and then explain the peculiar lineshape of the ASK resonance in terms of a Fano interference (Section 2.4.1). Finally, we briefly show how the ability to manipulate atoms on a surface with STM can be exploited to investigate the two-impurity Kondo problem (Section 2.4.2).

### 2.4.1 Kondo effect of adsorbed magnetic atoms

The characteristics of the Kondo effect are influenced by the electronic structure of the substrate [79, 80], *i. e.* the interaction of the magnetic impurity with its nearest-neighbor atoms of the surface. The changes observed on noble metal surfaces were explained by Wahl *et al.* [78]. They showed that the Kondo temperature  $T_K$  can be expressed as

$$k_B T_K \simeq \sqrt{\frac{\Gamma U}{2}} e^{-(\pi U/2\Gamma)|-n+3/2||-n+1/2|} \quad (2.11)$$

using the relation  $n = -\frac{\epsilon}{U} + \frac{1}{2}$  in Eq. (1.6), where  $n$  is the occupation of the magnetic  $d$ -level. If one supposes that  $U$  and  $\Gamma$  change little for Co on the surfaces, we may then assign the

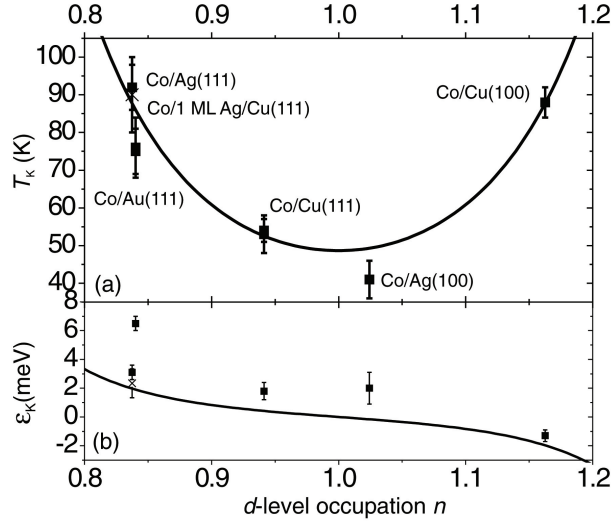


Figure 2.10: (a)  $T_K$  as a function of the occupation  $n$  of the  $d$ -level calculated from Eq. (2.12) and Eq. (2.11). (b)  $\epsilon_K$  as a function of  $n$  from Eq. (2.13). The dots are the experimental data [78].

changes in  $T_K$  to  $n$ —typically  $U = 2.5$  eV and  $\Gamma = 0.2$  eV [24]. The variation of the  $d$ -level occupation is increased by the  $sp$ - $d$  hybridization [81, 82] as shown by Anderson (Section 1.1), and changes of  $n$  with surface can then be expressed within a tight-binding model [83] as

$$n \propto n_{NN} e^{-a/\lambda} + \text{constant}, \quad (2.12)$$

where  $\lambda$  denotes the spatial extent of the  $d$  orbital (typically  $\lambda \approx 1$  Å). This relation establishes that changes in the occupation  $n$  and therefore  $T_K$  depend on surface structure through the number of neighboring substrate atoms ( $n_{NN}$ ) and the lattice parameter  $a$  of the surface. A similar conclusion may be deduced for the onset of the Kondo resonance  $\epsilon_K$  since

$$\epsilon_K = \Gamma \tan \left[ \frac{\pi}{2} (1 - n) \right]. \quad (2.13)$$

A nice agreement is found between the calculated and experimental estimates of  $T_K$  and  $\epsilon_K$  (Fig. 2.10). As shown,  $T_K$  varies between 40 K and 90 K, while  $\epsilon_K$  changes on the order of 1 meV. In quantum dots, the characteristics of the Kondo resonance can be tuned by gate voltages while in STM they can be pursued by using different surfaces.

In STM, the line shape of the Kondo resonance depends on the quantum interference,

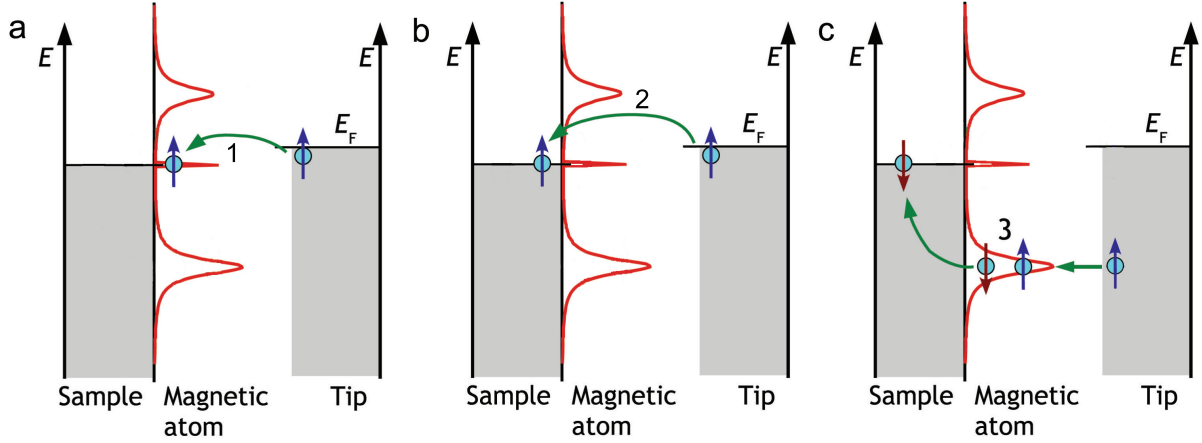


Figure 2.11: Schematic of the tunneling paths with a magnetic impurity on a non-magnetic surface. (a) Path 1 presents the tunneling through the Kondo resonance from the tip. (b) Path 2 describes the direct tunneling from the tip to the conduction band of the surface. For path 1 and 2, no spin flipping is expected. (c) A spin flipping process occurs in path 3. The electron from the tip, which has a lower transmission probability, first tunnels to the empty magnetic state of the impurity and then eventually tunnels in the conduction band of the surface at  $E_F$  through a spin-flip [33].

or Fano interference, of the tunneling channels [84, 85]. Figure 2.11 sketches the possible tunneling pathways between a metallic tip and a Kondo impurity. The first pathway is direct tunneling between the tip and the Kondo resonance [labeled 1 in Fig. 2.11(a)]. The second pathway is tunneling between the tip and the metal surface [non-Kondo processes, labeled 2 in Fig. 2.11(b)]. The third possibility is tunneling into the  $d$ -level of the impurity. In this case, the electron eventually has its spin flipped and is located at the Fermi energy in its final state. The occurrence of this “multi” tunneling process is however more rare than the previous two paths and we neglect it in the following. Paths 1 and 2 preserve the spin orientation and therefore can interfere. This interference, also known as Fano interference, produces the asymmetric line shape of the ASK resonance in the  $dI/dV$  spectra. In order to account for this interference, the effect of the tip needs to be taken into account when modeling the system. The Hamiltonian of Section 1.1 is then rewritten by adding two terms

$$H = H_{Anderson} + \sum_{\sigma} (\epsilon_t t_{\sigma}^{\dagger} t_{\sigma} + \hat{M}) , \quad (2.14)$$

where  $\epsilon_t$  is the energy of the tip with a single state and  $t$  ( $t^{\dagger}$ ) is the operator removing (creating)

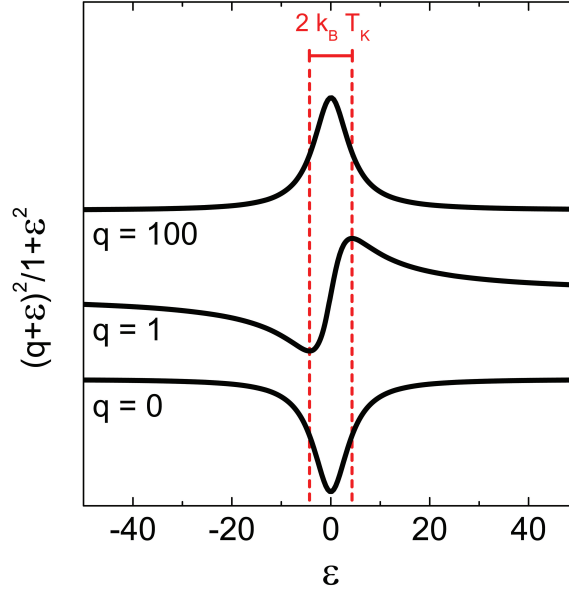


Figure 2.12: Simulated Fano line shapes for different values of  $q$ .

an electron in the energy of the tip. The Kondo resonance is treated here as it were a discrete energy level of an atom.  $\hat{M}$  accounts for the transfer Hamiltonian from tip to surface, and is expressed as

$$\hat{M} = (M_{at}a^\dagger t + \text{H.c.}) + \sum_k (M_{kt}c_k^\dagger t + \text{H.c.}) . \quad (2.15)$$

$M_{at}$  is the tunnel matrix elements linking the initial electronic state in the tip to the Kondo resonance or the spin state of the magnetic impurity, and  $M_{kt}$  for the tip to the conduction band of the surface, respectively. Using this Hamiltonian, it is then possible to show [85] that the differential conductance is

$$\frac{dI}{dV} \propto \frac{(q + \tilde{\epsilon})^2}{1 + \tilde{\epsilon}^2} . \quad (2.16)$$

The normalized energy  $\tilde{\epsilon}$  is defined as

$$\tilde{\epsilon} = \frac{E - \epsilon_K}{\Delta_K/2} , \quad (2.17)$$

where  $\epsilon_K$  is the position of the Kondo resonance. The line shape of the spectra is determined by the Fano parameter  $q$  which is the ratio between two tunneling channels (path 1 and 2).

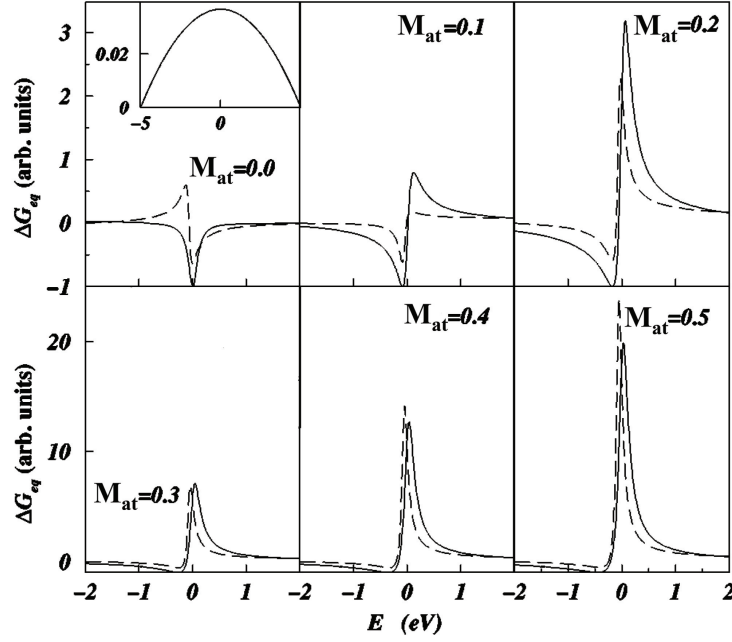


Figure 2.13: Differential conductance of a Kondo impurity for different  $M_{at}$ . The solid line denotes the differential conductance when the surface DOS is centered at 0 eV. The dotted line corresponds to the differential conductance when the surface DOS is shifted by 3 eV. The inset presents the model DOS centered at 0 eV [86].

This parameter is given by

$$q = \frac{A}{B}, \quad (2.18)$$

where

$$\begin{aligned} A(\epsilon) &= M_{at} + \sum_k M_{kt} V_k P\left(\frac{1}{\epsilon - \epsilon_K}\right), \\ B(\epsilon) &= \pi \sum_k M_{kt} V_k \delta(\epsilon - \epsilon_K). \end{aligned} \quad (2.19)$$

The first term in  $A$  accounts for the tunneling from the tip into the Kondo resonance. The second term in  $A$  describes the tunneling from the tip to the Kondo resonance via virtual transitions with the conduction electrons.  $B$  and the second term in  $A$  are linked through a Hilbert transformation.  $B$  denotes the coupling of the tip to the conduction band of the host metal. If  $q \gg 1$ , the resonance becomes peak-like (Fig. 2.12). For  $q = 0$ , the resonance is detected as a dip. An intermediate value of  $q$  gives an asymmetric line shape. When the



surface band structure is energy independent, the second term in  $A$  vanishes. In this case, when  $q \gg 1$ , tunneling occurs mainly through the Kondo resonance [Fig. 2.11(a)], while the tunneling into the substrate is dominant for  $q = 0$  [Fig. 2.11(b)]. Usually, however, the surface band structure is energy dependent. The second term in  $A$  is then non-zero and can affect the Fano line shape. An example is shown in Fig. 2.13. The surface DOS is assumed to vary elliptically with energy (Inset of Fig. 2.13). A shift of the band by 3 eV profoundly affects the lineshape as shown in Fig. 2.13. When  $M_{at} = 0$ , depending on the band structure, the Kondo resonance is detected as a dip (no shift of the surface DOS) or as an asymmetric shape (3 eV shift). With increasing  $M_{at}$ ,  $q$  increases recovering a peak-like shape.

### 2.4.2 Kondo effect with two atoms

STM allows us to manipulate molecules and atoms on a surface [87]. Thanks to the precise control which can be exerted, it is possible for the STM user to build artificial structures at the nanoscale. In this regard, the interaction between two Kondo impurities has been studied actively. As detailed in Section 1.3.3, two interacting Kondo impurities can exhibit a variety of ground states depending on the relative strengths of their Kondo temperature and magnetic couplings. Here we present some recent STM results obtained with two interacting Kondo impurities on a surface.

One of the first studies of this kind was reported by Wahl *et al.* [88]. The distance between two Co adatoms on Cu(100) was varied and  $dI/dV$  spectra were acquired to monitor the changes in the ASK resonance [Fig. 2.14(a)]. As long as the interatomic distance exceeds 6 Å, each Co adatom exhibits an unperturbed Kondo resonance. Below 6 Å, the Kondo ground state of the two Co atoms is perturbed through an exchange interaction. The sign of the exchange interaction depends on the Co-Co distance. At 5.12 Å, the exchange coupling is AFM and the Kondo resonance splits apart (Section 1.3.3). The resonance splitting is however not sufficiently strong in order to be detected in the  $dI/dV$  spectrum. Rather, a broadened line width is instead observed. At 2.54 Å, the two Co atoms couple instead ferromagnetically and the new Kondo temperature is given by  $T_K^N = T_K^2/|I|$  (Section 1.3.3) [47]. Since no spectral feature appears in the  $dI/dV$  spectrum, this means that  $T_K^N \ll T$ , *i.e.* the new Kondo ground state is lost at the working temperature  $T$ . Recently, Bork *et al.* performed a similar experiment [90] by attaching a Co atom on the tip and approaching the tip into contact with a Co adatom on the Au(111) surface. In another experiment, Neel *et al.* constructed  $\text{CoCu}_n\text{Co}$  chains to adjust

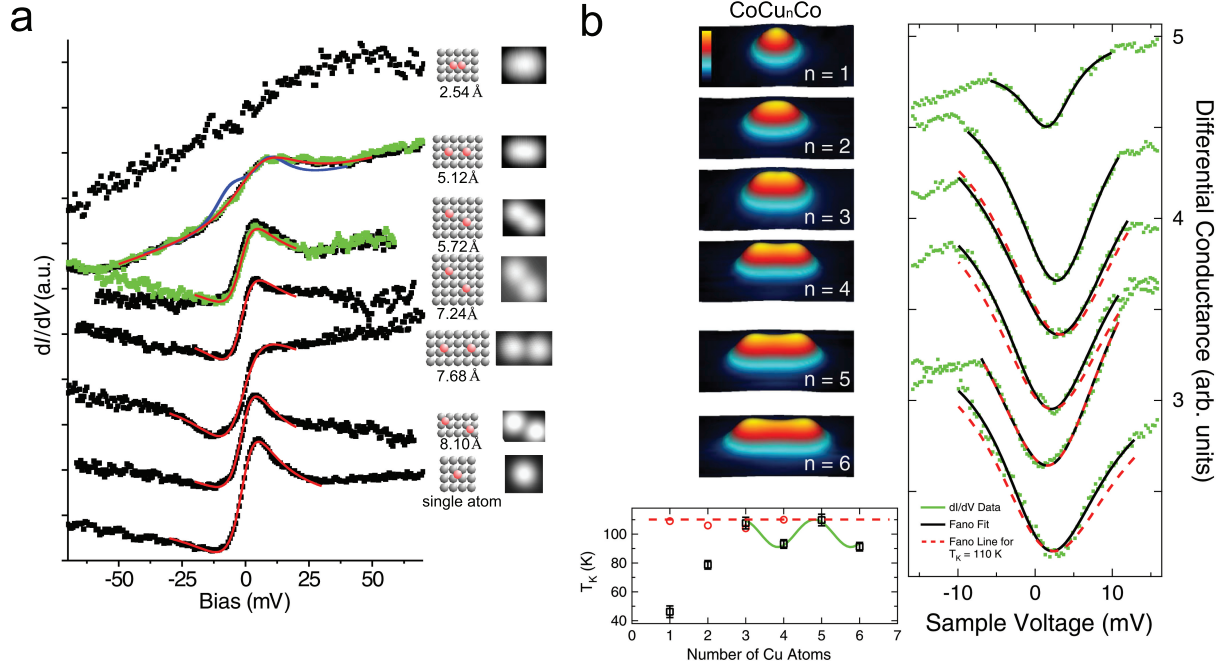


Figure 2.14: Kondo resonance measured on Co dimers on Cu(100) and  $\text{CoCu}_n\text{Co}$  chains on Cu(111). (a) The  $dI/dV$  spectra with varying distance between two Co adatoms on Cu(100). Right panels show the models and topography images [88]. (b) Spectroscopy above a Co atom of a  $\text{CoCu}_n\text{Co}$  chain with different number of Cu atoms on Cu(111). The left bottom panel shows the oscillatory behavior of  $T_K$  as a function of number of Cu atoms in a  $\text{CoCu}_n\text{Co}$  chain [89].

the distance between two Co atoms [89]. Here again, depending on the length of the chain, a different exchange interaction is produced. For  $n = 1$ , the interaction is FM; for  $n = 2$  the interaction is AFM. In the AFM case, no resonance splitting is observed, but only a broadened feature. An oscillation for  $T_K$  was evidenced with  $n \geq 3$  due to a RKKY interaction mediated by the Cu atoms between two Co atoms [Fig. 2.14(b)].

## Summary and conclusions

In this Chapter, we described the experimental setup employed in this Thesis. After a brief introduction of the working principle of STM, we detailed how the Kondo resonance is detected in an STM. We showed that the line shape of the Kondo resonance can be understood in terms of a Fano interference between two tunneling channels: one through the magnetic atom on the

surface (Kondo process) and one to the surface (non-Kondo process). The electronic structure of the substrate as well as the weight of each tunneling channel determine the characteristics of Kondo resonance including  $q$ ,  $\epsilon_K$  and  $T_K$ . We also showed that the Kondo temperature of adatoms on the surface is weaker than their bulk counterpart. Finally, we presented recent STM results on two interacting magnetic atoms. As we discussed, STM is the privileged tool for such studies, since atom-atom distance may be carefully tuned and eventually changed through a tip-assisted manipulation.

## CHAPTER 3

# Conductance-driven Kondo effect in a single cobalt atom

The performance of point-contact measurements can be monitored by the conductance, which allows then to define three transport regimes: tunneling, transition and contact. In this chapter, we explore the electrical conductance from tunneling to contact regime focusing on the spectroscopy of the differential conductance of a single magnetic atom. The electron transport properties of conductors at the atomic scale are of importance and the continuous effort is devoted to the miniaturization of electronic circuits. Quantum effects, charge transfer and energy dissipation are expected to play a central role. In Section 3.1 we briefly describe the quantum transport properties through single atoms and introduce in this regard the Landauer formulation of the problem. The mechanical properties of the point contact can strongly impact the conductance of the contact by atomic relaxations. This is presented in Section 3.2. Finally, the evolution of the Kondo effect of a single atom from tunneling to contact is discussed in Section 3.3. We show how the total conductance of the junction drives the change of the Kondo effect via atomic relaxations.

### 3.1 Quantum point contacts

At the macroscopic scale, the transport properties of conductors are determined by Ohm's law. The conductance  $G$  is then

$$G = \sigma \frac{S}{L} \quad (3.1)$$

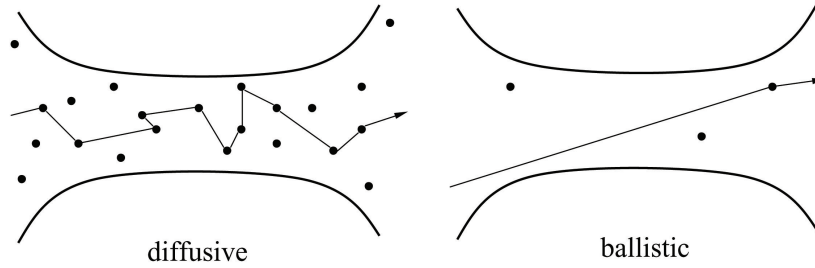


Figure 3.1: Schematics of a diffusive and a ballistic transport [91].

where  $\sigma$  is the conductivity of a material,  $S$  is the transverse area where electrons flow through, and  $L$  is the typical length scale of the sample. Ohm's law applies in the diffusive regime where, as shown in Fig. 3.1, the elastic mean-free path  $\ell$  of an electron is smaller than  $L$ . The elastic mean-free path corresponds to the average distance between two elastic collisions of an electron with the impurities in a metal. The conductance of a point-contact in the diffusive regime was first studied by Maxwell in 1873 [92]. In the classical limit, Maxwell found that the conductance is given by  $G_M = 2a/\varrho = 2a\sigma$  where  $a$  is the radius of the orifice and  $\varrho$  is the resistivity. At the atomic scale however, the transport properties are no longer diffusive. In the case of  $\ell \gg L$  [Fig. 3.1], the system enters in the ballistic regime where electron scattering is only induced at the boundaries of the conductor. For the ballistic transport, Sharvin showed in the semiclassical approximation [93] that the conductance is driven by solving the Laplace equation as  $G_S = e^2 k_F^2 a^2 / (2h)$  with the Fermi wave vector  $k_F$ , the electron charge  $e$  and Planck's constant  $h$ . The Sharvin conductance  $G_S$  has a contribution only from the electron density through  $k_F$ , and not from  $\sigma$  or  $L$ .

The conductance of a quantum point contact was instead described by the pioneering work of Landauer in 1957 [95]. In a quantum point contact, electron transport is still ballistic, but the contact radius is comparable to the Fermi wavelength  $a \sim k_F$ . The electron motion is laterally confined within the hard wall of the conductor (Fig. 3.2) so that the transverse momentum of electrons is quantized. The electrons propagate instead as plane waves along the longitudinal channels. The quantized transverse electron momentum in the contact constriction leads to the quantization of the conductance which can be explained by a simple model [96]. Figure 3.2 shows the quantized conductance in an atomic-sized conductor between two electrodes (tip and sample). The confined electron motion within the conductor in the transverse direction is

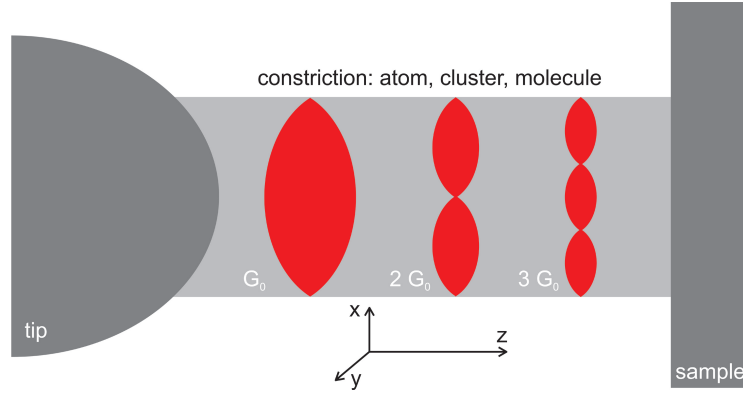


Figure 3.2: Conductance quantization in an atomic-sized conductor between two electrodes (tip and sample). The 1, 2, 3 eigenmodes are presented as standing waves with 1, 2, 3 antinodes each giving a quantum of conductance  $G_0$  [94].

illustrated assuming the potential is flat over the conductor. The three eigenmodes are shown as standing waves, which give a quantum of conductance  $G_0$  for each antinode. The quantum of conductance is  $G_0 = \frac{2e^2}{h} = 77.48 \mu\text{S}$ , which corresponds to a resistance of 12.9 k $\Omega$ . Here, the energy of the electron can be written as

$$E = E_i + \frac{\hbar^2 k^2}{2m_e}, \quad (3.2)$$

where  $E_i$  is the transverse mode energy,  $k$  is the wave vector along  $z$ , and  $m_e$  is the free electron mass. A net current caused from the coupling of the conductor to two reservoirs with potential difference  $V$  can be given as

$$I_i = e^2 V \rho_i(E_F) v_i(E_F) \quad (3.3)$$

in the  $i$ -th channel for  $E_i < E_F$  [96]. Since only electrons in a narrow region around the Fermi energy contribute to the current, the density of states ( $\rho_i$ ) and the group velocity ( $v_i$ ) are evaluated at  $E_F$ . Every mode  $i$  carries a one-dimensional electron gas with  $\rho_i = 2/(\hbar v_i)$  resulting in a total conductance as

$$G = \frac{1}{V} \sum_i I_i = G_0 \sum_i \Theta(E_F - E_i) = G_0 n, \quad (3.4)$$

where  $n$  is the number of open transverse modes or conductance channels and  $\Theta$  is the Heaviside step function. Standing waves with  $n$  antinodes are given by changing the energy of ballistic

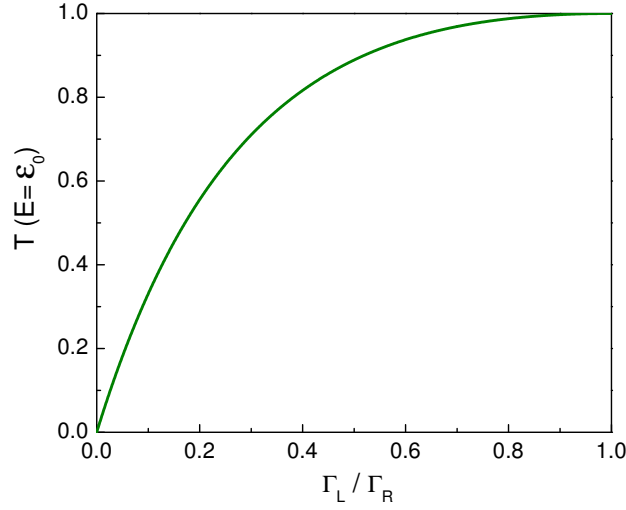


Figure 3.3: Transmission probability as a function of  $\Gamma_L/\Gamma_R$  when  $E = \epsilon_0$ .

transferred electrons. Each antinode adds one quantum of conductance  $G_0$ . Integer values of  $G_0$  indicate quantized conductance due to laterally confined quantum modes in the conductor.

This conductance quantization is consistent with the multichannel expression proposed by Landauer [95,97–100]. Landauer showed that the conductance of a conductor can be expressed as

$$G = G_0 \sum_{i,j=1}^n |\tau_{ij}|^2, \quad (3.5)$$

where  $|\tau_{ij}|^2$  specifies the transmission probability of an electron incident on the contact mode  $i$  and transmitted into mode  $j$ . Büttiker suggested another set of modes as eigenchannels which is not mixed in the scattering region of the quantum point contact [97]. As a consequence the transmission probability  $|\tau_{ij}|^2$  in Eq. (3.5) becomes  $T_i \delta_{ij}$  where  $T_i$  is the transmission probability of the  $i$ -th eigenchannel. The transformation of arbitrary channels into eigenchannels was given by Brandbyge and Jacobsen [101]. The number of eigenchannels is controlled by the number of valence orbitals in the atom. In other words, the channels are a linear combination of the atomic orbital such as  $s$ ,  $p$ ,  $d$  orbitals of the atom. Therefore, the transmission probability of the  $i$ -th eigenchannel  $T_i$  corresponds to the transmission of one orbital of atom. The transmission of one orbital of atom  $T$  can be expressed as

$$T = \frac{4\Gamma_L\Gamma_R}{(E - \epsilon_0)^2 + (\Gamma_L + \Gamma_R)^2} \quad (3.6)$$

where  $E$  is the bias applied to the system,  $\epsilon_0$  denotes the orbital energy level and  $\Gamma_{L(R)}$  is the coupling between left (right) electrode and the atomic-sized contact. If the coupling becomes asymmetric,  $T$  drops drastically (Fig. 3.3). And as long as the cross section of the quantum point contact changes slowly with the constriction,  $T_i$  will be either 1 or 0 [102–105]. If the smearing due to finite temperatures or any effect from the internal disorder and inelastic impurity scattering is neglected, the sum of transmission probabilities will be integer values. The conductance will then be quantized in units of  $G_0$ .

To study the conductance of atomic-sized contacts, a variety of experiments using the tip of STM were performed [91, 106–108]. These experiments were carried by bringing the tip into the pristine surface forming a contact. In these experiments, contact formation is monitored by recording the current at a fixed junction voltage. Instead of limiting investigations to tip-surface point contacts, tip contacts can be also performed with single atoms or molecules adsorbed on a metal surface as shown in recent STM experiments [60, 109–116]. Tip-adsorbate contacts turn out to be highly reproducible and stable contrary to tip-surface contacts. Single-atom or single-molecule junctions can be formed in this way with an increased control compared to other experimental techniques. The electrodes (the tip and the surface) and the contact constriction (the atom or the molecule) can be in fact characterized prior to and after the contact. Section 3.1.1 describes contacts to individual adsorbed atoms (adatoms) on surfaces. All the experiments carried out on single adatoms were pursued at cryogenic temperature, since under ambient thermal conditions, atoms diffuse to the step edges of the crystal.

### 3.1.1 Conductance of a single atom using STM

In a pioneering work, Yazdani *et al.* investigated the controlled contact of an STM tip to individual adsorbed xenon atoms adsorbed on a Ni(110) surface [117]. The conductance of individual Xe atoms was studied using a bare W-tip and a tip terminated by a xenon atom (Fig. 3.4). The conductance curves as a function of a tip displacement using a single Xe atom terminated tip shows a smooth transition from tunneling to contact, while an abrupt jump-to-contact was observed with a bare W-tip. The jump-to-contact corresponds to a sudden vertical displacement of the Xe atom towards the tip. The Xe atom is then nearly centered between the surface and the tip. The jump-to-contact occurs at  $0.2 G_0$  and signals that the system enters the contact regime.

The contact to metallic adatoms was first carried out by Limot *et al.* [60] and Néel *et*



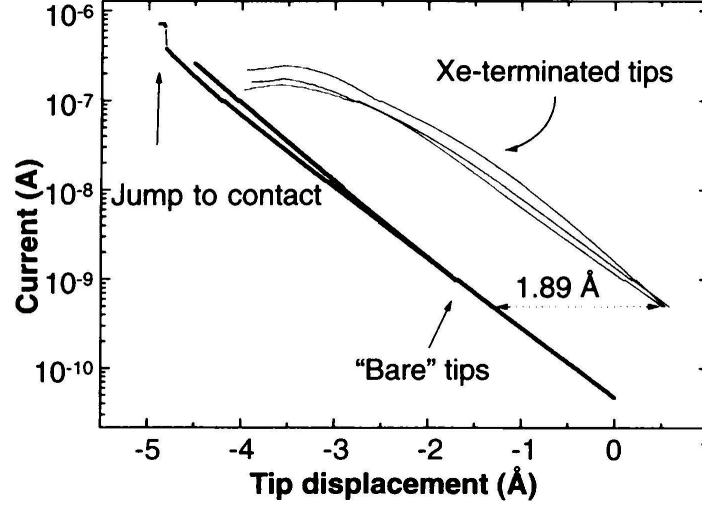


Figure 3.4: Current as a function of the tip displacement at  $-10$  mV using bare tungsten and Xe-terminated tips above a Xe atom on Ni(110) [117].

*al.* [109, 112, 118, 119]. Contrary to the contact experiments with a W-tip reported by Yazdani *et al.* [117], a continuous transition from tunneling to contact was observed with the metallic adatoms on the surface. Figure 3.5 presents a conductance curve for a Cu adatom on Cu(111) surface in a logarithmic scale, where  $z$  denotes the tip displacement. The dashed lines mark the boundaries among three transport regimes, which we describe hereafter. Well below  $G_0$ , the conductance varies exponentially with the distance and this behavior is defined in the tunneling regime. In a one-dimensional description of the tunneling barrier [120] [see also Sec. 2.2], the apparent barrier height can be written as

$$\Phi[\text{eV}] = 0.952[\text{eV } \text{\AA}^2] \left( \frac{\ln I}{z[\text{\AA}]} \right)^2. \quad (3.7)$$

Table 3.1 contains a collection of apparent barrier heights obtained for clean surfaces and for single adsorbed atoms according to Eq. (3.7). A difference is observed between the apparent barrier height of the individual adatom and the corresponding surface. This can be related to the dipole moment of the adatom which is induced by charge transfer to the surface.

When the conductance is close to  $G_0$ , the system enters the contact regime. Within the time resolution accessible experimentally, no jump-to-contact is observed on the conductance of adatoms on the surface. The continuous transition between tunneling and contact regimes is

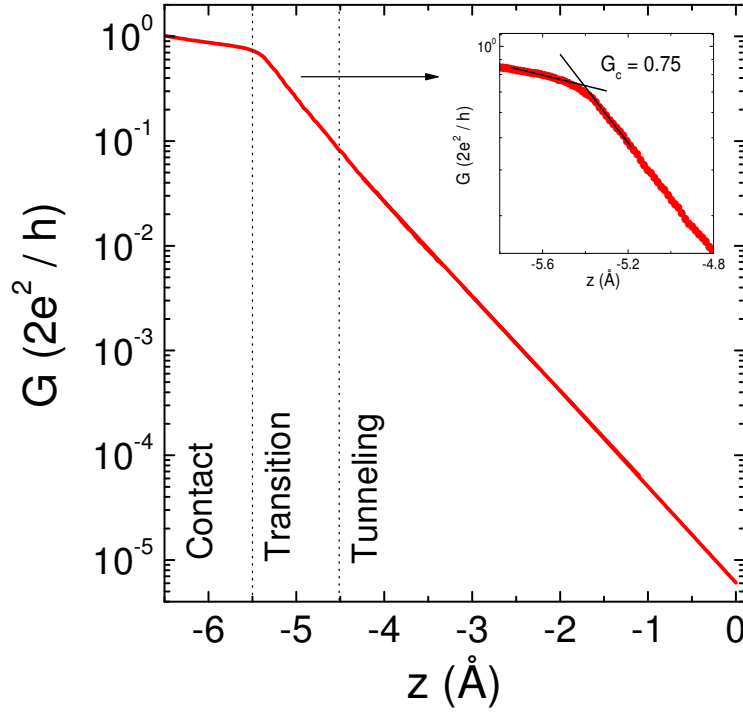


Figure 3.5: Conductance versus tip displacement of a single-adsorbed Cu atom on a Cu(111) surface. Inset: Close-up view of the transition between the tunneling and contact regimes showing how to define the contact conductance ( $G_c$ ).

due to the redistribution of surface charge mentioned above, which then enhances the bonding of the atom to the surface. The bond between the adatom and the surface has in fact a larger stiffness according to the increased elastic constants with respect to flat surfaces [60, 121]. Limot *et al.* [60] showed that the tip-adatom interaction then leads well below the threshold value needed to produce a jump-to-contact. The absence of a jump-to-contact above atoms is common for many metals. In some cases, a specific configuration and material composition of the electrodes before contact may however favor a jump-to-contact [122]. This is also the case of the xenon experiment reported by Yazdani *et al.*, where the closed shells of Xe must minimize charge transfer to the surface.

Given the absence of a jump-to-contact, the contact conductance  $G_c$  is defined as the conductance where a change of slope occurs. As shown in Fig. 3.5, a third regime in fact subsists between the tunneling and the contact regime. In Sec. 3.2, we show that this regime, defined as the transition regime, is characterized by the presence of atomic relaxations, which sets in approximately 1 Å before contact. The change of slope between the transition and the

	$\Phi$ (eV)	$G_c$ ( $G_0$ )	Reference
Ag(111)	4.4	1.5	Limot <i>et al.</i> [60]
Au(111)	4.0	1.0	Kröger <i>et al.</i> [111]
Cu(111)	4.7	1.1	Limot <i>et al.</i> [60]
Ag(111)-Ag	4.6	0.8	Limot <i>et al.</i> [60]
Au(111)-Au	5.0	0.9	Kröger <i>et al.</i> [111]
Cu(111)-Cu	5.3	0.9	Limot <i>et al.</i> [60]
Cu(111)-Co	4.2	1.0	Néel <i>et al.</i> [118]
Cu(100)-Co	3.0	1.0	Néel <i>et al.</i> [109]

Table 3.1: Apparent barrier heights ( $\Phi$ ) and contact conductance ( $G_c$ ) for various surfaces and adatoms [94].

contact regime then defines  $G_c$ . The contact conductance may then be estimated following a geometrical approach as shown in Fig. 3.5 [118].

A single conductance channel can be expected for noble metal atoms which are monovalent. For the contact conductance,  $1 G_0$  should be yielded as long as the transmission probability equals 1. In reality,  $G_c$  of noble adatoms is not  $1 G_0$  as seen in Tab. 3.1. According to Eq. (3.5), the contact conductance is a sum over each of the conductance eigenchannels with a certain transmission probability. A monovalent atom has simply  $G = \tau G_0$ . Therefore the difference of the contact conductance from  $1 G_0$  to  $\tau G_0$  comes from the difference of the transmission probability. As mentioned in Eq. (3.6), the transmission probability is proportional to the coupling of the atom to the metallic leads (tip and surface). To obtain a transmission probability of 1, the leads should be also defect- and excitation-free which is not physically possible. A number of corrections which reduce the total conductance are caused by the scattering near the contact. Therefore the experimentally obtained  $G_c$  of noble adatoms is lower than the ideal  $G_c$ ,  $1 G_0$ .

## 3.2 Atomic relaxations near point contact

The close proximity of a tip to a surface produces changes in the conductance [123], but also introduces short range adhesive forces acting between tip and sample [124]. The transition regime is therefore affected by structural relaxations induced by these adhesive forces, which

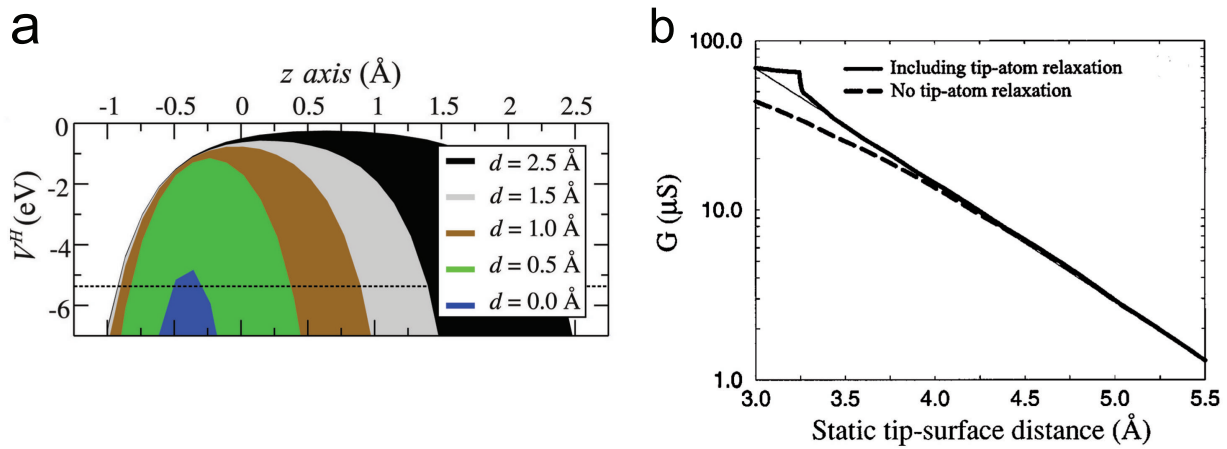


Figure 3.6: The collapse of the tunnel barrier and the calculated conductance. (a) Cross section of the Hartree potential along the  $z$  axis at different distances  $d$  between the tip and the sample for Pt/Pt(111) [126]. The collapse of the tunnel barrier is evidenced when the distance  $d$  decreases. (b) Calculated conductance as a function of the static distance for an Au(111) surface and an Au tip. Full curve: with atomic relaxations; dashed curve: without. Adapted from [127].

also modify the surface and tip electronic structure. Independently on atomic relaxations, the tunneling barrier progressively collapses in this regime. The transport regime gradually changes from tunneling to ballistic [125] over approximately 1 Å as shown in Figure 3.6(a). In practice, an accurate *ab initio* description of the conductance in the transition regime is difficult as all these factors play a role.

The collapse of the tunneling barrier is associated to charge accumulation which affects the orientation and energy of atomic orbitals and leads to a saturation of the conductance [123,128,129] via elastic multiple scattering processes [130]. Figure 3.6(b) shows a density functional theory (DFT) calculation by Olesen *et al.* for the conductance between a Au tip and a Au(111) surface. The dashed curve presents the case of a static tip and surface, where it can be seen that the conductance should saturate close to point contact. A static distance means the tip-surface distance in the absence of relaxations. The behavior of the conductance is in apparent contradiction with the exponential variation of the conductance up to point contact seen experimentally (see for example Fig. 3.5). This apparent discrepancy is due to the presence of atomic relaxations. When the relaxations are included (full bold black curve), the saturation is compensated by the attraction of the tip atom towards the surface, because the actual tip-sample distance is shorter than the static one. In addition to this “mechanical” effect, atomic

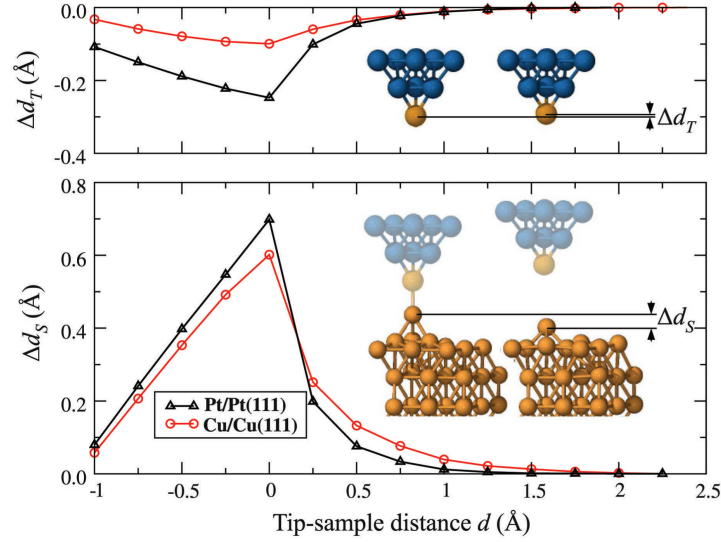


Figure 3.7: Atomic relaxations near point contact. Relaxation of tip apex atom towards the surface (top) and of the adatom on the surface towards the tip (bottom) for Pt-Pt(111) and Cu-Cu(111) systems. The stick-ball model shows how the tip and adatom are relaxed near point contact [126].

relaxations may also change the electronic structure of the tip and surface, which in turn also impact the conductance. Depending on tip geometry and material, the conductance in the transition regime may deviate or not from the exponential behavior of the tunneling regime.

The scenario for a tip-atom contact is similar to the one described above for a tip-surface contact. Figure 3.7 describes the simulated atomic relaxation of the tip apex and adatom on the surface. As shown, approximately 1 Å before the contact, the adatom on the surface starts to interact with an atom at the tip apex. Adhesive forces tend to stretch the tip and the atom towards each other. Contact is established once the changes in the atomic distances are maximized. In the contact regime, the adatom is pressed back into the surface while the tip is compressed. The maximum tip displacement which may be achieved in the contact regime depends on tip and surface structure. An open structure, e.g. a (100) surface, will allow larger tip excursions compared to a compact structure, e.g. a (111) surface.

The experimental characterization of atomic relaxations is possible by directly measuring both the conductance and the adhesives force. Nowadays, this can be routinely observed by combined STM/AFM microscopes [132–136]. Another possibility to detect atomic relaxations is to perform STS. Atomic relaxations may then be indirectly monitored through the changes

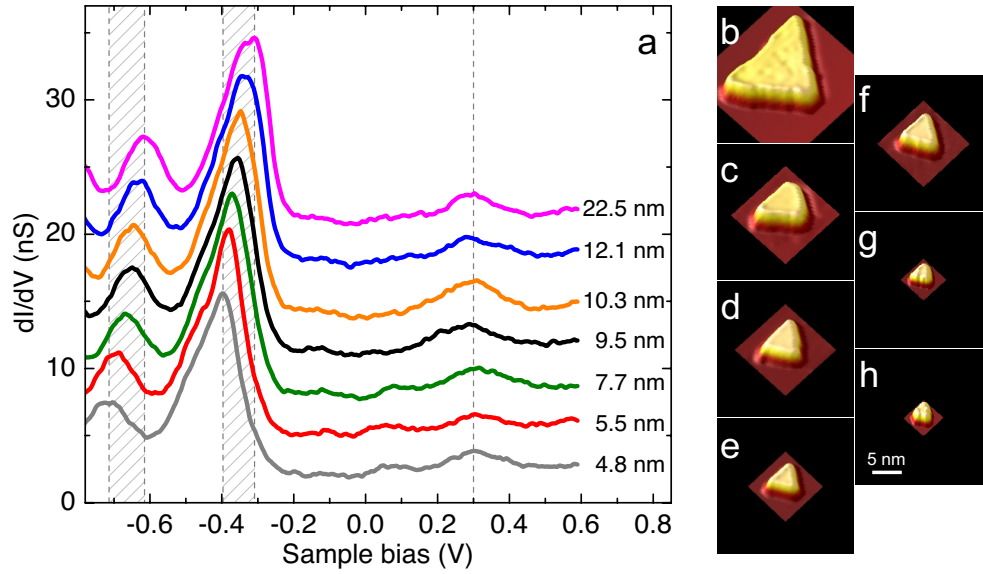


Figure 3.8: (a)  $dI/dV$  spectra above Co nanoislands of increasing size and corresponding topographic images [(b)—(h)] [131]. Feedback opened at 1.5 nA, 0.6 V. Spectra over the islands with edge sizes of 5.5, 7.7, 9.5, 10.3, 12.1, 22.5 nm are vertically shifted upward by 3, 6, 9, 12, 16, 19 nS, respectively. The hatched areas delimit the range over which an energy shift is observed for the peaks.

induced in the electronic structure of the junction. An example is the accelerated Stark shift detected for the Shockley surface states of Ag, Cu and Au(111) when the tip is in close proximity with the surface [137, 138]. More generally, it is widely known that the electronic states of a crystal can be changed by tuning the interatomic distances. Epitaxial systems offer an interesting approach in this regard as the bond lengths between the metal atoms in the supported film are different from those in the parent metals, resulting in strain. For example, the growth of one monolayer of copper on Ru(0001) results in a Cu(111) surface with an expanded lattice of approximately 6% [139]. Accordingly, the Shockley surface states are shifted upward in energy by 0.7 eV as shown by STS measurements. Strain affects also the properties of electronic states in nanoscale systems. In these systems, strain is produced by the lattice mismatch with the metal substrate—and, to some extent in heteroepitaxial systems, by the nature of the bonding interactions island-substrate interface. For example Co nanoislands grown on Cu(111) have minority  $d$  states that shift in energy with island size [Fig. 3.8] [131]. These  $d$  states are easily detected in STS and may be used as a spectroscopic marker to probe changes in the atomic relaxation among and within islands. In the following Section, we also use STS to detect atomic

relaxations. In particular we focus on the Kondo effect in the conductance of a single atom and show through STS how the Kondo effect is exponentially sensitive to structural changes.

### 3.3 Conductance-driven change of the Kondo effect

Zero-bias anomalies in the conductance represent an opportunity for detecting and eventually controlling nanomagnetic phenomena by means of the total conductance. The most known example is the Abrikosov-Suhl-Kondo (ASK) resonance, which is introduced in Chapter 1. The Kondo effect has been evidenced in the conductance of lithographically defined quantum dots [5,6], carbon nanotubes [25], or single molecules [11,26–28] coupled to metallic electrodes. A fine tuning of the impurity-electrode hybridization could provide an interesting way to test the impact of structural changes on Kondo correlations [29,30]. To date, however, the lack of control over this hybridization has resulted in a strongly device-dependent effect. It was recognized quite early—for example, by exerting an hydrostatic pressure on the host crystal [21]—that the Kondo effect is in fact exponentially sensitive to these changes. More recently, by employing an STM, a similar result was achieved with a single atom. The Kondo effect of the atom was modified through the crystal structure of the host surface [77,78], or through the strain affecting the atom environment [140,141].

Following the seminal point-contact study by Yanson *et al.* [142], the ASK resonance has also been observed on rare occasions in well-controlled two-terminal devices where a single atom adsorbed onto a metal surface is brought into contact with the tip of an STM. Surprisingly, the ASK resonance was shown to be little affected by structural changes induced by the tip-atom contact [90,109,143]. Motivated by this apparent discrepancy, we revisit in this Section the tip contact with a Co atom on Cu(100). We show, unlike Néel *et al.* [109], that atomic relaxations produced by the tip displacement continuously affect both the ASK resonance and the conductance prior to and after tip contact. A reproducible exponential variation of the ASK line width with the conductance is evidenced and explained through an Anderson-based model. Our findings demonstrate that the Kondo effect of single atoms adsorbed on a metal surface, and more generally their magnetism, may be tuned via the ballistic conductance of the junction.

Theoretical support to the results presented was provided by **Pascal Simmon**<sup>1</sup>

---

<sup>1</sup>Laboratoire de Physique des Solides, CNRS, Université Paris Sud at Orsay, France

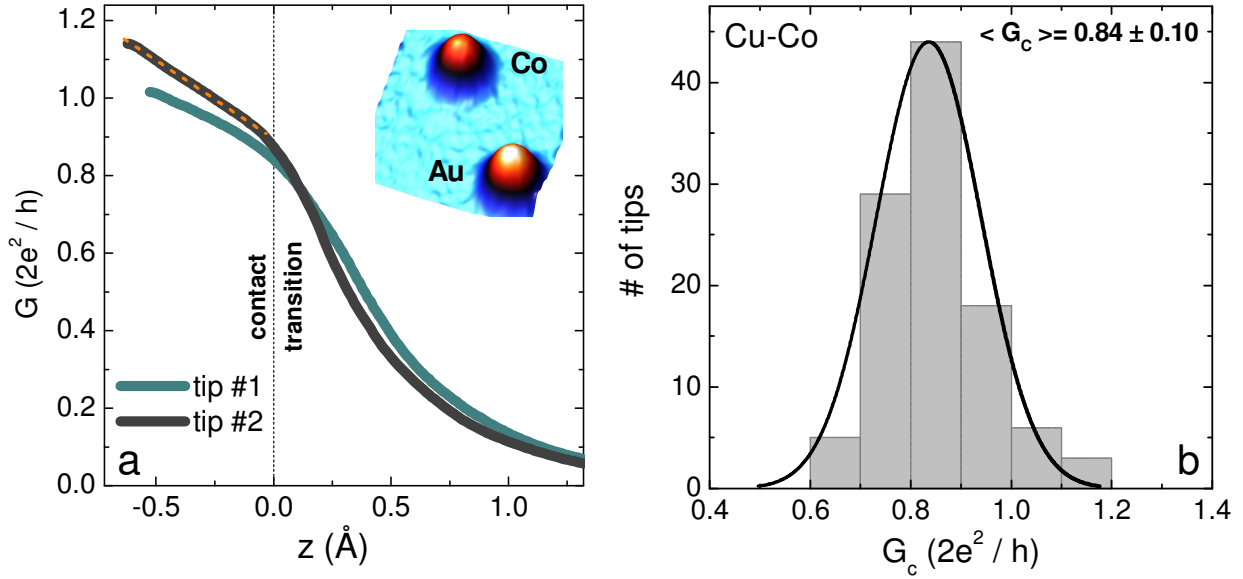


Figure 3.9: Evolution of the conductance with two different tips. (a) Typical conductance versus tip displacement for two tips above a Co atom on Cu(100) ( $V = -200$  mV) and linear fit to  $G(z)$  in the contact regime (see text). The vertical dashed line is positioned at  $z = 0$  where  $G = G_c$ . Inset: Constant-current image of Co and Au atoms on Cu(100) ( $13 \times 13 \text{ \AA}^2$ ,  $-200$  mV,  $1$  nA). Apparent heights are  $1.1$  and  $1.2 \text{ \AA}$  for Co and Au, respectively. The contact conductances amount to  $0.84$  and  $0.72$ , respectively. (b) Histogram of  $G_c$  for roughly 100 tips over Co atom on Cu(100).

### 3.3.1 Contact conductance over a Co adatom on Cu(100)

For this study, we employed etched W tips, which were cleaned by sputter/anneal cycles and coated with copper *in vacuo* by soft indentations into the clean Cu(100) surface. Tip status was monitored through STM images and controlled tip-atom contacts in order to select tips terminated by a single-copper atom [60]. Figure 3.9 presents the evolution of the conductance ( $G = I/V$ ) for two given copper-coated W tips as they are vertically displaced towards the center of a Co atom on Cu(100) (inset of Fig. 3.9). A tip displacement of  $z = 0$  defines the boundary between the transition regime ( $z > 0$ ) and the contact regime ( $z < 0$ ) —the  $z = 0$  boundary is deduced through  $G_c$ . As mentioned in Section 3.2, in the transition regime, electrons tunnel from the tip into the substrate, but the conductance is influenced by atomicscale relaxations [60, 126, 143]; the structural relaxations vanish once  $z \gtrsim 1 \text{ \AA}$  [not shown in Fig. 3.9(a)]. Figure 3.9(b) is the histogram of  $G_c$  for overall 100 tips over Co adatom on Cu(100). The statistical survey follows the Gaussian distribution and an average of  $\langle G_c \rangle = 0.84 \pm 0.09$  (in units of  $2e^2/h$ ) is



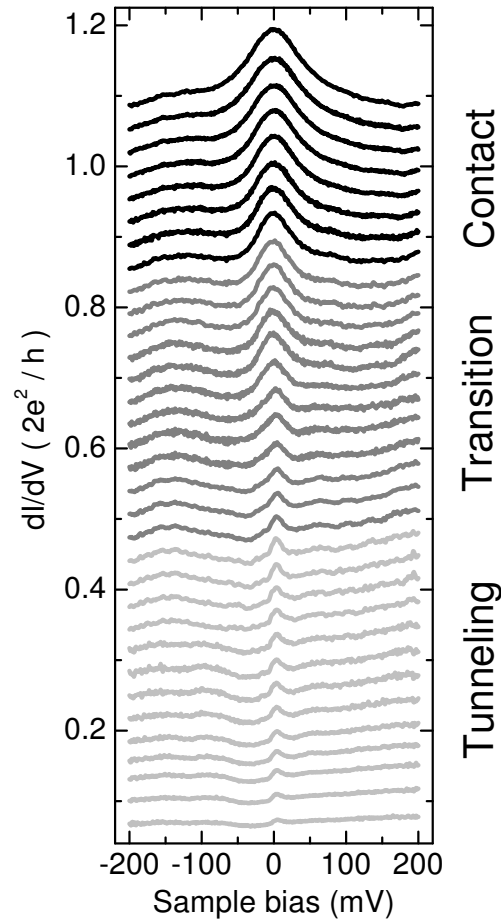


Figure 3.10: Evolution of the ASK resonance.  $dI/dV$  spectra from tunnel (solid light-grey lines) to contact (solid black lines), including spectra in the transition regime affected by atomic relaxations (solid dark-grey lines). All the data is fully reversible with tip displacement.

found. The contact formation between the tip and the Co atom is therefore highly reproducible and reversible as anticipated in Section 3.1.

In Fig. 3.10, the evolution of the Kondo resonance of Co/Cu(100) in the presence of a copper-coated W tip is shown. To do so, we freeze the geometry of the junction by opening the feedback loop at selected conductances and acquire a  $dI/dV$  spectrum. These conductances correspond to the value of the  $dI/dV$  at  $-200$  mV. Several orders of magnitude for the conductance were covered in this way, corresponding to a tip excursion of about  $5.5$  Å. In Fig. 3.10, we focus on the final  $2$  Å where substantial spectral changes are evidenced. An ASK resonance is detected at the Fermi level, but compared to the previous study [109], the line width evolves

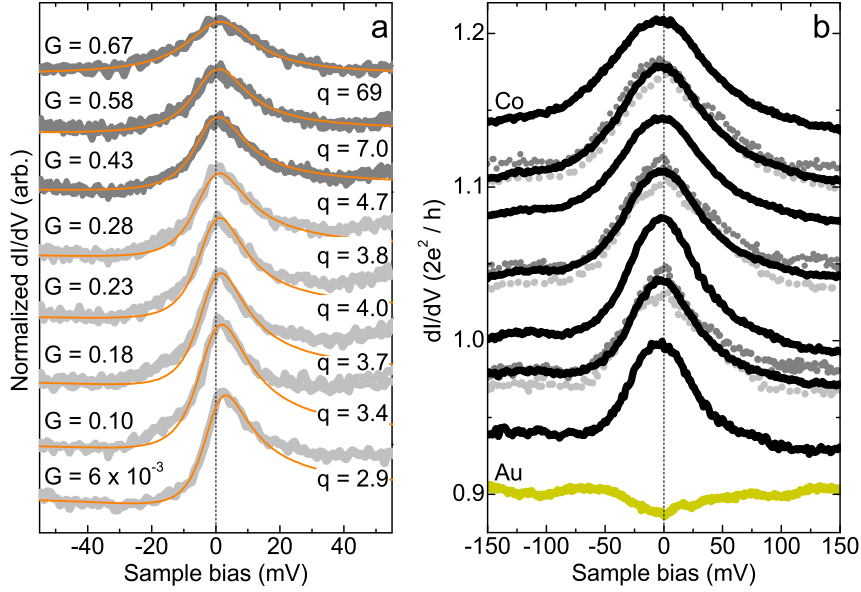


Figure 3.11: ASK resonance from transition to contact. (a)  $dI/dV$  spectra near the tunnel-to-transition regime. Spectra are renormalized by the conductance where the feedback loop was open (indicated on the figure). The solid lines are Fano fits as described in the text and  $q$  is the corresponding Fano parameter of each single fit. The ASK resonance is centered close to  $\epsilon_K = -1$  meV. (b)  $dI/dV$  spectra in the contact regime. We have included spectra acquired with two other tips (gray dotted lines, vertically displaced upward by 0.005; light-gray dotted lines displaced downward by  $-0.005$ ). The spectrum acquired in contact with a non-magnetic Au atom on Cu(100) is featureless. The vertical dashed line is positioned at zero bias.

continuously with increasing conductance. The color code employed in Fig. 3.10 reflects the different spectral regimes corresponding to tunneling, transition and contact regime.

### 3.3.2 Evolution of the Fano line shape

The resonance in the transition and tunneling regimes ( $z < 0$ ) is shown in Fig. 3.11(a). As presented in Section 2.4.1, the lineshape corresponds to a Fano line  $dI/dV \propto (q + \epsilon)^2 / (1 + \epsilon^2)$  [24, 86], where  $\epsilon = (eV - \epsilon_K) / k_B T_K$ ;  $q$  and  $\epsilon_K$  are the asymmetry parameter and the energy position of the resonance, respectively. The full width at half maximum (FWHM) of the ASK resonance is therefore equivalent to  $2k_B T_K$  [see Eq. (1.8)]. The resonance is detected as a steplike feature with a Fano parameter ranging from  $q = 2.9$  to  $4.7$  up to  $G = 0.43$  [light-grey spectra in Fig. 3.11(a)], which corresponds to  $z = 0.5$  Å. Starting here, the Fano parameter

increases rapidly until at  $G = 0.67$  ( $z = 0.25$  Å) the ASK line shape becomes peaklike [dark-grey spectra in Fig. 3.11(a)]. As mentioned in Section 2.4.1, the ratio between the indirect (tunneling through the Co atom) and direct tunneling paths (tunneling to the Cu surface) determines the value of the Fano parameter  $q$ , the ratio between the two paths depending on the surface and impurity electronic structure. The Kondo effect of Co has in fact been studied on various copper surfaces by tunneling spectroscopy and shown to be diplike on Cu(111) (corresponding to  $q = 0$ ) [76, 143], steplike on Cu(100) ( $q \sim 1$ ) [76], or peaklike on Cu(110) ( $q \gg 1$ ) [77]. The changes in the line shape we detect therefore reflect a modification in the local electronic structure that are assigned to the atomic relaxation present in the transition regime [86]. In particular, the increase in  $q$  indicates that the indirect tunneling path is steadily quenched. We have seen in Section 2.4.1 that  $q$  depends on  $M_{at}$ , which is the tunnel matrix element that connects the tip states to the discrete atomic  $d$ -resonance. The evolution of the Fano line shape therefore likely reflects an increase in  $M_{at}$  and therefore of the coupling  $\Gamma_t$  between the tip and the atom. This is consistent with the findings presented in Section 3.3.3, where  $\Gamma_t$  is shown to change by at least six orders of magnitude [see Fig. 3.14(b)], from a couple of neV in the tunneling regime up to a couple of meV at contact. The change of  $q$  would then reflect the exponential change of  $\Gamma_t$  in the transition regime.

As shown in Fig. 3.11(b), the spectral line shape remains peaklike in the contact regime up to the highest conductances explored. Further theoretical work, see for example [144, 145], is clearly needed to justify such a Fano line shape in the contact regime. We note however that a very satisfying agreement is found between our  $dI/dV$  data and simulations of the Kondo line shape [see Fig. 3.17(b)] carried out with a Frota function [146], which closely reproduces the exact solution that can be obtained with numerical-renormalization group theory [147]. Along with Co, we also monitored the  $dI/dV$  spectra on non-magnetic Au and Cu atoms. We have included in Fig. 3.11(b) a  $dI/dV$  spectrum acquired with the tip in contact with Au where, as expected, no ASK resonance is present.

### 3.3.3 The relation between $T_K$ and $G$

The changes in the line shape are also characterized by a concomitant increase of the FWHM, hence of  $T_K$ , which we plot in Fig. 3.12(a) as a function of tip displacement. For all tip apices employed, in the tunneling regime we find  $T_K = 90$  K in agreement with previous studies [76, 109]. However starting from  $z = 0.5$  Å,  $T_K$  increases and rapidly reaches a temperature close to 300 K

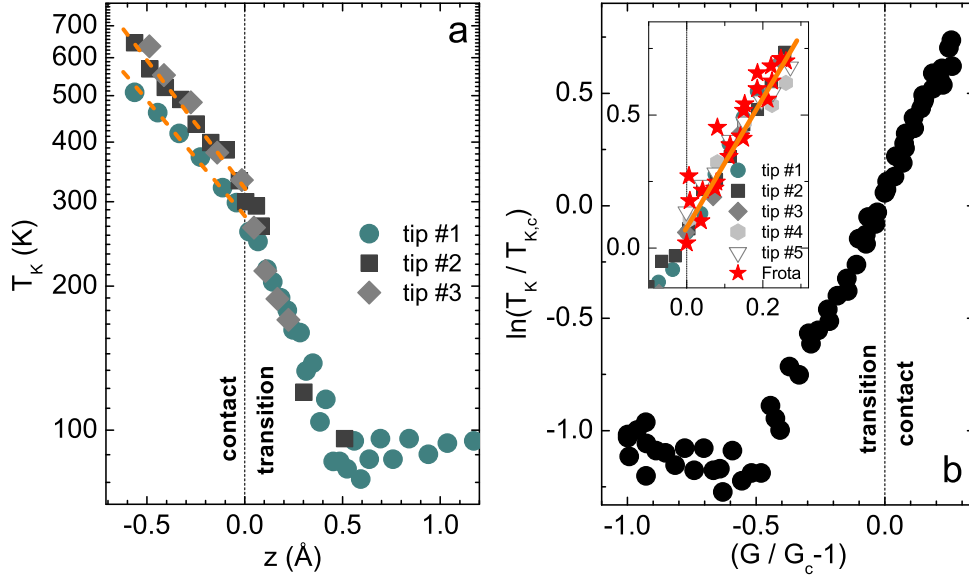


Figure 3.12: Evolution of the Kondo temperature. (a)  $T_K$  versus tip displacement. The solid lines correspond to the fits described in the text. (b)  $T_K$  versus conductance for various tips. The vertical dashed line is positioned at  $G = G_c$ .  $T_{K,c}$  is the Kondo temperature at  $z = 0$  and experimentally determined to be close to 300 K for all tips employed. Inset:  $T_K$  in the contact regime for five tips labeled 1, 2, 3, 4, 5 which have respectively, a contact conductance of  $G_c = 0.87, 0.90, 0.91, 0.90, 0.85$ . The solid line in the contact regime corresponds to the fit described in the text. The stars correspond to the data evaluated using Frota functions [see Section 3.3.4].

at  $z = 0$ . In the contact regime ( $z < 0$ ),  $T_K$  increases exponentially with  $z$ , but is tip-dependent. For some tips, values up to 650 K are found at  $z = -0.6$  Å (going beyond this tip excursion results in irreversible tip or surface modifications). The maximum value found for  $T_K$  is close to the one for Co in bulk *fcc* copper [4, 147], despite the lower coordination of Co in our junction. The Kondo temperature was extracted by Fano fits [see Fig. 3.11(a)], or alternatively by measuring in the contact regime the FWHM of the ASK resonance. Estimates of  $T_K$  change depending on the analytical function used to reproduce the ASK resonance. For example, if one follows [11], our  $T_K$  estimates need to be divided by  $\sqrt{2}$ . If one follows [147] [see Frota fit in Fig. 3.17(b)], our  $T_K$  estimates need to be divided by a factor 2. The evolution of  $T_K/T_{K,c}$  with conductance is however robust to the method used to estimate the Kondo temperature as shown in the inset of Fig. 3.12(b). Quite remarkably, the exponential dependency of the Kondo temperature on  $G$  is barely dependent on the tip employed. To further exemplify this,

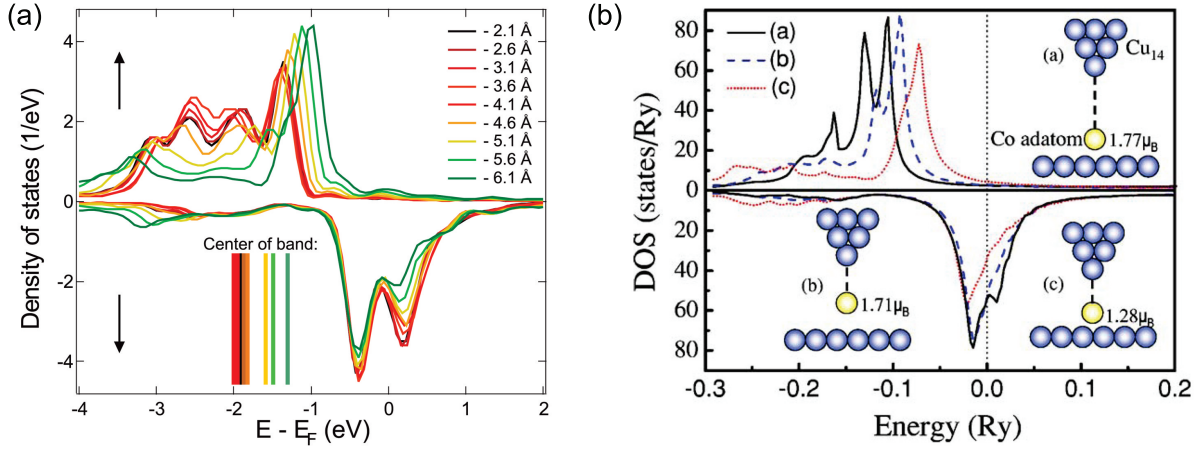


Figure 3.13: Density of  $d$  states of a Co adatom on Cu(100) for different tip displacements. (a) The spin-up states ( $\uparrow$ ) have positive amplitude, while the spin-down states ( $\downarrow$ ) have a negative amplitude. The  $d \uparrow$  band is shifted upwards towards  $E_F$  as the tip-atom distance decreases, while  $d \downarrow$  stays near  $E_F$  [109]. (b) DOS of a Co adatom on Cu(100) for three different tip separations. The influence of the STM tip on the electronic and magnetic properties in a relaxed geometry is shown [148].

Fig. 3.11(b) shows ASK resonances acquired with other tips (solid light gray and gray lines). The exponential dependency holds in the transition regime and eventually breaks down below  $G = 0.4$  ( $z = 0.5$  Å). When moving to even lower conductances,  $T_K$  slightly increases again.

To understand how  $T_K$  relates to  $G$ , we treat the Kondo effect of a single Co impurity within an effective spin-1/2 Anderson impurity model without orbital degeneracy [24], where, as shown in Chapter 1, the Kondo temperature is [4, 20]

$$k_B T_K \simeq \sqrt{\frac{\Gamma U}{2}} \exp\left\{-\frac{\pi(\epsilon + U)|\epsilon|}{2\Gamma U}\right\}. \quad (3.8)$$

This equation relates the Kondo temperature  $T_K$  to the on-site Coulomb repulsion  $U$ , the half width of the hybridized  $d$ -level  $\Gamma$  and its position  $\epsilon$ . Density functional theory (DFT) is used to map the “real” system [e.g. Co/Cu(100)] onto the spin-1/2 effective Anderson model [24].  $\epsilon$  and  $U$  are determined through the band structure of Co by estimating the  $d$ -level occupation and the exchange splitting between majority and minority  $d$ -bands. DFT calculations of Co/Cu(100) by Hofer *et al.* [109] predict a shift of the majority band towards the Fermi level when strain is exerted onto Co through a tip displacement [Fig. 3.13(a)]. The DFT calculations

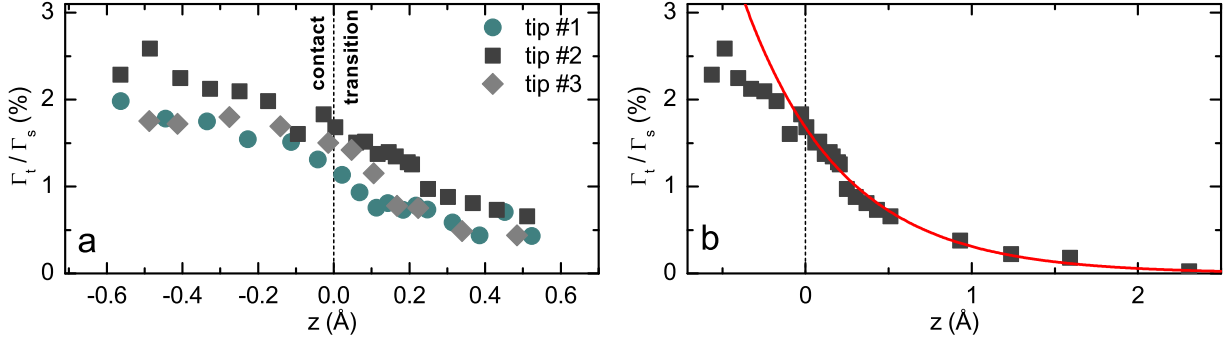


Figure 3.14: Relative coupling  $\Gamma_t/\Gamma_s$  for various tips: (a) Contact-Transition region, (b) Over a wider tip excursion (the solid line is an exponential fit to the data in the tunneling regime). The vertical dashed line is centered at  $z = 0$ . We estimate  $\Gamma = \Gamma_s = 0.3$  eV (see text), therefore  $\Gamma_t$  varies from a couple of neV in the tunneling regime up to a couple of meV in the contact regime.

by Stepanyuk *et al.* [Fig. 3.13(b)] [143, 148] predict a similar shift, but also predict a shift of the minority band towards negative energies. This shift is small compared to the one of the majority band, but sufficient to decrease the magnetic moment of the Co atom from 1.77 (tunnel) to  $1.28 \mu_B$  (contact). Since  $\Gamma$  is nearly constant (see below), we may anticipate from DFT calculations that  $\epsilon$  and  $U$  change upon tip displacement due to the forces acting between the Co atom and the tip-apex atom, and consequently increase the Kondo temperature. The changes we detect in  $T_K$ , and also in the Fano parameter  $q$ , indicate that adhesive forces set in at least  $0.5 \text{ \AA}$  prior to contact in agreement with previous studies presented in Section 3.2.

To quantify the impact of tip displacement on  $\Gamma$ , we have determined in Fig. 3.14 the relative  $s-d$  coupling of the atom to the surface ( $\Gamma_s$ ) and tip ( $\Gamma_t$ ) based on the magnitude of the differential conductance at the Fermi level. In the limit of  $T \ll T_K$  [31, 150, 151], which is fulfilled here, we have

$$dI/dV(V=0) \approx (4\Gamma_t\Gamma_s)/(\Gamma_s + \Gamma_t)^2 + (dI/dV)_{\text{el}} \quad (3.9)$$

(in units of  $2e^2/h$ ). This expression recalls the transmission probability expected for one atomic orbital (Eq. (3.6)). The first term accounts for the ASK resonance, while the second term corresponds to a background contribution and amounts to at least 95% of the total conductance [Fig. 3.10]. A majority of electrons have therefore a ballistic conductance with a transmission most likely governed by the  $4s$  state of Cu and the  $3d$  and  $4s$  states of Co. Only a minor fraction

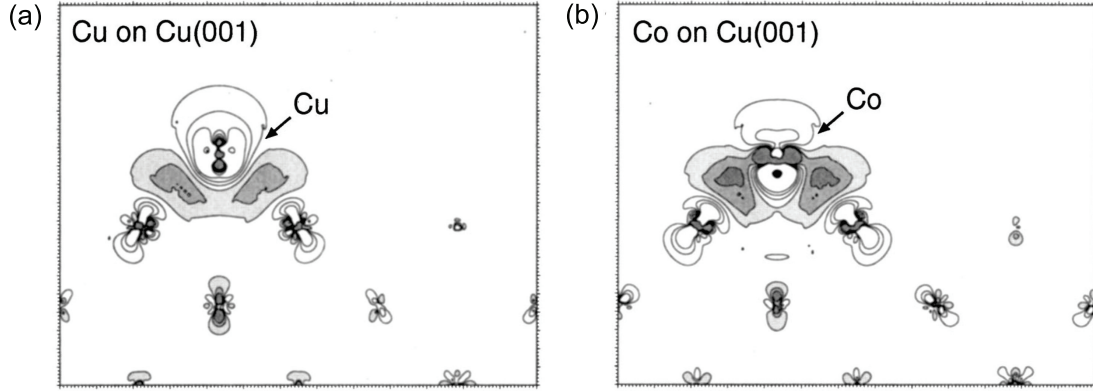


Figure 3.15: Electron density of Cu (left) and Co (right) adatoms on Cu(100). The plot is a cross section along the (100) plane. The grey regions describe the increase of electron density, while the electron depletion is marked as a contour line [149].

of the overall electrons is instead affected by Kondo correlations ( $G_c$  is in fact little dependent on bias). This is favored in our setup by the small  $\Gamma_t/\Gamma_s$  ratio of 3% or lower reported in Fig. 3.14(a). This ratio smoothly increases from tunnel to contact [Fig. 3.14(b)], but only the weaker coupling  $\Gamma_t$  changes significantly so that the overall  $\Gamma$  is practically unaffected by the tip displacement. Therefore, the total coupling is constant and  $\Gamma = \Gamma_s + \Gamma_t \simeq \Gamma_s$ . To some extent, the tip-atom coupling is expected to be weaker than the atom-surface coupling. A first argument to invoke is coordinance, the cobalt adatom having only one neighbouring atom on the tip compared to four neighbouring atoms on the surface. A second argument is charge transfer. Pentcheva *et al.* [149] performed DFT calculations for the electron density of Co adsorbed on Cu(100) [Fig. 3.15(a)] and for Cu adsorbed on Cu(100) [Fig. 3.15(b)]. They showed that in both systems the electron density is located in the interstitial regions below the Co and the Cu adatoms. If we then approximate the tip apex by the Cu/Cu(100) system, we may then conclude that there is less charge density available to form a bond in the tip apex-adatom region than in the adatom-surface region; accordingly  $\Gamma_t$  should then be weaker compared to  $\Gamma_s$ . Finally, we may also invoke a geometrical argument to justify  $\Gamma_t \ll \Gamma_s$ . Because  $d$  orbitals are spatially anisotropic, an  $s-d$  coupling is sensitive to the atom-lead geometry. In particular for Co/Cu(100), the Kondo effect is mainly carried by the  $d_{xy}$  orbital of the Co adatom [152]. The four lobes of the  $d_{xy}$  orbital being parallel to the surface, the hybridization between  $d_{xy}$  and the  $4s$  orbitals carried by the surface atoms is probably more favorable than the hybridization with the  $4s$  orbital of the tip-apex atom.

To fully link Eq. (3.8) to our experimental observations, we need first to formally express the changes in  $T_K$  with the  $d$ -band structure of Co, hence with  $z$ . We introduce the occupation of the  $d$ -level  $n$ , which in the spin-1/2 effective Anderson model can vary between 0 (empty orbital) and 2 (double occupancy). The Kondo regime corresponds to  $0.8 < n < 1.2$  [153] with approximately one unpaired electron in the  $d$  level. In the tunneling regime,  $n$  is estimated between  $n = 1.16$  [78] and  $n = 0.91$  [77] for Co on Cu(100). In the contact regime, the  $d$ -level occupation is unchanged [109] [Fig. 3.13(a)] or increases slightly due to a downward shift of the minority  $d$ -band [148] [Fig. 3.13(b)], but cannot increase to higher values than 1.2 in order to preserve the Kondo physics. Following then Újsághy *et al.* [24], we relate  $\epsilon$  and  $U$  by  $n = -\epsilon/U + 1/2$  and remark that the range of possible values for the  $\epsilon/U$  ratio is therefore strongly reduced. In the following, we suppose then that the  $\epsilon/U$  ratio is constant. The continued evolution of  $U$  in the contact regime should benefit from further study. This translates into a simplified expression for Eq. (3.8)

$$\ln(T_K/T_{K,c}) \simeq (\epsilon - \epsilon_c)/\tilde{\Gamma} = (-\beta\kappa/\tilde{\Gamma})z, \quad (3.10)$$

where  $\tilde{\Gamma} = 2\Gamma/\pi(1.5 - n)$  and  $T_{K,c}$  is the Kondo temperature at  $z = 0$ . We neglect changes in  $U$  in the prefactor of Eq. (3.8), which would yield a first order correction of  $\tilde{\Gamma}/2\epsilon_c \ll 1$  to Eq. (3.10). Equation (3.10) explicitly shows that the  $d$ -band displacement  $\epsilon$  relative to the equilibrium position at  $z = 0$  (noted  $\epsilon_c$ ) exponentially changes the Kondo temperature in the contact regime. Remarking that this band shift is driven by changes in the Co-Cu distances due to the tip displacement, we have expressed  $\epsilon(z) - \epsilon_c$  within a tight binding approximation. The transfer integral is approximated by  $-\beta\kappa z$  [131],  $\beta$  being proportional to the cobalt  $d$  bandwidth and  $\kappa$  a structure dependent decay constant; in transition metals,  $\kappa$  is related to the bulk modulus and is  $1 \text{ \AA}^{-1}$  or higher [154]. As  $\beta$  and  $\tilde{\Gamma}$  relate to properties of the Co atom, the tip dependency evidenced in Fig. 3.12(a) is carried by  $\kappa$ . On average we find a slope of  $\beta\kappa/\tilde{\Gamma} = -1.2 \pm 0.1 \text{ \AA}^{-1}$ . From the band shift  $\epsilon - \epsilon_c$  predicted by DFT in the contact regime we estimate  $\beta\kappa \approx 0.5 \text{ eV \AA}^{-1}$  [143], which, based on our findings, would then yield a reasonable  $s - d$  coupling of  $\Gamma \approx 0.3 \text{ eV}$  for a  $d$ -level occupation of  $n \approx 1$ . DFT predicts  $\beta\kappa \approx 0.2 \text{ eV \AA}^{-1}$  for Co/Cu(111) [143], therefore  $T_K$  should also be sensitive to atomic relaxations in this system.

We may now link  $T_K$  to the conductance in the contact regime. As mentioned above [see discussion based on Eq. (3.9)], the conductance is mainly governed by ballistic electrons. We then express the dependence of  $G$  on  $z$  within a linear expansion  $G/G_c = 1 + \kappa_0 z$ , where the



decay constant is  $\kappa_0 = (dG/dz)_{z=0}/G_c$ . This decay constant is extracted from  $G(z)$  (dashed lines in Fig. 3.9) and is tip-dependent. The average value for the tips employed amounts to  $\kappa_0 = 0.45 \text{ \AA}^{-1}$  so that  $\kappa_0 z \ll 1$  for the tip displacements considered here. By substituting this expression for  $G$  in Eq. (3.10) we arrive then to

$$\ln(T_K/T_{K,c}) = (\beta/\tilde{\Gamma})(\kappa/\kappa_0)(G/G_c - 1). \quad (3.11)$$

We have used Eq. (3.11) to fit the data of Fig. 3.12(b) (solid line) and find that  $(\beta/\tilde{\Gamma})(\kappa/\kappa_0) = 2.4 \pm 0.1$  for all tips employed. From the data, we extract  $\kappa_0 \approx 0.5 \text{ \AA}^{-1}$ , which is consistent with the previous estimate. Although  $\kappa$  and  $\kappa_0$  are tip dependent, the changes of  $T_K$  with  $G$  are not, which indicates that the ratio between the two decay constants must cancel out the tip dependency. More generally, our findings show that in this regime the  $d$ -band of Co/Cu(100), and therefore  $T_K$ , can be exponentially tuned through the conductance of the junction, regardless of tip structure. This follows from the highly reproducible contact geometry, and hence reproducible  $G_c$ , achieved with this experimental setup. The above relation also applies in the transition regime, but only over a finite conductance range as  $\kappa_0$  increases due to the presence of the tunneling barrier. We find in fact  $\kappa_0 = 2.15 \text{ \AA}^{-1}$  in the tunneling regime where  $G \propto \exp(-\kappa_0 z)$ , which then limits the validity of Eq. (3.11) to  $G \gtrsim 0.6$ . For a full description of the transition regime, an analytical expression of  $G(z)$  would be needed.

### 3.3.4 Heating effects

As presented in Section 1.2, temperature can induce a broadening of the Kondo resonance. Local heating effects induced by the current density flowing across the Co atom can therefore potentially impact our measurements. Heating occurs when electrons exchange energy with the single atom that bridges the electrodes and with conduction electrons forming the Kondo cloud. The heating power is typically within 10% of the electric power because of ballistic transport [91]. The heat generated at the atom is dissipated to the bulk electrodes via phonon-phonon interactions, while the heat of the electronic bath is dissipated to the lattice through electron-phonon interactions. The atom region reaches a local temperature higher than the working temperature. Based on our data, however, heating effects do not affect the Kondo effect of Co.

In thin metal films, however, the electron-phonon scattering rate, which determines the rate

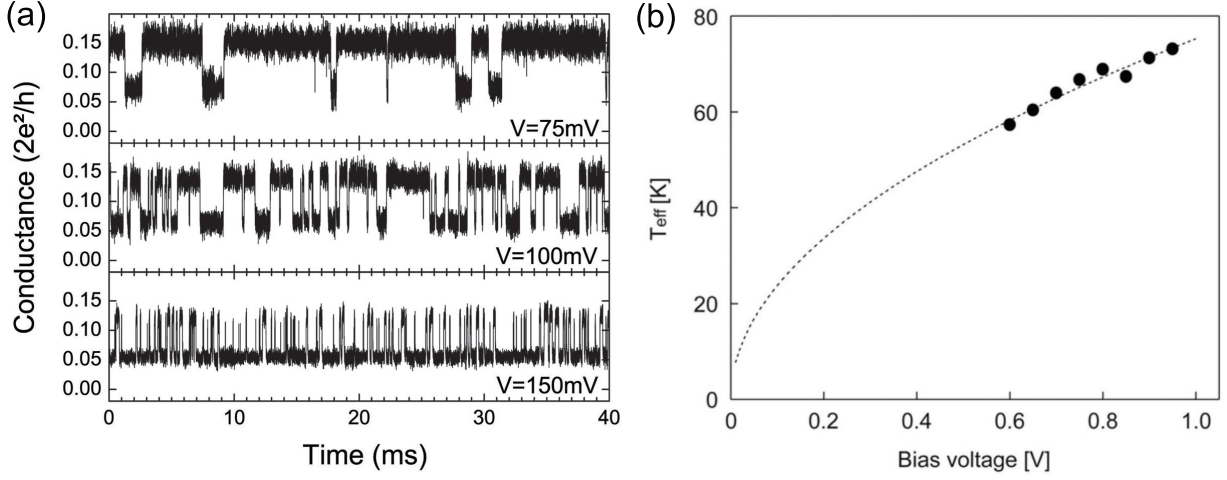


Figure 3.16: Time resolved two-level fluctuations of the conductance: (a) Bias dependence [159], (b)  $T_{\text{eff}}$  as a function of bias for an Au atomic-sized contact [160].

of heat flow out of the electron gas, can be smaller than the electron-electron scattering rate ( $1/\tau_{e-e}$ ). This results in a temperature difference between electrons (at temperature  $T_e$ ) and the lattice (at temperature  $T_l$ ) with  $T_e > T_l$  [155–157]. The question to answer in relation to the Kondo effect is then: Why is  $T_e \ll T_K$ ? A possible explanation for the absence of heating may be invoked by comparing the typical length scales involved in the Kondo screening ( $\xi_K$ ) and in the inelastic scattering. The spatial range of the Kondo effect of Co/Cu(100) is  $\xi_K = \hbar v_F / k_B T_K \simeq 40 \text{ nm}$  ( $v_F$ : Fermi velocity of copper) [18]. The electron-electron scattering length is  $\xi_{e-e} = v_F \tau_{e-e}$  and, for the biases employed,  $\xi_{e-e}$  is equivalent to at least 900 nm [158]. Since  $\xi_K \ll \xi_{e-e}$ , heating can be neglected.

Estimates of the lattice temperature also indicate that heating is negligible. The lattice temperature of an atomic contact can be evaluated by focusing on the random telegraph noise [159, 160] in the conductance of an atomic point contact [Fig. 3.16(a)]. This noise reflects the two-level fluctuations (TLF) of the conductance between tunneling and contact regimes caused by atomic vibrations from inelastic scattering of the ballistic electrons. As bias is increased, the frequency of the fluctuations increases and an effective temperature of the junction can then be extracted using an Arrhenius-like law [161, 162]. The voltage dependence of  $T_{\text{eff}}$  is expressed as [163, 164];

$$T_{\text{eff}}^4 = T^4 + \gamma^4 L^2 V^2, \quad (3.12)$$

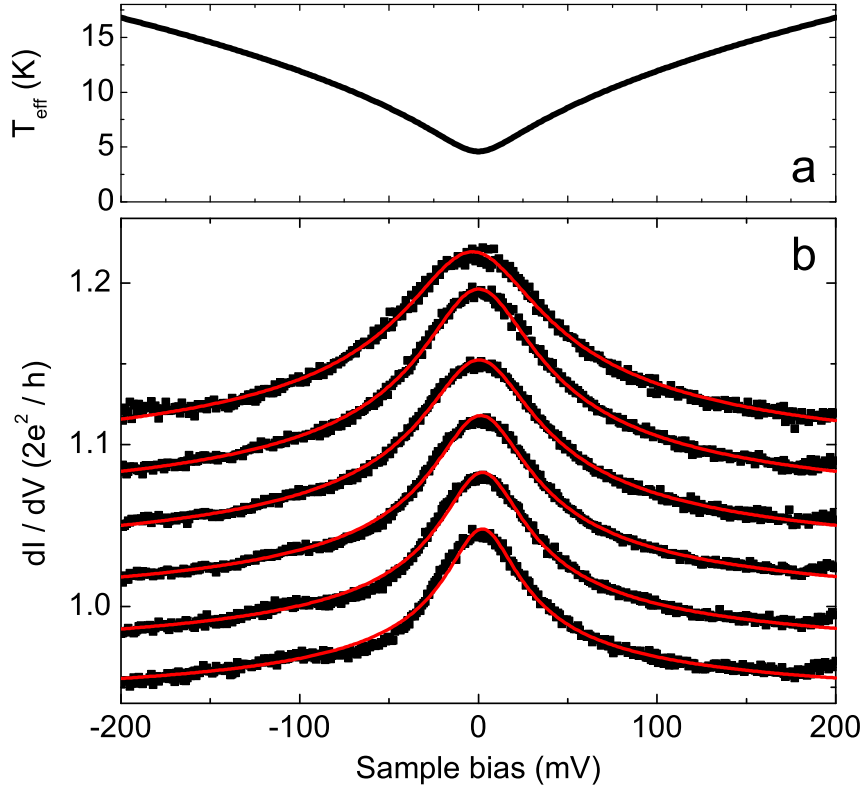


Figure 3.17: Simulation of  $T_{\text{eff}}$  and Frota fitting of the ASK resonance as a function of bias. (a)  $T_{\text{eff}}$  as a function of bias in our system. (b)  $dI/dV$  fitted by Frota functions in the contact regime.

where  $T$  is the zero-bias temperature,  $L$  is the characteristic length of the contact, and  $\gamma$  denotes the efficiency of the electron-phonon interaction to produce heat. This constant is typically  $\gamma \sim 60 \text{ K V}^{-1/2}$  for metals [164]. As shown in Fig. 3.16(b) for an atomic-sized contact,  $T_{\text{eff}}$  increases monotonically with bias [160, 165]. We have simulated in Fig. 3.17(a) the effective lattice temperature of our junction using Eq. (3.12). We assume that in the case of a single-atom contact  $L$  corresponds to an atomic lattice distance of  $2.5 \text{ \AA}$ . The temperature then varies from 18 K at the setpoint bias of  $-0.2 \text{ V}$  down to 4.6 K at zero bias, where the system recovers the reservoir temperature, and remains always well below  $T_K$ . Recent theoretical work on an aluminium nanowire also predicts similar temperatures [166].

More evidence showing the minimal impact of heating may be gathered directly from the experimental data. Firstly, the Kondo line width starts increasing in the transition regime where heating effects are negligible [159] (Fig. 3.14). Therefore the observed broadening cannot be

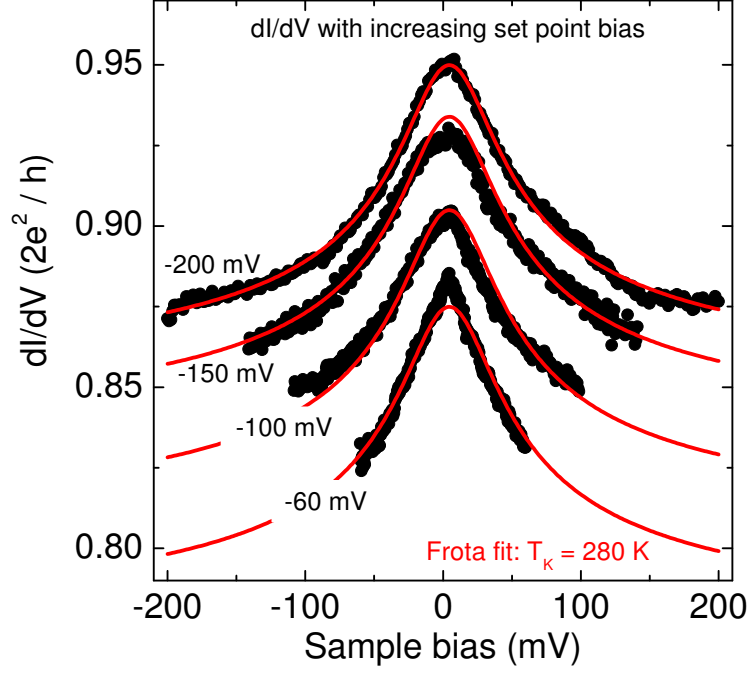


Figure 3.18:  $dI/dV$  acquired with increasing bias ranges:  $\pm 60$  mV,  $\pm 100$  mV,  $\pm 150$  mV and  $\pm 200$  mV.

explained by a heating mechanism. Secondly, if heating were significant in the contact regime, it would affect the line shape of the  $dI/dV$  spectra. Since heating is a bias-dependent effect, a bias-dependent broadening would set in during spectrum acquisition and cause the high-bias “tails” of the ASK resonance to stretch (an accurate modeling of this effect necessitates an out-of-equilibrium analysis beyond the scope of the present Thesis). To test if this is the case, we have fitted in Fig. 3.17(b) our  $dI/dV$  data with a Frota function. This fitting method is only applicable for the case where  $q \gg 1$ , *i.e.* when the ASK resonance is peak-like [167, 168]. Frota *et al.* [146, 169] proposed a phenomenological expression for the ASK resonance, which closely approximates the exact solution obtained with numerical-renormalization group theory. In particular, the Frota function correctly reproduces the logarithmic tails of the ASK resonance contrary to a Lorentzian. The Frota function  $\rho_F$  has been recently applied to successfully fit the Kondo line shape of STM measurements [147, 170] and is expressed by

$$\rho_F(\epsilon) = \text{Im} \left[ \frac{1}{i} \sqrt{\frac{i\Gamma_F}{i\Gamma_F + \epsilon - \epsilon_K}} \right], \quad (3.13)$$

where  $\Gamma_F = 1.455k_B T_K$ . The definition of the Kondo temperature differs from the one used for a Lorentzian function; the two are related by  $0.54T_K(\text{Lorentzian}) = T_K(\text{Frota})$  [147]. Figure 3.17(b) shows that our experimental data can be successfully fitted with a Frota function in the contact regime. The ASK resonance detected therefore exhibits a line shape very close to predictions. Moreover, as shown in Fig. 3.18, the  $dI/dV$  spectra remain similar despite the increasing set point voltages used. Based on these results, we therefore neglect heating effects.

## Summary and conclusions

The conductance of a quantum point contact is characterized by the lateral confinement of the electron wave vector in the conductor. As a result the conductance is expressed by multiple values of the quantum of conductance  $G_0 = 2e^2/h$ . The contact conductance of a monovalent atom deviates from its ideal value due to asymmetries in the atom coupling to the leads, or due to the presence of defects or excitations such as phonons in the leads. We have seen that STM can be successfully employed to build stable and reproducible single-atom contacts. To do so, we progressively bring the STM tip into contact on an adsorbed atom by monitoring the changes in conductance with tip displacement.

When the tip is moved into contact on a target atom, the environment of the atom experiences atomic relaxations, which also affect the transport properties. Atomic relaxations can in principle be monitored by the combined measurement of conductance and force using an STM/AFM microscope. Alternatively, we may use STS and monitor indirectly the changes in the electronic structure induced by atomic relaxations. In the present Chapter, we have in particular focused on the evolution of the ASK resonance of a single Kondo impurity in the presence of tip-induced atomic relaxations. A low-temperature STM was employed to build a junction comprising a Co atom bridging a copper-coated tip and a Cu(100) surface. An ASK resonance was evidenced in the differential conductance and its width was shown to vary exponentially with the ballistic conductance regardless of the tip employed. Using a theoretical description based on the Anderson model, we showed that the Kondo effect and the total conductance are related through the atomic relaxations affecting the environment of the Co atom. Our findings should apply to other single-impurity Kondo systems and, more generally, open the interesting perspective of controlling, and even activating the magnetism of single impurities on surfaces through the conductance.

## CHAPTER 4

# Spin-polarized currents at a single Kondo impurity

In this chapter, we deal with the Kondo effect in the presence of a spin-polarized current, which is a fundamental topic totally unexplored to date. To do so, we exploit some basic concepts developed in spintronics and pioneered over the last two decades. Spintronics exploits two spin populations—up and down—to implement logic memory in devices. Of importance to spintronics, and to us, is the possibility to inject a spin-polarized current into a nonmagnetic metal, since if the metal hosts a single Kondo impurity, it is then possible to study the interplay between the Kondo effect and the spin-polarized current. The Chapter is therefore organized as follows. The basic concepts of spintronics are introduced in Section 4.1. Emphasis will be put on the giant magnetoresistance (GMR) where the spin injection between a ferromagnet and nonmagnet produces a net magnetization near their interface. This magnetization is directly responsible for the changes we observe in the Kondo resonance. These are presented in the second part of this Chapter. By contacting a single Co atom on a Cu(100) surface with copper-coated ferromagnetic tips or pristine ferromagnetic tips (Section 4.2), we show that the Kondo resonance may split apart or not depending on the competition between spin-polarization, ferromagnetism and atomic relaxations. We will then conclude this Chapter by comparing our results with two related studies.

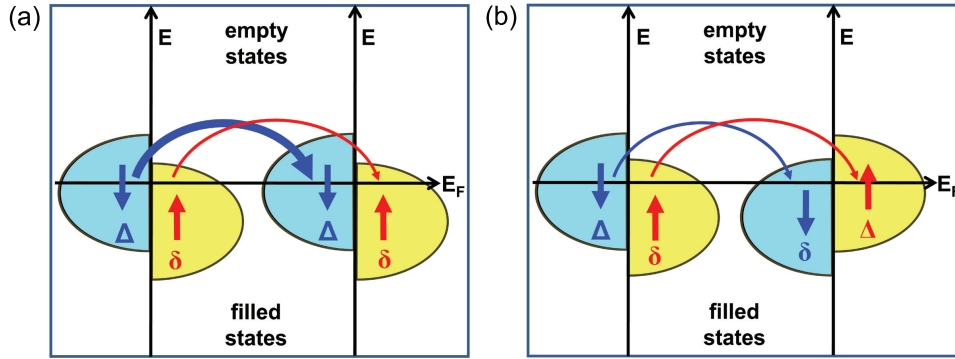


Figure 4.1: Schematics of the density of states (DOS) and spin-polarized tunneling in a (a) parallel and (b) antiparallel alignment of the magnetizations for two FMs. The conductance in the parallel configuration is higher than in the antiparallel case at the Fermi level.  $\Delta$  and  $\delta$  are the DOS at  $E_F$  for minority and majority spin populations, respectively. The tunneling process preserves the spin orientation of the electrons.

## 4.1 Spintronics: a brief overview

Spin-transport electronics, also known as spintronics, is an emerging technology that exploits the spin of an electron in solid-state devices in addition to its electronic charge. In particular, two spin channels—up and down—are used to convey or store binary information. Control over the two channels is achieved by external parameters such as an applied magnetic field and can be used to write or read in data storage devices. Spin-polarized tunneling was pioneered by R. Meservey and P. M. Tedrow in the 1970s [171, 172]. A spin-polarized current was shown to tunnel from a ferromagnet (FM) through an insulating barrier by using an aluminium superconductor as a spin detector. An important step forward was done by Jullière in 1975, who reported the first conductance measurements on a ferromagnet/insulator/ferromagnet tunnel junction [173]. Jullière proposed that the tunneling current depends on the orientation of the magnetization of the two ferromagnets, parallel ( $\uparrow\uparrow$ ) or antiparallel ( $\uparrow\downarrow$ ). According to the model suggested by Jullière, the conductance for parallel and antiparallel alignment is proportional to the product of the density of states (DOS) of the two ferromagnets which is given as  $G_{\uparrow\uparrow} \propto (\Delta_{\uparrow})^2 + (\delta_{\downarrow})^2$  and  $G_{\uparrow\downarrow} \propto \Delta_{\uparrow}\delta_{\downarrow} + \delta_{\downarrow}\Delta_{\uparrow}$  (Fig. 4.1).  $\Delta_{\uparrow(\downarrow)}$  and  $\delta_{\uparrow(\downarrow)}$  are the amplitude of the DOS of each ferromagnet at a given energy for spin-up and down electrons, respectively. Assuming that  $\Delta \gg \delta$ , then  $G_{\uparrow\uparrow} \propto \Delta^2$  and  $G_{\uparrow\downarrow} \propto 2\Delta\delta$ . In this simple example, the  $\uparrow\uparrow$  configuration produces the highest conductance of the junction, while  $\uparrow\downarrow$  produces a

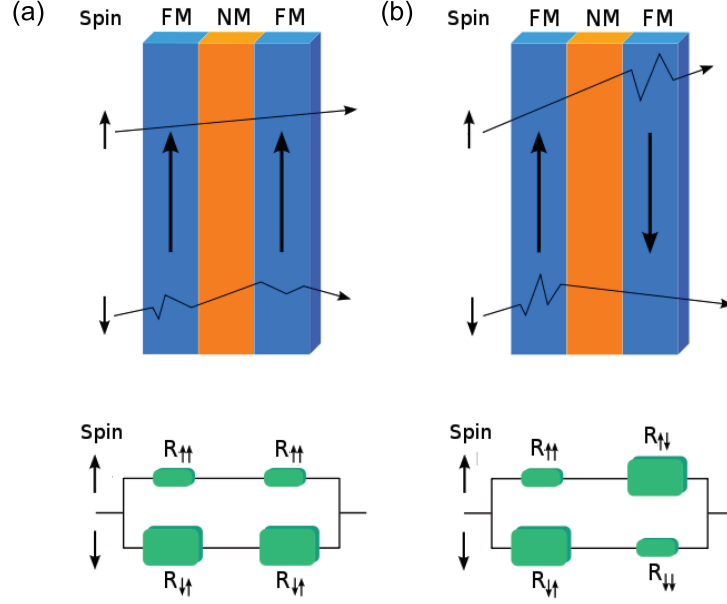


Figure 4.2: Schematics of spin-polarized transport for (a) parallel, and (b) antiparallel alignments of FMs in a GMR device. A spin-polarized current flows from one FM through NM to another FM. In the case of parallel alignment of the FMs, the resistance is lower than in the antiparallel configuration.

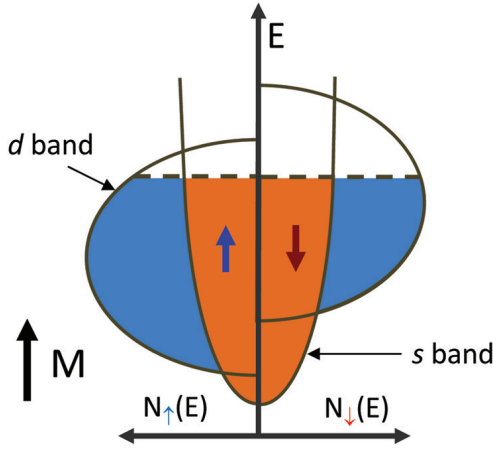
lower conductance. The change of the conductance in the junction can then be expressed as a magnetoresistance (MR)

$$\text{MR} = \frac{G_{\uparrow\uparrow} - G_{\uparrow\downarrow}}{G_{\uparrow\downarrow}} = \frac{\Delta R}{R} = \frac{R_{\uparrow\downarrow} - R_{\uparrow\uparrow}}{R_{\uparrow\uparrow}}, \quad (4.1)$$

where  $R_{\uparrow\downarrow}$  is the resistance in the antiparallel configuration and  $R_{\uparrow\uparrow}$  denotes the resistance in the parallel orientation. The practical realization of a tunneling magnetoresistance (TMR) was carried out with two FMs insulated by a tunnel barrier of  $\text{Al}_2\text{O}_3$  in 1995 [174, 175].

A giant magnetoresistance (GMR) [176, 177] was discovered in “spin valve” devices comprising two ferromagnets (FMs) separated by a nonmagnetic metallic layer—a nonmagnet (NM) [178]. The working principle of such a GMR device is sketched in Fig. 4.2. It is very similar to a TMR device, however the electrons now flow ballistically from one ferromagnet to the other, instead of tunneling. The nonmagnet spacer is only a few nanometers thick in order to ensure ballistic transport, but sufficient to magnetically decouple the ferromagnets. An electron passing through this multilayer device will be scattered more if the ferromagnets have





Material	Point	Base	$P_{n=0}(\%)$	$P_{n=1}(\%)$
Co	Nb	Co foil	$35 \pm 3$	$42 \pm 2$
Fe	Ta	Fe film	$40 \pm 2$	$45 \pm 2$
	Fe	Ta foil		$46 \pm 2$
	Nb	Fe film		$42 \pm 2$
Ni	Nb	Ni foil	$23 \pm 3$	$46.5 \pm 1$
	Nb	Ni film		$43 \pm 2$
	Ta	Ni film		$44 \pm 4$

Figure 4.3:  $s$  and  $d$  band structures in a ferromagnet. The  $d$  band is split due to the exchange interaction. The table presents polarizations at  $E_F$  for several FMs [179,180].  $P_{n=0}$  corresponds to the tunneling polarization, while  $P_{n=1}$  is the current polarization.

opposite magnetizations. The device has then a higher resistance than in the parallel case and the collected current differs for the two configurations. A hard disk storing binary information can use the difference in resistance between parallel and antiparallel alignments as a method of storing 0s and 1s.

When a current flows from a ferromagnet to a nonmagnet, the current is spin-polarized due to the spin-asymmetry of the DOS in the ferromagnet (Fig. 4.3). The DOS of the ferromagnet at the Fermi-level has  $s$  and  $d$  character. The  $d$  band is more localized than the  $s$  band, accordingly  $s$  electrons have a higher mobility compared to  $d$  electrons. The current is therefore carried by  $s$  electrons. However, the  $d$  electrons are split by the exchange interaction and, as a result, present a very different DOS for spin-up and down channels into which the  $s$  electrons may be scattered (Fig. 4.3). The down  $s$  channel (minority spins) suffers the most scattering and hence has lower mobility than the up-channel (majority spins). The up- $s$  channel consequently carries most of the current. Thus in a system with  $s$ - and  $d$ -like character at  $E_F$ , the tendency is for the current to be carried by the majority spins where majority is taken to mean the electrons with the lowest DOS at  $E_F$ . With this convention, when the current is carried by majority spins, the current polarization is positive. The current polarization is defined as

$$P = \frac{I_{\uparrow} - I_{\downarrow}}{I_{\uparrow} + I_{\downarrow}}, \quad (4.2)$$

where  $I_{\uparrow}$  is the current for majority electrons and  $I_{\downarrow}$  for minority electrons. Note that the magnetization of the FM layer is defined as ( $k_B T \ll E_F$ )

$$M \propto \mu_B \int_{-\infty}^0 (N_{\uparrow} - N_{\downarrow}) dE, \quad (4.3)$$

where  $N_{\uparrow(\downarrow)}$  is the DOS of spin-majority (minority) electrons, respectively. In the case of Ni and Co ferromagnets,  $M$  and  $P$  have same sign. This situation is depicted in Fig. 4.3. The expression of the polarization changes depending on the measurement performed or length scale examined [181]. The general expression of the polarization is [182]

$$P_n = \frac{N_{\uparrow} v_{\uparrow}^n - N_{\downarrow} v_{\downarrow}^n}{N_{\uparrow} v_{\uparrow}^n + N_{\downarrow} v_{\downarrow}^n} \quad (4.4)$$

where  $v_{\uparrow}^n$  and  $v_{\downarrow}^n$  denote the spin-dependent Fermi velocity. The  $n = 0$  case corresponds to photoemission measurements or to tunneling across amorphous barriers, while  $n = 1$  corresponds to ballistic transport and  $n = 2$  to diffusive conduction. The tunneling polarization is expressed as  $P_{n=0} = (N_{\uparrow} - N_{\downarrow}) / (N_{\uparrow} + N_{\downarrow})$  assuming that the tunneling barrier is not spin-selective. The current polarization is  $P_{n=1} = P = (I_{\uparrow} - I_{\downarrow}) / (I_{\uparrow} + I_{\downarrow})$ . The two polarizations  $P_{n=0}$  and  $P_{n=1}$  of ferromagnets are not identical as shown in the table in Fig. 4.3.

A fundamental aspect of any GMR device is the presence of a spin-polarized current in the nonmagnet. Far away from the FM/NM interface, the current depends on the conductivity and therefore on the DOS of each layer. In the nonmagnet, the current is unpolarized, so there are an equal number of majority and minority spins flowing. In the ferromagnet on the other hand, the current is spin dependent as mentioned above. When electrons flow from the ferromagnet to the nonmagnet [Fig. 4.4(a)], there are more majority electrons than minority electrons flowing towards the interface, but equal numbers of majority and minority electrons flowing away from it in the nonmagnet. This imbalance leads to an accumulation of majority spins near the interface and causes the chemical potential ( $\mu$ ) of spin up and down electrons to split:  $\Delta\mu = \mu_{\uparrow} - \mu_{\downarrow}$  [Fig. 4.4(b)]. This effect is known as spin accumulation. These majority spins diffuse away from the interface into both materials. The diffusion of majority spins away from the interface and back into the ferromagnet gives a negative correction to the spin-polarized current flowing in the ferromagnet [Fig. 4.4(c)]. The diffusion of majority spins into the NM means instead that the current in the nonmagnet is spin-polarized. The system reaches a steady state because of spin-flip scattering. As more nonequilibrium spins accumulate, they relax faster

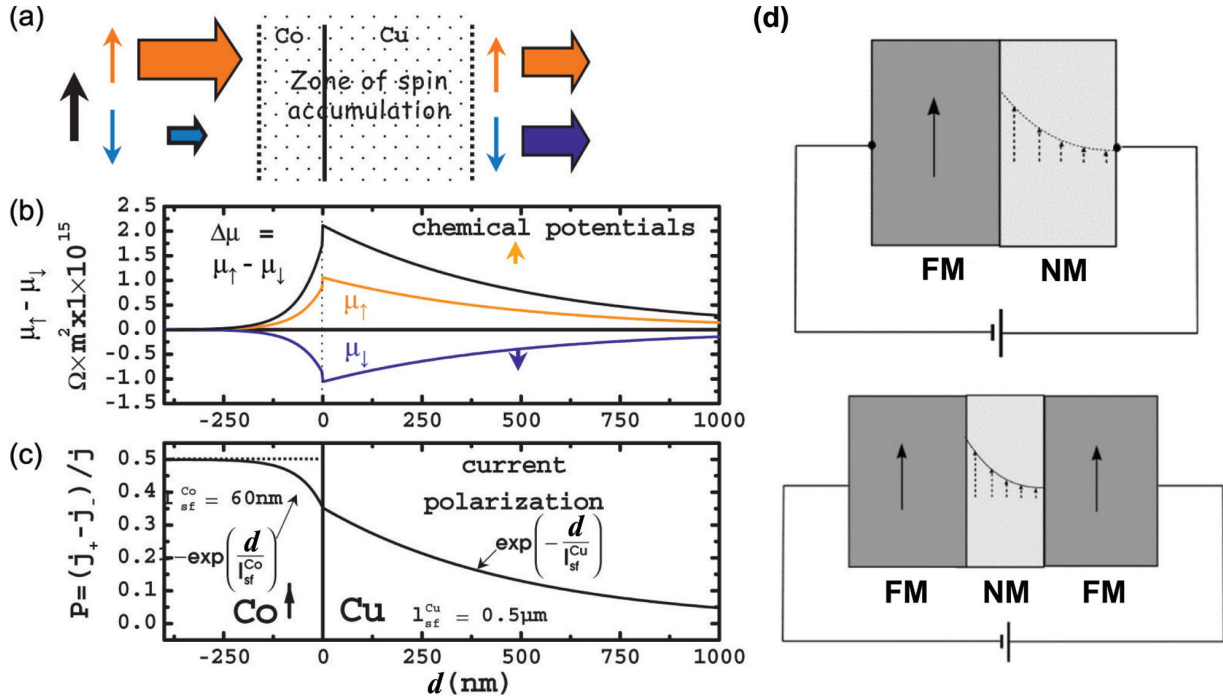


Figure 4.4: Spin junction at the interface of a cobalt FM and a copper NM. (a) Schematic view of spin injection from a cobalt FM to a copper NM. Spin-up electrons are injected more than spin-down electrons. (b) The chemical potential of spin up and down electrons and splitting of the chemical potential  $\Delta\mu$  as a function of  $d$ . (c) Spin polarization at the interface [183]. (d) Schematics of spin injection at FM/NM interface and spin-valve device [184].

toward equilibrium due to the increased population, and eventually, spin-flip scattering cancels the net arrival of excess spins. The length scale over which the spin-polarized current recovers its bulk values is the spin diffusion length ( $l_{sf}$ ). The spin diffusion length is  $l_{sf} = (v_F \tau_{sf} l / 3)^{1/2}$ , where  $l$  is the mean free path and  $\tau_{sf}$  denotes the spin relaxation time. Typical values of  $l_{sf}$  are therefore greater than  $l$ :  $\geq 500$  nm for Cu,  $\geq 40$  nm for Co,  $8.5 \pm 1.5$  nm for Fe and  $21 \pm 2$  nm for Ni at 4.2 K [185].

The existence of accumulated spins near the interface means that a magnetization ( $M_s$ ) builds up in the nonmagnet. This magnetization decays exponentially away from the interface [Fig. 4.4(d)] and can be expressed by the Valet-Fert model as [186]

$$M_s = (P j l_{sf} \mu_B / e D) \exp(-d / l_{sf}) \quad (4.5)$$

where  $P$  is the spin polarization of the current,  $j$  is the current density,  $\mu_B$  the Bohr magneton,  $D$

the diffusion constant of the nonmagnet, and  $d$  the distance away from the interface. In practice, however, detecting spin accumulation is not straightforward. One possibility, for example, would be to measure the splitting of the chemical potential  $\Delta\mu$ . This splitting is related to  $M_s$  by [186]

$$\Delta\mu = \mu_{\uparrow} - \mu_{\downarrow} = M_s(eD\rho/\mu_B) = Pj\rho l_{sf}\exp(-d/l_{sf}) , \quad (4.6)$$

where  $\rho$  is the resistivity of the nonmagnet. For typical values of the current density ( $j = 10^3$  A cm<sup>-2</sup>),  $\Delta\mu$  amounts to only  $2 \cdot 10^{-4}$  meV at a Co/Cu interface. In the following section, we show instead that this is feasible if the detection is performed in a quantum point contact, since then the current densities are  $j \sim 10^8$  A cm<sup>-2</sup>.

## 4.2 Spin injection and detection with a Kondo impurity

In this section, we show how it is possible to detect and control the spin-polarized current flowing across a single atom. Using an STM, we build well calibrated junctions [60] comprising a single cobalt atom bridging two electrodes—tip and surface—of different geometry and chemical nature. We use the Kondo effect [109, 143, 187] as a spectroscopic probe of the magnetic environment surrounding the cobalt atom. As we presented in Section 1.3, exchange interactions tend in fact to freeze the spin of a Kondo impurity and ultimately lead to the splitting of its ASK resonance. The resonance splitting detected in conductance measurements has been exploited to study direct [90, 188–190] and indirect [10, 191] interactions between spins, or the exchange interaction with ferromagnetic leads [9]. We extend here this work to an atomicscale spintronic device engineered by using a copper-coated magnetic tip in contact with a single cobalt atom. Spins are injected at the interface between the magnetic tip and the copper-coating layers, while a quantum-point contact between the copper tip apex and the cobalt atom is used as a spin detector. The current densities flowing across the cobalt atom are sufficiently high to split the ASK resonance apart, demonstrating the presence of a spin-polarized current in the nonmagnetic copper spacer. Spin injection is shown to be altered by the chemistry of the tip apex, as pristine magnetic tips tend instead to weaken the spin injection.

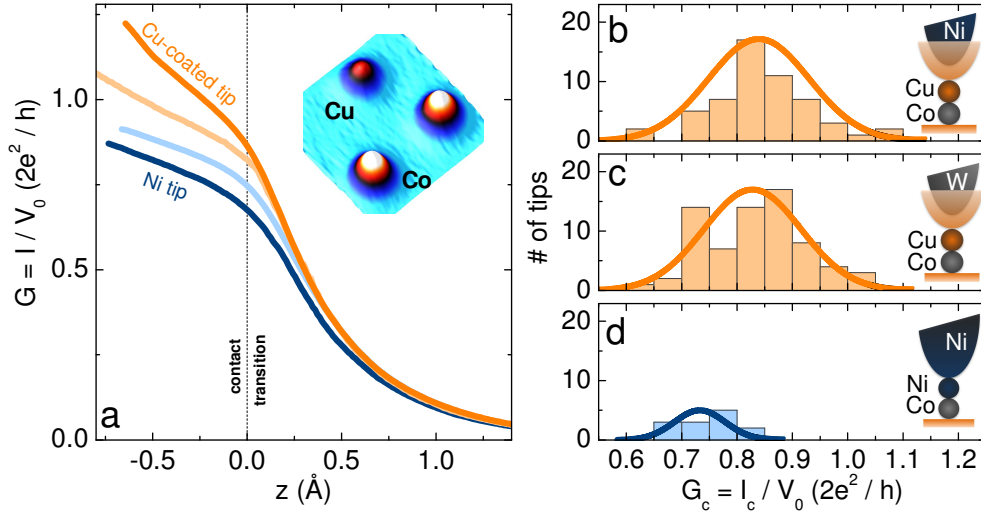


Figure 4.5: Engineering a single-atom junction. (a) Typical conductance versus tip displacement for two copper-coated tips (solid orange lines) and for two Ni tips (solid blue lines) above a Co atom on Cu(100) ( $V_0 = -200$  mV). The vertical dashed line is positioned at  $z = 0$  where  $G = G_c$ . Inset: Constant-current image of Co and Cu atoms on Cu(100) ( $13 \times 13 \text{ Å}^2$ ,  $-200$  mV,  $1$  nA). Apparent heights are  $1.1$  and  $0.8 \text{ Å}$  for Co and Cu, respectively. (b)-(d) Histogram of  $G_c = I_c/V_0$  for NiCu tips (b), for WCu tips (c), and for Ni tips (d). The distinct values of  $G_c$  for the copper-coated and pristine nickel tips allow easily distinguishing Ni tips contaminated by surface material. Each junction is sketched to the right of the histograms.

#### 4.2.1 Junction fabrication

For this study, we use magnetic tips covered by non-magnetic copper. Etched W tips, as well as bulk Ni and Fe tips, were first cleaned by sputter/anneal cycles. The copper-coating of the tips was then performed by depositing 10 atomic layers (AL) of copper through the sublimation of a high-purity Cu wire. Alternatively, copper-coating was carried out *in vacuo* by indenting the tips a multiple number of times into the copper substrate (the depth of each indentation amounted to  $3 \text{ nm}$  or more). As both coating methods produced similar data, we therefore estimate the thickness of the copper layers on the tip to be  $\geq 10 \text{ AL}$ . Tip status was monitored through STM images and through controlled tip-atom contacts in order to select tips terminated by a single atom [60]. The differential conductance spectra,  $dI/dV(V)$ , where  $V$  is the sample bias measured with respect to the tip and  $I$  is the current, were acquired via lock-in detection with a bias modulation of amplitude  $2 \text{ mV rms}$ , or less, and a frequency close to  $700 \text{ Hz}$ .

Figure 4.5(a) presents the evolution of the conductance ( $G = I/V_0$ ) for two given Cu-coated

tips and for two pristine Ni tips as they are vertically displaced towards the center of a Co atom on Cu(100) [inset of Fig. 4.5(a)]. The curves are acquired at a fixed bias of  $V_0 = -200$  mV. A tip displacement (noted  $z$  hereafter) of  $z = 0$  defines the boundary between the transition regime ( $z > 0$ ) and the contact regime ( $z < 0$ ). As we showed in Section 3.2, in the transition regime, electrons tunnel between the tip and the substrate, but the conductance is influenced by atomicscale relaxations [60,126]; the structural relaxations vanish once  $z \gtrsim 1$  Å. The  $z = 0$  boundary is deduced through the contact conductance ( $G_c = I_c/V_0$ ), which is determined following a geometrical approach described elsewhere (see Fig. 3.5 in Chapter 3) [118]. The contact formation is stabilized by charge transfer between Co and the surface [60], and is highly reproducible and reversible. The average contact conductance is  $\langle G_c \rangle_{\text{NiCu}} = 0.83 \pm 0.09$  (in units of  $2e^2/h$ ) for Ni tips coated with copper (noted NiCu), while it is  $\langle G_c \rangle_{\text{WCu}} = 0.84 \pm 0.09$  for W tips coated with copper (noted WCu). The similar values obtained for  $G_c$  indicate that the conductance is governed by the bottleneck structure comprising the Co atom and the Cu apex atom of the tip, and is only weakly influenced by the bulk material of the tip. The contact of a Ni tip with Co produced a lower value of  $\langle G_c \rangle_{\text{Ni}} = 0.73 \pm 0.05$  compared to copper-coated tips, in agreement with previous work [118]. The weaker conductance observed for Ni tips compared to Cu-coated tips is assigned to a smearing of the minority  $d$  states of Co due to the additional hybridization with the minority  $d$  states of Ni [192]. As we show after, this also weakens the spin-polarization of the current flowing across the Co atom.

#### 4.2.2 Spin- versus structure-related properties

Figure 4.6 presents the evolution of the Kondo effect of Co/Cu(100) with nonmagnetic tips (WCu) and bulk magnetic tips terminated with copper (NiCu and FeCu tips). The  $dI/dV$  spectra are acquired by freezing the geometry of the junction at selected conductances. These conductances correspond in Fig. 4.6 to the value of the  $dI/dV$  at  $-170$  mV. A tip excursion of about  $5.5$  Å was covered by varying the conductance over several orders of magnitude. In Fig. 4.6, we focus on the transition-to-contact boundary where substantial spectral changes are evidenced. With WCu tips [Fig. 4.6(a)], an ASK resonance is detected at the Fermi level [187]. The peak line shape is correctly reproduced by a Frota function [solid orange lines in Fig. 4.6(a)] [146], which closely reproduces the exact solution obtained with numerical-renormalization group theory [147]. Along with Co, we also monitored the  $dI/dV$  spectra on non-magnetic Cu and Au atoms, where as expected, no ASK resonance is present [see orange

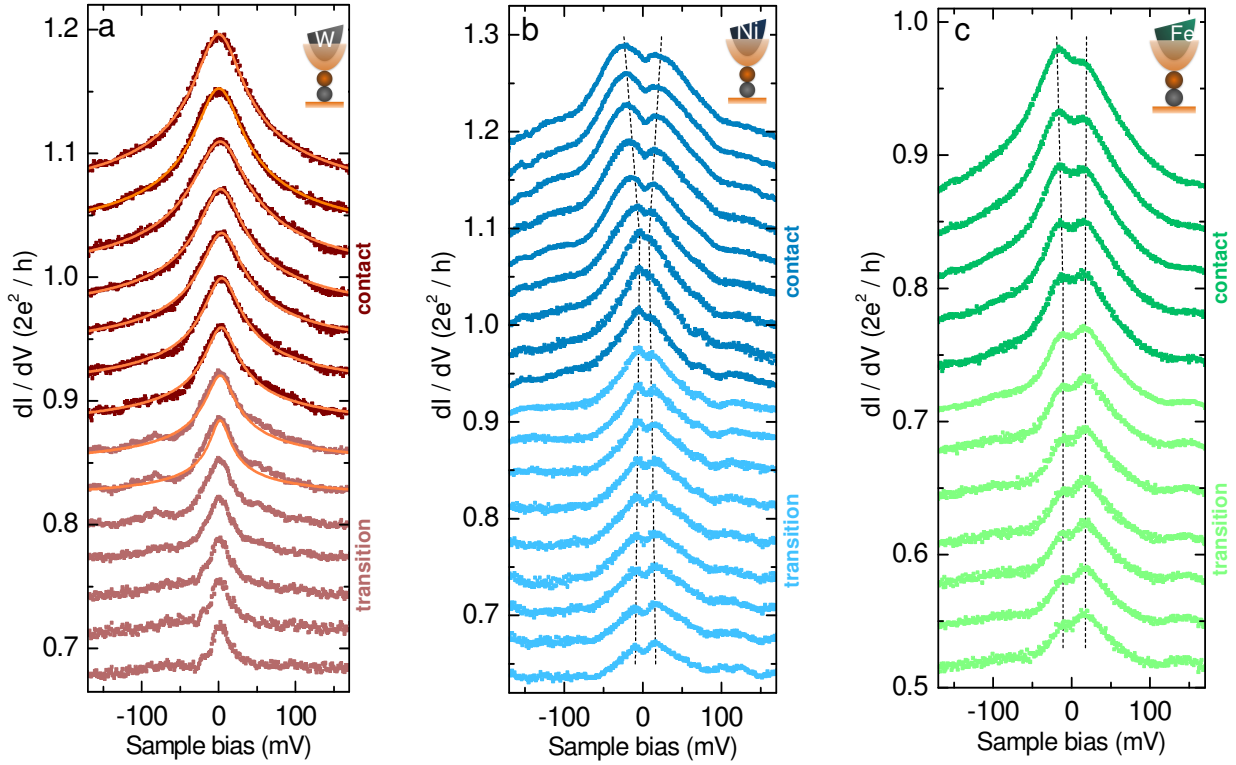


Figure 4.6: ASK resonance in the presence of a spin-polarized current. (a)  $dI/dV$  spectra from transition (solid light-red lines) to contact (solid red lines). The solid orange lines correspond to fits using a Frota function [147]. All data are fully reversible with tip displacement. (b) and (c) present  $dI/dV$  spectra from transition to contact acquired with a NiCu and a FeCu tip, respectively, showing how the ASK resonance splits apart in two resonances (the dashed lines are positioned at the maxima of the two resonances).

line in Fig. 4.10(b)]. The line width increases exponentially as a function of the current reflecting changes in the Kondo temperature ( $T_K$ ). These changes are due to tip-induced atomic relaxations affecting the environment of the Co atom (Section 3.3). The Kondo temperature varies typically from 100 K in the transition regime up to 300 K or more in the contact regime [see Fig. 4.7(a)]. We use here Wilson's definition of  $T_K$  [147, 193], therefore the values of  $T_K$  are lower by a factor 2 compared to Section 3.3. The spectral signature of the ASK resonance changes dramatically when NiCu [Fig. 4.6(b)] or FeCu [Fig. 4.6(c)] tips are brought into contact with the Co atom. Instead of a single peak, two peaks are detected in the  $dI/dV$ , approximately symmetric about the Fermi level and with similar amplitudes and widths. Several FeCu and NiCu tips were employed [see Fig. 4.7(b) for another FeCu tip] and, despite a strong tip

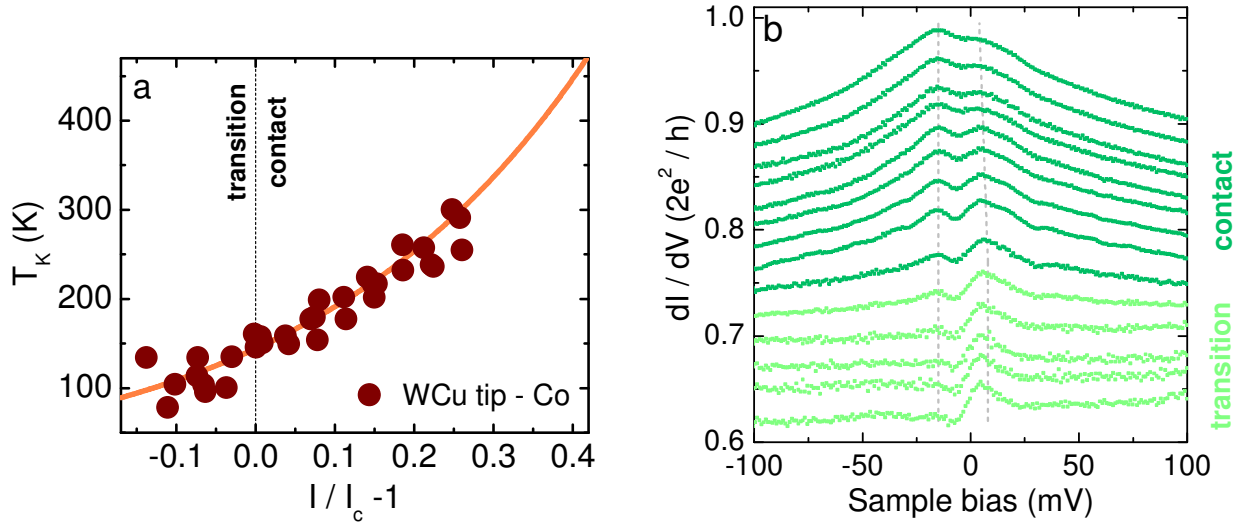


Figure 4.7:  $T_K$  versus current for a WCu tip and evolution of  $dI/dV$  spectra for a FeCu tip. (a)  $T_K$  versus conductance for various WCu tips. The Kondo temperature is extracted from the Frota fits [147]. The vertical dashed line is positioned at  $G = G_c$ . The solid orange line corresponds to an exponential fit [187]. (b) ASK resonance from transition to contact obtained with a FeCu tip.

dependency, all showed a similar trend [Fig. 4.8(a)]. The ASK resonance starts splitting apart in the transition regime at  $G \geq 0.25$ , which corresponds to  $z \leq 0.5$  Å. For an overwhelming majority of tips, the peak separation  $\Delta$  increases with conductance, reaching values comprised between 20 and 40 mV at the highest tip excursions explored ( $z = -0.7$  Å).

As we discuss in Section 4.2.3, the RKKY interaction is not responsible for the splitting observed. Our findings rather indicate the existence of a spin-polarized current at the Co site. As we showed in Section 4.1, when a current is injected from a ferromagnet into a non-magnetic metal, it brings with it a net injection of spin angular momentum [194–196]. A magnetization  $M_s$  builds up in the metal as result of a balance among spin injection, spin accumulation and spin relaxation. Assuming that the current has a polarization, a magnetization  $M_s$  and therefore an effective magnetic field,  $H_s \propto PI \exp(-d/l_{sf})$ , is generated at a distance  $d$  away from the interface [197]—this distance corresponds here to the thickness of the copper spacer. Since at low temperature the spin diffusion length is  $l_{sf} = 500$  nm  $\gg d$  for copper [185], we propose that the ASK resonance is spin split by the effective field  $H_s \propto PI$  [see Fig. 4.12(a)]. The resonance splitting  $\Delta$  is therefore governed by the magnitude of the current flowing across Co and its polarization  $P$  near  $E_F$ . As we showed in Section 3.3, about 90% of the current is ballistic in



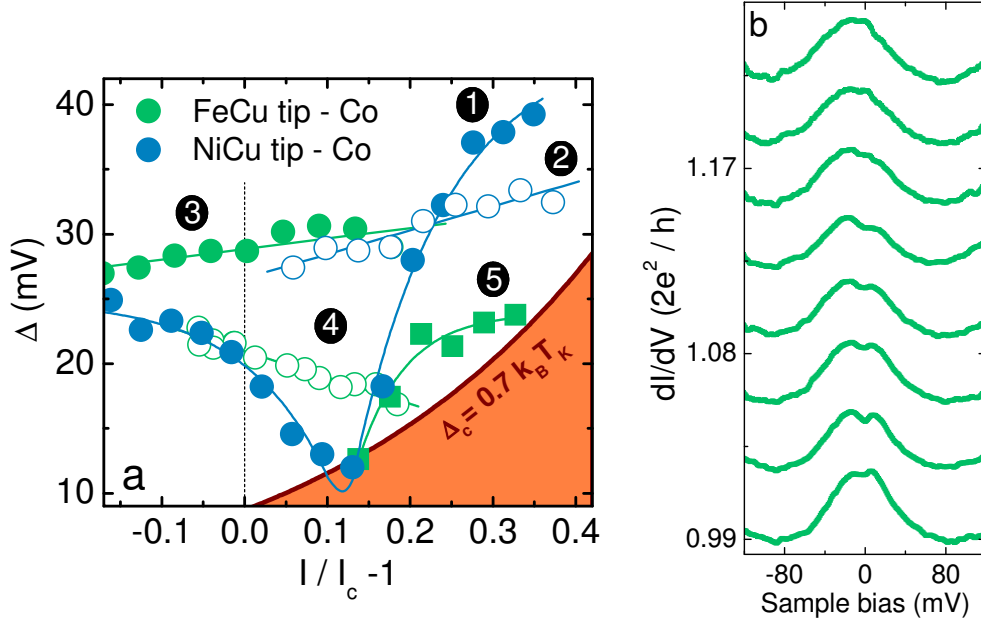


Figure 4.8: (a)  $\Delta$  versus current for various FeCu and NiCu tips [tips are labeled from 1 to 5; tip 2 corresponds to the spectra of Fig. 4.6(b)]. The lines are a guide to the eye. The solid red line corresponds to the exponential fit of panel Fig. 4.7(a) scaled by a factor 0.7 (see text). Below this line, the resonance splitting is lost. (b) Restoration of the ASK resonance by atomic relaxations [spectra correspond to the curve labeled 5 in (a)].

the contact regime, while only 10% of the electrons possess Kondo correlations, so that the spin-polarized current is mainly carried by ballistic electrons. The spin-polarized current is also responsible for the splitting observed in the transition regime and is only fully suppressed once the tunneling barrier is restored at  $z = 0.5 \text{ \AA}$  [126], in remarkable agreement with our findings. Figure 4.7(b) presents a close up view of the lineshape in the transition-to-contact region. The Kondo resonance is detected as stepped-like Fano line in the tunneling regime as for a WCu tip (Section 3.3). However, once in the transition regime, a gradual change towards a peak-like ASK resonance occurs. While the Fano parameter increases from  $q \sim 1$  to  $q \gg 1$ , a second peak appears below  $E_F$ , which eventually matches the other peak in width and amplitude.

An obvious consequence is that  $\Delta$  is expected to increase with current, which agrees with the trend observed in Fig. 4.8(a). The scattering of the experimental data in Fig. 4.8(a) also indicates that tip-dependent effects impact the evolution of  $\Delta$  with current. A first effect is related to structural details of the tips employed. These affect the amount of current flowing across Co at given tip excursions as revealed by the curves in Fig. 4.5(a) or by the histogram

in Fig. 4.5(b). Secondly, we expect  $P$  to be tip-dependent due to the lack of control on the roughness of the ferromagnet/copper interface. No discernible difference was observed for copper-coated Ni and Fe tips, suggesting similar polarizations for the two as found in superconducting point contacts with Fe and Ni films (Table in Fig. 4.3). Finally, it is essential to keep in mind that  $T_K$  also increases with current due to atomic relaxations affecting the environment of Co [Fig. 4.7(a)]. While  $\Delta$  splits the ASK resonance apart, a higher  $T_K$  tends instead to restore the Kondo line. The competition between the two effects can result in a weakening of the splitting [tip 2 in Fig. 4.8(a)], or even its suppression well within the contact regime [tips 4 and 5 in Fig. 4.8(a)]. Figure 4.8(b) shows a set of spectra where a suppression of the splitting of the Kondo resonance occurs. Based on the gathered data, we estimate that the resonance is approximately observable whenever  $\Delta > \Delta_c = 0.7k_B T_K$ , which is close to the critical value needed to observe a Zeeman splitting of the ASK resonance [34]. The critical value  $\Delta_c$  is plotted versus the conductance in Fig. 4.8(a) [for this purpose we use the fit to  $T_K$  of Fig. 4.7(a) scaled by a factor 0.7].

### 4.2.3 Role of the RKKY interaction

A splitting of the ASK resonance is known to occur when a Kondo impurity is exchanged coupled with a magnetic electrode [9, 37, 39]. Since the Co atom is separated from the magnetic backbone of the tip by at least 10 ALs of copper (or equivalently 2 nm of copper), the exchange coupling must necessarily be indirect. The splittings are too large to be associated to a Zeeman splitting  $2g\mu_B H$  [34] produced by the stray fields of Ni or Fe ( $\approx 1$  Tesla), since the splitting observed amounts to an effective magnetic field of  $H \approx 130$  Tesla exerted on the Kondo impurity. Another possibility to consider is an RKKY interaction mediated by the electrons of the copper spacer (Section 1.3.3). Recently, Meier *et al.* [198] showed by using an STM that the RKKY interaction between a Co atom and a Co cluster is at most 1 meV [Fig. 4.9(a)]. Given the thickness of the Cu-spacer on the tip, the RKKY is negligible and probably lower than expectations due to the roughness of the tip-copper interface [200, 201]. The RKKY interaction is therefore at least one order of magnitude weaker than the splitting observed in our experiments. Studies conducted with multilayer systems also showed that no RKKY interaction could be evidenced with a Kondo impurity when the non-magnetic spacer is thicker than 3 ALs [202, 203]. Finally, *ab initio* calculations confirm that the RKKY interaction is indeed weak for distances higher than 1 nm [199] [Fig. 4.9(b)]. We stress, moreover, that the *ab initio*

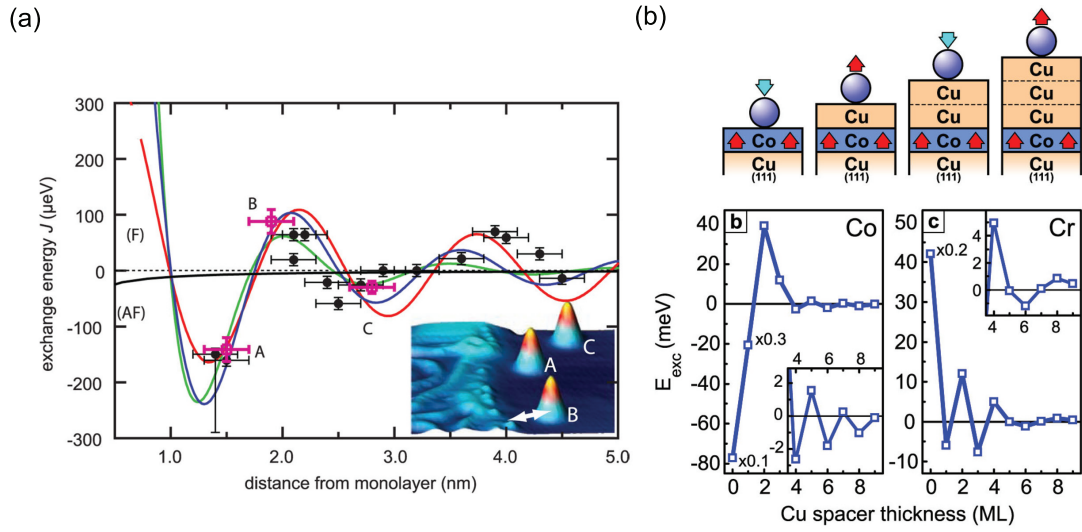


Figure 4.9: (a) Experimental estimate of the RKKY interaction (dots) between a Co atom and a Co cluster (see image in the inset). The solid black line is the calculated dipole interaction, while the simulated RKKY interactions are plotted in red (1D), blue (2D), and green (3D) [198]. (b) Up: Schematics of the system used for the *ab initio* calculations. An adatom is coupled to a Co layer through a Cu spacer with different thickness. Bottom: Exchange coupling energy for a Co (left) and a Cr (right) adatom as a function of the spacer thickness [199].

calculations predict changes up to two orders of magnitude for the RKKY interaction between an atom and a magnetic surface, these changes occurring mainly when the non-magnetic spacer is 1 to 4 ALs thick. If the RKKY interaction were involved in the splitting we observe, our results would depend crucially on the thickness of the copper spacer at variance with observations. We can therefore neglect the RKKY interaction in our setup.

#### 4.2.4 Ferromagnetism and chemistry

In order to probe the influence of pristine magnetic tips on the Kondo effect of Co, we performed controlled contacts with a Ni tip. Typical  $dI/dV$  spectra for Co are presented in Fig. 4.10(a). Surprisingly, a unique ASK resonance is now detected in the transition and contact regimes. A multitude of tips were employed [Fig. 4.10(b)], and none exhibited the splitting previously reported for copper-coated Ni tips. In Fig. 4.10(c), we have estimated the width of the ASK resonance for a collection of Ni tips using Frota fits as in Fig. 4.6(a). The Kondo temperature extracted from these resonances is very similar to the one reported for the WCu tip [the solid

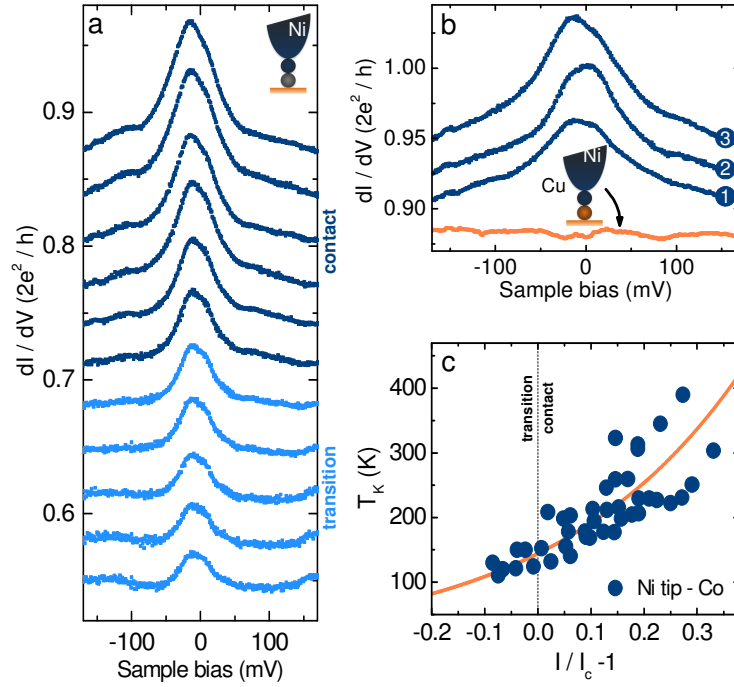


Figure 4.10: ASK resonance in the presence of a spin-polarized current and ferromagnetism. (a)  $dI/dV$  spectra from transition (solid light-blue lines) to contact (solid blue lines) acquired with a pristine Ni tip. (b)  $dI/dV$  spectra acquired in the contact regime with three different tips labeled 1, 2, 3 in the panel. For clarity, spectra 2 and 3 are displaced vertically by 0.02 and 0.04, respectively. The bottom spectrum was acquired with the tip into contact with a non-magnetic Cu atom. (c)  $T_K$  versus conductance for various Ni tips. The Kondo temperature is extracted from Frota fits [147]. The solid orange line is the fit of Fig. 4.7(a).

line in Fig. 4.10(c) corresponds to the exponential fit of Fig. 4.6(a)]. Since  $T_K$  is sensitive to relaxations effects, we conclude that a Ni tip and a copper-coated tip produce similar tip-induced atomic relaxations in the contact regime. As shown in Fig. 4.11, estimates of the  $\Gamma_t/\Gamma_s$  ratio (see Section 3.3) confirm also that the coupling of Co to the surface continues to dominate the Kondo effect. The absence of splitting in the case of a pristine Ni tip therefore cannot be justified by invoking relaxations effects alone.

A more plausible scenario is to recall that compared to the copper-coated Ni tip, there is now along with a spin-polarized current flowing across Co also a direct ferromagnetic coupling between the Co atom and the Ni tip. The Co atom interacts with the single Ni atom at the tip apex [Fig. 4.5(d)]. We assume the Co-Ni  $d-d$  exchange coupling to be roughly 10 meV since the coupling among neighboring Co-Co and Ni-Ni atoms amounts to  $J_{d-d} = 15$  and 3 meV,

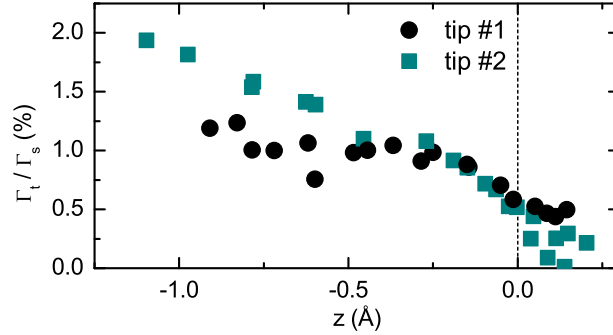


Figure 4.11: Relative coupling  $\Gamma_t/\Gamma_s$  for pristine Ni tips in the contact-transition region.

respectively [12, 204]. The exchange field produced by the Ni apex atom on Co is then at most of order  $H_{FM} = J_{d-d}\langle S_{Ni} \rangle / (g\mu_B) \simeq 50$  Tesla, where  $\langle S_{Ni} \rangle = 0.6$ . This exchange field produces a Zeeman splitting of the ASK resonance, which we estimate to be  $2g\mu_B H_{FM} \simeq 10$  meV [34]. Since density functional theory calculations show that the current is still carried by majority carriers in a Ni-Co-Cu quantum point contact [192], the exchange field  $H_{FM}$  and the field  $H_s$  sum up to split the ASK resonance apart. The detection of a unique ASK resonance indicates however that the two effective fields are not sufficient to overcome the restoring effect of  $T_K$ , in other words  $\Delta < \Delta_c$ . The only plausible explanation is that the exchange field  $H_s$  in the present setup decreases at least by a factor 2. Since the currents flowing across Co differ at most by 10% between copper-coated and Ni tips [Fig. 4.5(b)], the decreased value of  $H_s$  originates from a dramatic change in the current polarization produced by the Ni-Co contact. This dropped polarization is supported by recent calculations by Tao *et al.* predicting a polarization of only 2.5% in a Ni-Co/Cu contact [192]. Spin injection is therefore less efficient with a pristine ferromagnetic Ni tip compared to a copper-coated ferromagnetic tip.

#### 4.2.5 Model calculation: Equation of motion

Our findings indicate that the point contact between a magnetic tip and a Kondo impurity produces an intricate Kondo effect involving the competition between spin-polarized current, ferromagnetism and atomic relaxation. To model the impact of the spin-polarized current on the Kondo effect, we recall that  $M_s \propto \mu_\uparrow - \mu_\downarrow$  [see Eq. (4.6)] [197, 205], where  $\mu_\uparrow$  and  $\mu_\downarrow$  are the chemical potentials of majority and minority spins. This then implies that  $H_s \propto Q$ , where  $Q = (\mu_\uparrow - \mu_\downarrow) / (\mu_\uparrow + \mu_\downarrow)$ . Spin accumulation leads to nonequilibrium states for majority

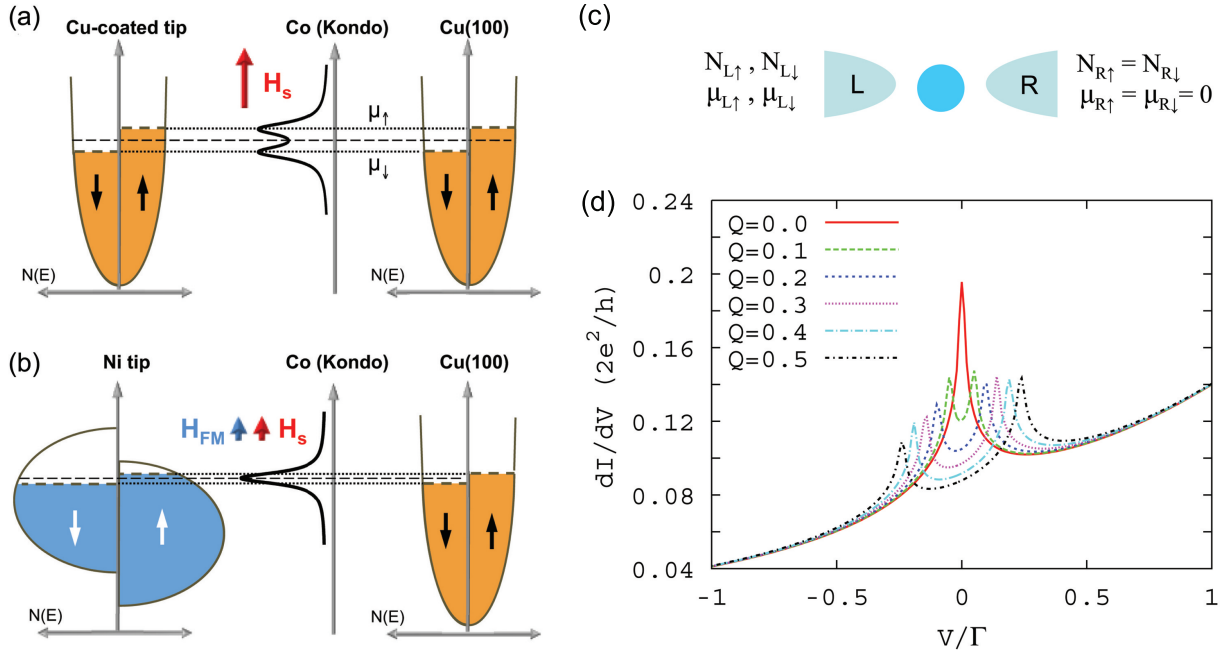


Figure 4.12: Panels (a) and (b) illustrate, respectively, how the ASK resonance changes with a magnetic tip coated with copper and with a pristine Ni tip. (c) The schematic diagram of the model system used for the EOM calculation. The atom is located between the two leads. The left lead carries the spin-dependent chemical potential and a polarization. (d) Theoretical simulation of the differential conductance in the presence of a splitted chemical potential without the ferromagnetic  $d$ - $d$  coupling.

and minority spins where  $\mu_{\uparrow}$  and  $\mu_{\downarrow}$  are different at the ferromagnet and nonmagnet interface. Figure 4.12(a) illustrates schematically the splitting of the chemical potential when the magnetic tip is covered by copper. We suppose that the splitting of chemical potential is same for both sides of the junction, *i. e.* it is the same in the copper to the left of the cobalt atom, and in the copper to the right of the cobalt atom. The splitting of the chemical potential generates an effective magnetic field,  $H_s$ , which lifts the degeneracy of spin up and down states and splits the Kondo resonance apart. The system with a pristine magnetic tip is illustrated in Fig. 4.12(b). In this case, a direct  $d$ - $d$  coupling is also present, which produces an exchange field  $H_{FM}$  on the Co atom. Depending on the magnetic material used,  $H_{FM}$  and  $H_s$  can be either parallel or antiparallel. In the antiparallel case, the resonance splitting produced by the ferromagnetic coupling opposes the one originating from the spin-polarized current. Here, in view of the Ni tip used,  $H_s$  and  $H_{FM}$  are instead parallel and sum up to split the ASK resonance. However

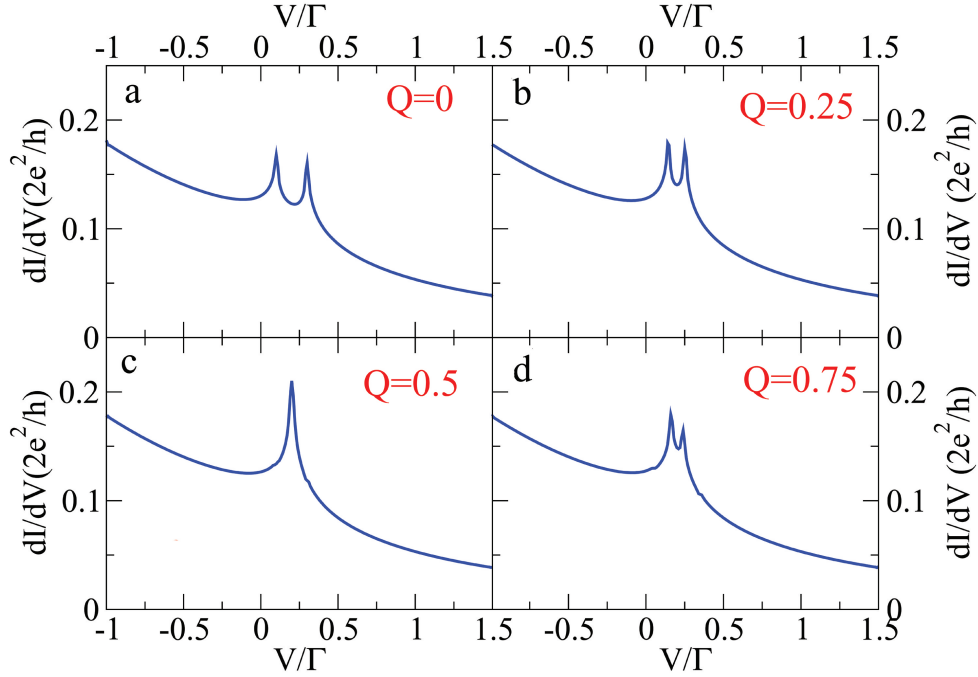


Figure 4.13: Theoretical simulation of the differential conductance in the presence of a spin-polarized current and ferromagnetism ( $\Gamma = 0.5$ ,  $T = T_K$  and  $U \rightarrow \infty$ ). In panel (c),  $H_s$  and  $H_{FM}$  are antiparallel, therefore compensate each other and restore the Kondo resonance.

this is still not sufficient to overcome the restoring effect carried by the atomic relaxations, and therefore no splitting of the resonance is detected. Note that  $H_s$  is weaker in Fig. 4.12(b) compared to Fig. 4.12(a) due to the Ni-Co hybridization.

In order to validate this scenario, **Jong Soo Lim**, **Rosa López**<sup>1</sup> and **Pascal Simon**<sup>2</sup> carried out calculations based on the equation of motion technique (EOM) [9]. The objective was to show that when a splitting of the chemical potential and a ferromagnetic interaction are introduced in the Kondo Hamiltonian (see Section 1.1), they lead to a splitting of the Kondo resonance. Such a theoretical analysis has not yet been performed to date. The model system is illustrated in Fig. 4.12(c), where we assume that the spin-dependent chemical potential and the ferromagnetism are carried by the left lead without loss in generality. We first present the calculated differential conductance without the ferromagnetic  $d$ - $d$  interaction [Fig. 4.12(d)]. The calculation clearly shows that as a nonequilibrium spin-population builds up, and leads to

<sup>1</sup>Departament de Física, Universitat de les Illes Balears, at Palma de Mallorca, Spain

<sup>2</sup>Laboratoire de Physique des Solides, CNRS, Université Paris Sud at Orsay, France

a splitting of the Kondo resonance. The higher  $Q$ , *i. e.* the higher the current flows across Co, the stronger the splitting gets. Note that  $T_K$  is kept constant, therefore atomic relaxations are neglected here. When a ferromagnetic coupling is introduced, an effective exchange field  $H_{\text{FM}}$  is exerted on the Co atom [Fig. 4.13(a)]. This produces the splitting of the Kondo resonance even if  $Q = 0$ . This situation resembles the one described by Pasupathy *et al.* (Section 1.3.2). When  $Q \neq 0$ , and if  $H_{\text{FM}}$  and  $H_s$  are parallel, the resonance splitting increases (not shown). However, when the two are antiparallel, as  $Q$  increases, the Kondo splitting is first seen to decrease [Fig. 4.13(b)], and eventually is fully restored when  $|H_s| = |H_{\text{FM}}|$  [Fig. 4.13(c)]. If  $Q$  is further increased, the Kondo resonance splits apart again.

### 4.3 Comparison with previous studies

#### “The Kondo effect in the presence of ferromagnetism” by Pasupathy *et al.*

As we showed in Section 1.3.2, Pasupathy *et al.* demonstrated that the Kondo resonance is split in the presence of ferromagnetism [9]. They used a  $\text{C}_{60}$  molecule as a quantum dot bridging two ferromagnetic leads [Fig. 4.14(a)]. With Au leads, the Kondo resonance is detected as a single peak, while with Ni leads the Kondo resonance is split when the magnetizations of the leads are parallel [Fig. 4.14(b)]. In their system, the electrons are tunneling since the  $\text{C}_{60}$  and the leads are weakly coupled. This can be easily recognized by the background contribution to the differential conductance which is much lower than  $1 G_0$ . The coupling with the leads is ensured by  $s$  electrons; these are also spin-polarized by the  $d$  electrons of the leads, and produce the exchange field, which splits the resonance apart.

To some extent, the experiment of Pasupathy *et al.* closely resembles to our experiment carried out with ferromagnetic tips covered by a nonmagnetic material. The only difference resides in the transport properties, which in our case, are governed by ballistic electrons compared to tunneling electrons in their case. While their results have established that the Kondo effect can be exploited in relation to a TMR device, our findings demonstrate that the Kondo effect may also be explored with a GMR device. Actually, if a second magnetic lead could be implemented in our setup [dashed line in Fig. 4.14(a)], as in the setup of Pasupathy *et al.*, it could be possible to control the Kondo effect through the relative orientations of the magnetizations of the two ferromagnetic leads.



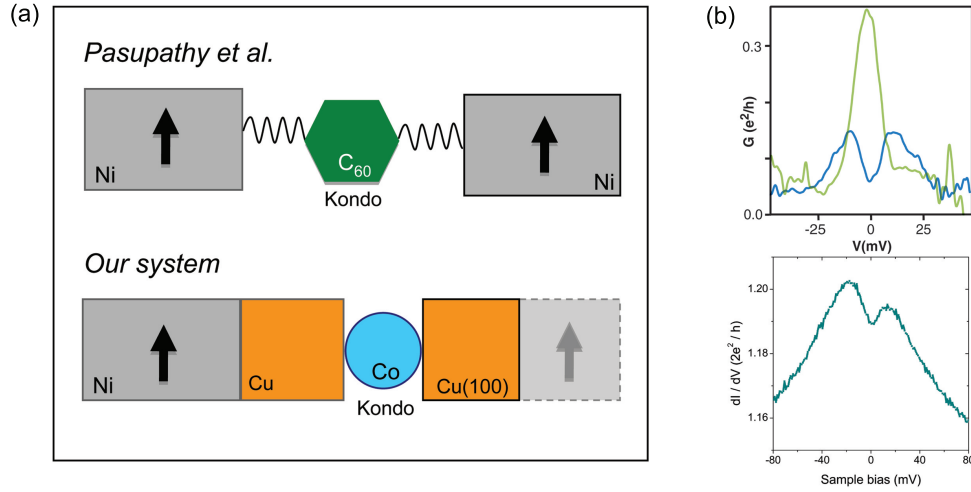


Figure 4.14: Comparison with the experiment by Pasupathy *et al.* (a) Schematics of the junction used by Pasupathy *et al.* and our junction (b) Top: The differential conductance in a Ni-C<sub>60</sub>-Ni device with magnetizations in parallel (blue line) and anti-parallel (green) alignment [9]. Bottom:  $dI/dV$  spectrum acquired with a Ni tip covered by copper in contact with a Co atom on Cu(100).

### “The Kondo effect in ferromagnetic atomic contacts” by Calvo *et al.*

Calvo *et al.* focused on the Kondo effect in nanoscale constrictions of ferromagnetic wires [12]. While in bulk the conduction takes place through  $s$  and  $p$  electrons, whereas the magnetic moments are carried by  $d$ -electrons, this general picture may change in nanoscale constrictions. Electrons can in fact then experience interactions that differ from those in the bulk. In fact, despite their strong bulk ferromagnetism, Calvo *et al.* showed that these constrictions exhibit a Kondo Physics. The conductance was recorded during the stretching of iron, nickel and cobalt magnetic wires and the monatomic contact was assigned to conductances ranging from  $1G_0$  to  $2G_0$  [Fig. 4.15(a)] [206]. The evolution of the conductance was recorded for thousands of traces due to the lack of microscopic control over the constriction [Fig. 4.15(a)], which is instead achievable in our setup. A Kondo resonance is unexpectedly observed in the  $dI/dV$  spectra as shown in Fig. 4.15(b). More than 80 % of the  $dI/dV$  curves showed peaks or dips around zero bias such as those in Fig. 4.15(b). The resonances observed were interpreted as single ASK resonances and assigned to exhibit a characteristic Fano-like lineshape. A statistical survey of the resonance width in the different materials indicates that the Kondo temperature is  $T_K = 90, 120, 280$  K for iron, cobalt and nickel, respectively.

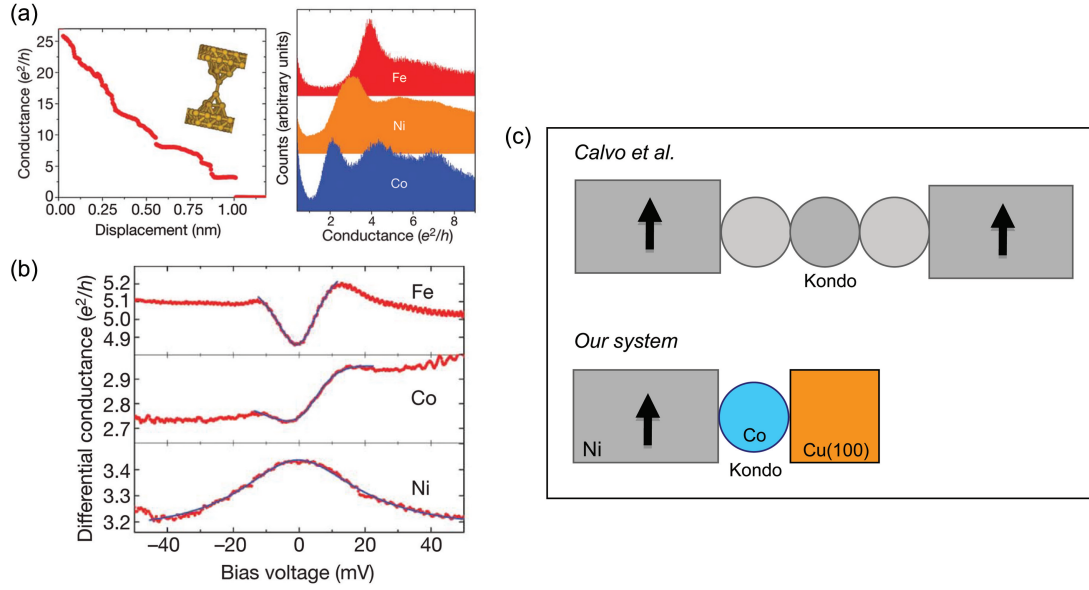


Figure 4.15: Comparison with the experiment by Calvo *et al.* (a) Left: The conductance recorded while stretching a nickel wire at 4.2 K. The inset shows the schematics of the monatomic contact. Right: Conductance histograms for iron, nickel and cobalt from thousands of traces. The first peak is the conductance of the monatomic contact. (b) Differential conductance spectra of the ferromagnetic constrictions [12]. (c) Schematics of our junction and the one used by Calvo *et al.*

To justify the presence of a Kondo effect in these constrictions, Calvo *et al.* invokes three important points. First, a local magnetic moment forms at the contact atom due to the reduced coordination [Fig. 4.15(c)]. Second, the intra-atomic coupling is enhanced due to the reduced symmetry of the contact, thus reinforcing the antiferromagnetic  $sp-d$  hybridization responsible for the Kondo effect. Third, the direct  $d-d$  ferromagnetic coupling with neighboring atoms is weakened due to the reduced coordination. Thus the magnetic moment of the contact is dominated by the antiferromagnetic coupling with the  $s-p$  itinerant electrons resulting in the Kondo effect.

In view of our results, however, we believe that the interpretation given by Calvo *et al.* for their  $dI/dV$  spectra is not completely correct. Their findings of a Kondo effect in ferromagnetic nanoconstrictions is beyond any doubt, but the interpretation in terms of a single ASK resonance is problematic. Firstly, these constrictions host a spin-polarized current, and this current is likely to split apart the Kondo resonance. Secondly, even if direct  $d-d$  interactions among neighboring atoms are negligible compared to the  $sp-d$  interaction involved in the Kondo effect

( $J_{d-d} \ll J_{sp-d}$ ), the exchange field produced by  $J_{d-d}$  is still sufficient to yield a splitting of the Kondo resonance. The coupling  $J_{d-d}$  is in fact 19, 15 and 3 meV for iron, cobalt and nickel, and exchange fields  $H_{FM} = J_{d-d} \langle S \rangle / g\mu_B$  of order 526, 260 and 16 Tesla are to be expected, respectively, where  $\langle S_{Fe} \rangle = 3.2$ ,  $\langle S_{Co} \rangle = 2.1$ ,  $\langle S_{Ni} \rangle = 0.6$  [207]. We therefore propose to interpret the finding of Calvo *et al.* in terms of a Kondo resonance split apart by a spin-polarized current and/or a ferromagnetic exchange field carried by neighboring magnetic atoms (ferromagnetic electrodes) flanking the constriction. With this in mind, the  $dI/dV$  curves of the iron and cobalt constrictions in Fig. 4.15(b) should be viewed as an ASK resonance split apart by 20 meV. We then also expect the observed Kondo resonance to depend on the relative orientation of the magnetizations of the two electrodes.

## Summary and conclusions

Injecting and controlling a spin-polarized current by electrical means is central to the giant magnetoresistance, and more generally to spintronics. A spintronic device typically consists in creating nonequilibrium spin populations with the highest injection efficiency possible in one part of the device, and in detecting these populations in another part of it. In its most simple version, this is achievable by using two ferromagnets separated by a nonmagnetic region [195]. With the device dimensions nowadays approaching nanometer scale, it is becoming urgent to address this fundamental problem at the smallest possible length scales. The ability to build well calibrated junctions with a single atom bridging two electrodes of different geometry and chemical nature represents an opportunity for examining spin transport at the smallest possible length scales.

In this regard, here, we demonstrated the injection and detection of a spin-polarized current at a single-atom contact by exploiting the Kondo effect. In particular, magnetic tips covered with copper and pristine magnetic tips were brought into contact with a Co atom on Cu(100). When the spin-polarized current is injected from the magnetic tip into the copper surface, the spin dependent current splits the chemical potential of copper and induces a splitting of the Kondo resonance of Co. The resonance splitting depends on the current amplitude and polarization. When a pure magnetic tip is used instead, two changes occur with respect to the coated copper tips. Firstly, a direct  $d-d$  coupling is present between the magnetic atom at the tip apex and the Co atom on the surface. The direct interaction produces an exchange field

which contributes to the splitting of the Kondo resonance. Secondly, the hybridization between the Co atom and the tip apex changes; this in turn modifies the current polarization and hence the resonance splitting due to the chemical potential. By modeling the system, through the EOM technique, we confirmed our findings. Moreover, calculations predict that under some specific circumstances, direct ferromagnetic coupling and splitting of the chemical potential can compensate and therefore restore the Kondo resonance. This setup therefore constitutes a benchmark for investigating the interplay between Kondo correlations and itinerant-electron ferromagnetism, and can be easily extended to molecular complexes presenting a Kondo effect.



## CHAPTER 5

# Kondo effect in a molecular junction

A possible way to carry out the downscaling of electronic devices is through the manipulation of a single molecule or molecular complex as these could constitute the active components within a hybrid metal-molecule architecture. This approach, also known as molecular electronics, has been growing promisingly driven by the advancement in fundamental aspects as well as in applications. At this scale, however, new and fundamental problems arise due to sizable quantum effects. The emerging picture of electron transport through a molecular junction is in fact different from what is observed for typical conductors. Two-terminal devices, where a single molecule bridges two metal electrodes, have evidenced for example how electron transport is sensitive to the chemical nature of a molecule and its intrinsic ability to conduct current. There is also a growing awareness that electron transport suffers from poor injection efficiency at the molecule-metal contact due to a lack of control over its structural details. An increased understanding and atomicscale optimization of these factors could open up the exciting prospect of engineering the desired electric response into a molecule.

In a conventional experimental setup, the atomic structure of a molecular junction is inferred indirectly from the conductance data, and uncertainties related to the details of the molecule-electrode contacts still remain. STM can strongly minimize these uncertainties. In this Chapter we show how a stable and reproducible two-terminal device can be engineered by picking up a  $C_{60}$  molecule on the tip and then contacting an adsorbate on the surface. This approach is different compared to previous studies of this kind where a target  $C_{60}$  molecule is instead contacted by a metallic STM tip [110,112,113,116,208,209]. In an attempt to merge molecular electronics and Kondo physics, we show in this Chapter how the Kondo resonance evidenced in

Chapter 3 is modified when the Co atom is contacted by a  $C_{60}$ -terminated tip. The outline of this Chapter is as follows. In Section 5.1, we introduce the  $C_{60}$  molecule which we chose for this study and briefly describe the adsorption of  $C_{60}$  on a metal surface. In section 5.2, we present STS carried out with a  $C_{60}$ -terminated tip above a Cu(111) surface. We exemplify through this study the interest of using such a tip for exploring molecular electronics: we show how to engineer a well controlled negative differential conductance (NDC) by tunneling electrons between the  $C_{60}$  tip and the Shockley surface states of Cu(111). Afterwards, in Section 5.3, we present an ongoing work proving the impact of a  $C_{60}$ -tip onto the Kondo effect of a Co atom on Cu(100).

## 5.1 The $C_{60}$ terminated tip

$C_{60}$  is a spherical symmetric rigid molecule so-called buckminsterfullerene which consists of 60 carbon atoms. The  $C_{60}$  molecule comprises 12 pentagonal and 20 hexagonal carbon rings in a icosahedron symmetry—pentagons do not share any edge. The van der Waals diameter of a  $C_{60}$  molecule is about 1.1 nm and the nucleus to nucleus diameter is about 0.71 nm [210]. The average bond length is close to 1.4 Å. The bond between pentagon-hexagon rings has a different bond length compared to the bond between hexagon-hexagon rings, because hexagon-hexagon rings are linked by a double bond.  $sp^2$  hybridizations are formed between all of the carbon atoms and every three neighboring carbon atoms are bound through a  $\sigma$  bond.  $p_z$  orbitals form degenerate  $\pi$  orbitals over the whole molecular cage. Figures 5.1(a) and 5.1(b) show the structure of a  $C_{60}$  molecule and the LUMO+1 isosurface plot for different orientations (LUMO: lowest unoccupied molecular orbital). As shown, the LUMO+1 has a ring-like structure and is localized on the pentagons forming the  $C_{60}$  skeleton [see Fig. 5.1(b)]. Figure 5.1(c) presents the corresponding STM images of the LUMO+1.

$C_{60}$  is potentially interesting for molecular electronics because of its high chemical and thermal stability. This has motivated over the past decade, an intense characterization of its intrinsic transport properties. Many studies have been done using  $C_{60}$  adsorbed on a surface or between electrodes. Interfacial properties are important in terms of electron transport and STM is the ideal tool to investigate them. In particular, it can be easily shown that  $C_{60}$  adopts various orientations upon adsorption onto a metal surface, and each orientation then produces a different metal-molecule interface. In order to get acquainted with these orientations, we

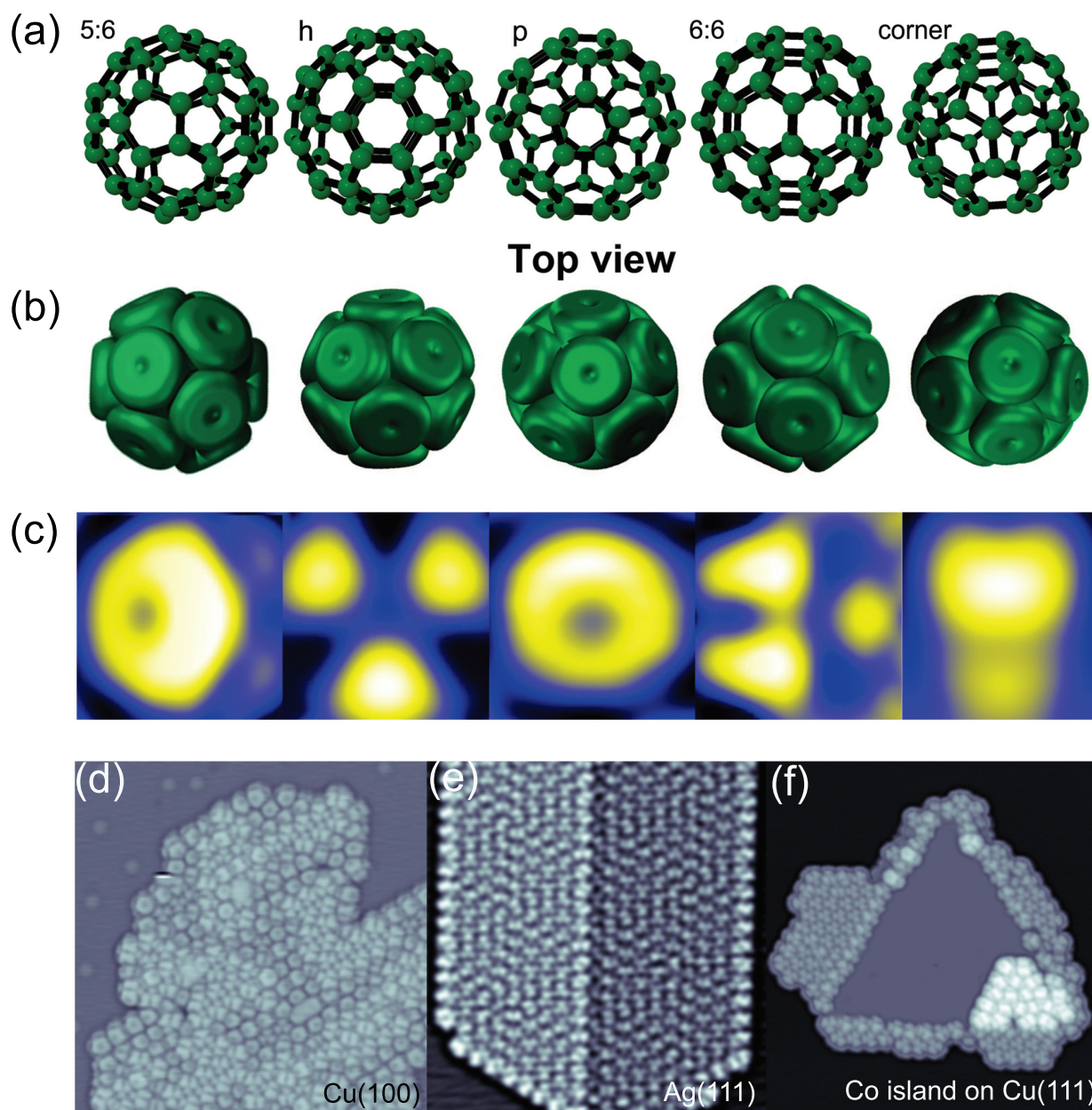


Figure 5.1: Top view of the C<sub>60</sub> structure, of the LUMO+1 isosurface and images of C<sub>60</sub>. (a) C<sub>60</sub> structure with different characteristic structural elements pointing up: a hexagon-pentagon bond (**5:6**), a hexagon ring (**h**), a pentagon ring (**p**), a hexagon-hexagon bond (**6:6**), and an apex atom (**corner**). (b) isosurface plots of the LUMO+1 corresponding to the orientations in (a). Isosurface plots adapted from Refs. [94, 115]. (c) Topographic images of a C<sub>60</sub> molecule on Cu(100) for each orientation as in (a) (gap condition:  $V = 1.9$  V,  $I = 0.5$  nA). (d) C<sub>60</sub> molecules on Cu(100) surface. (e) C<sub>60</sub> molecules on Ag(111). (f) C<sub>60</sub> molecules adsorbed on a Co island on Cu(111) surface. The images were taken at  $V = 1.9$  V,  $I = 0.5$  nA [Scan area:  $10 \times 10$  nm<sup>2</sup> for (d) and (e),  $20 \times 20$  nm<sup>2</sup> for (f)].



present the topography of  $C_{60}$  molecules adsorbed on various metal surfaces. Figures 5.1(d)—(e) present typical STM images of  $C_{60}$  adsorbed on Cu(100), Ag(111) and a Co island grown on Cu(111), respectively. Approximately 0.15 monolayers of  $C_{60}$  were dosed onto the surface from a crucible containing a 99.9% pure powder heated to 400°C (see section 2.1.2 for details). In this submonolayer coverage regime,  $C_{60}$  forms compact molecular islands.

$C_{60}$  has the possibility to have 5 dominant orientations on the surface as shown in Fig. 5.1, however even slightly tilted orientations are possible [211]. The different adsorption geometries can be identified by means of the imaged orbital symmetry of molecular states [212, 213], in particular of the LUMO+1. On Cu(100) [Fig. 5.1(d)], the dominant orientations are corner and hexagon with a population of 56% and 31%, respectively, while other orientations have a population below 5%. The bright and dim rows in Fig. 5.1(d) correspond to  $C_{60}$  molecules aligned along specific crystallographic directions of Cu(100). By combining STM and X-ray photoelectron diffraction, Abel *et al.* concluded that these stripe patterns are due to a  $C_{60}$ -induced missing-row reconstruction of the underlying substrate surface [214]. Approximately 99% of the molecules adsorb with a hexagonal facet on Ag(111) [see Fig. 5.1(e)]. On a Co island grown on Cu(111) [Fig. 5.1(f)], 95% of the molecules have a corner orientation, whereas on Cu(111) roughly 90% of the molecules have hexagon configuration.

Recent work by Schull *et al.* showed how to exploit a  $C_{60}$ -terminated tip to study the transport properties of a  $C_{60}$  or  $C_{60}$ - $C_{60}$  contact between two well defined electrodes [215, 216]. To do so, a  $C_{60}$  molecule was transferred from the surface to the tip. In this Thesis, this was carried out by positioning a metal tip (a tungsten tip coated with copper) above a  $C_{60}$  molecule. The sample bias was held at  $-0.2$  V while approaching the tip towards the molecule and simultaneously recording the current as a function of the tip displacement. A single  $C_{60}$  was attached to the copper-coated W tip by repeatedly bringing the tip into contact with the target molecule and pressing beyond contact [215]. Figure 5.2(b) shows the same zone as in Figure 5.2(a), but the central molecule where the contact was performed is now missing, resulting in a  $C_{60}$  picked up on the tip.

As shown by Schull *et al.* [Fig. 5.3(a)—(b)], a reverse image, or counter image, of the tip apex can be acquired by imaging an atom or a metallic cluster. Instead of obtaining a featureless image, a molecular pattern is observed within the atoms and clusters with the  $C_{60}$ -terminated tip. The molecular pattern corresponds to the orientation of the  $C_{60}$  molecule at the tip apex (see also Fig. 5.4). Additionally, the molecular tip may also be characterized by STS.  $C_{60}$  adsorbed on a surface has typically a highest occupied molecular orbital (HOMO) at

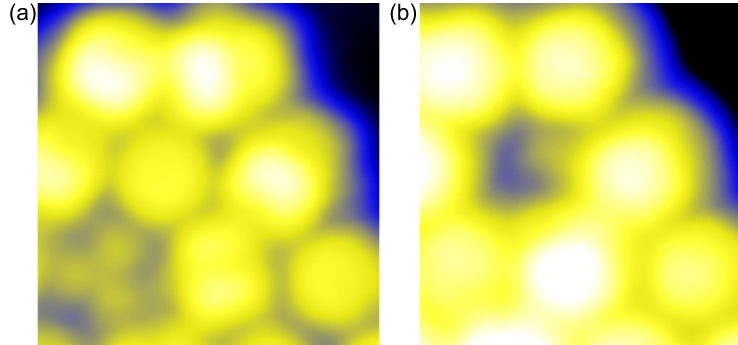


Figure 5.2: Topography before and after picking up  $C_{60}$  on the tip. (a) The  $C_{60}$  molecular layer on Cu(100) before picking up  $C_{60}$  on the tip. (b) The  $C_{60}$  molecule is picked up on the tip [scan image area:  $1.5 \times 1.5 \text{ nm}^2$ , gap condition:  $V = 1.9 \text{ V}$ ,  $I = 0.5 \text{ nA}$ ]. The left bottom molecule rotates from a hexagon to a pentagon orientation.

$-2 \text{ V}$ , a LUMO at  $0.5 \text{ V}$  and a LUMO  $+1$  at  $2.5 \text{ V}$  [Fig. 5.3(c)], although the position of the peaks changes with the  $C_{60}$ -metal interface (see Section 5.2.1). With a  $C_{60}$  molecular tip, the spectra are bias-reversed [Fig. 5.3(d)]. To understand the experimental reversed spectra, we need to recall Eq. (2.1):

$$I \propto \int_0^{eV} \rho_t(E - eV) \rho_{C_{60}}(E) dE, \quad (5.1)$$

where  $C_{60}$  is on the surface and the transmission factor  $T$  is assumed to be constant. For a constant tip DOS, the differential conductance is then proportional to the  $C_{60}$  DOS:

$$\frac{dI}{dV} \propto \rho_{C_{60}}(eV). \quad (5.2)$$

If now the molecule is attached to the tip, Eq. (2.1) is written as:

$$I \propto \int_0^{eV} \rho_{C_{60}}(E - eV) \rho_s(E) dE. \quad (5.3)$$

By introducing  $E - eV = E'$  we can rewrite:

$$I \propto \int_{-eV}^0 \rho_{C_{60}}(E') \rho_s(E' + eV) dE'. \quad (5.4)$$

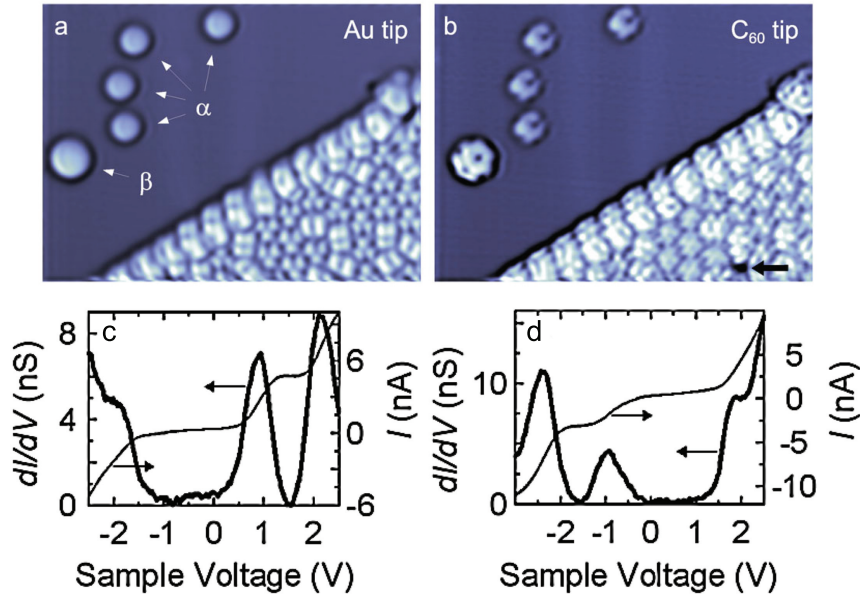


Figure 5.3: Topography and spectroscopy using a metallic and a  $C_{60}$  terminated tip. (a)-(b) Topographic images of  $C_{60}$  molecular layer, gold atoms ( $\alpha$ ) and a gold cluster ( $\beta$ ) on Au(111) surface using (a) a metallic tip and (b) a  $C_{60}$  terminated tip. The  $dI/dV$  spectra (c) on  $C_{60}$  with a metallic tip and (d) on metal surface with a  $C_{60}$  terminated tip [215].

Assuming the sample DOS as constant, then the differentiate conductance can be written as:

$$\frac{dI}{dV} \propto \frac{d}{dV} \int_{-eV}^0 \rho_{C_{60}}(E') dE', \quad (5.5)$$

and this leads to:

$$\frac{dI}{dV} \propto \rho_{C_{60}}(-eV). \quad (5.6)$$

Based on Eq. (5.2) and Eq. (5.6), the  $dI/dV$  is proportional to the molecular DOS, but for the case of the  $C_{60}$  terminated tip, the bias dependence is inverted. Unoccupied molecular orbitals will appear at negative bias, while occupied molecular orbitals appear at positive bias. The equivalent result can be obtained by changing the polarity of the bias in the STM junction. Functionalized molecular tips can also be built by picking up molecules such as CO or  $H_2$  to obtain an enhanced resolution in STM images [13, 14]. In Section 5.2, we present one of the first spectroscopic studies carried out with a molecular tip.

## 5.2 Spectroscopy with a molecular tip: Controlling NDC

Important advances have been made over the past decades in molecular electronics. It has been demonstrated for example that molecules can perform controllable functions such as negative differential resistance or conductance (NDC) [217–219]. First discovered in the Esaki diode [220], NDC leads to regions in the  $I - V$  curve where the current  $I$  decreases (increases) with increasing (decreasing) voltage  $V$ . This fundamental property is nowadays exploited in CMOS devices for low-power memory, fast switches or oscillators. Early atomic-scale observations of NDC by STM have been attributed to narrow energy states in tip and sample [221, 222], in analogy with the resonant tunneling leading to NDC in semiconductors [223]. In principle, resonant tunneling via molecular orbitals also leads to NDC in single molecules [224–226], but progress in this direction has been hindered by the lack of microscopic control over electrode and molecule status.

It was shown in particular with single  $C_{60}$  that NDC occurrence can be improved by narrowing the molecular levels through a reduced molecule-substrate coupling [227, 228], in order to exploit the bias-dependence of the transmission function [229, 230]. In this section, we introduce a different approach and report the occurrence of single-molecule NDC with a  $C_{60}$ -terminated tip. By attaching a molecule to the STM tip, an increased control is gained over the entire tunnel junction [14, 215]. This method allows, unlike previous NDC studies, exploring the NDC occurrence with well-defined pristine metal surfaces serving as a counterelectrode. Taking advantage of this setup, we demonstrate in stark contrast to conventional mechanisms that NDC can be produced by electron tunneling between a molecular orbital of the tip and a two-dimensional electron gas hosted by a copper surface —the Shockley surface states of Cu(111). In this calibrated setup, NDC may be tuned by varying the barrier thickness or by changing the  $C_{60}$  orientation up to complete extinction. Our study demonstrates that molecular orbitals act as angular momentum filters to the tunneling process, leading, in particular, to NDC if accurately matched with the local orbital symmetry of the surface states.

Theoretical support regarding DFT and transport calculations was provided by **Thomas Frederiksen**<sup>1</sup>.

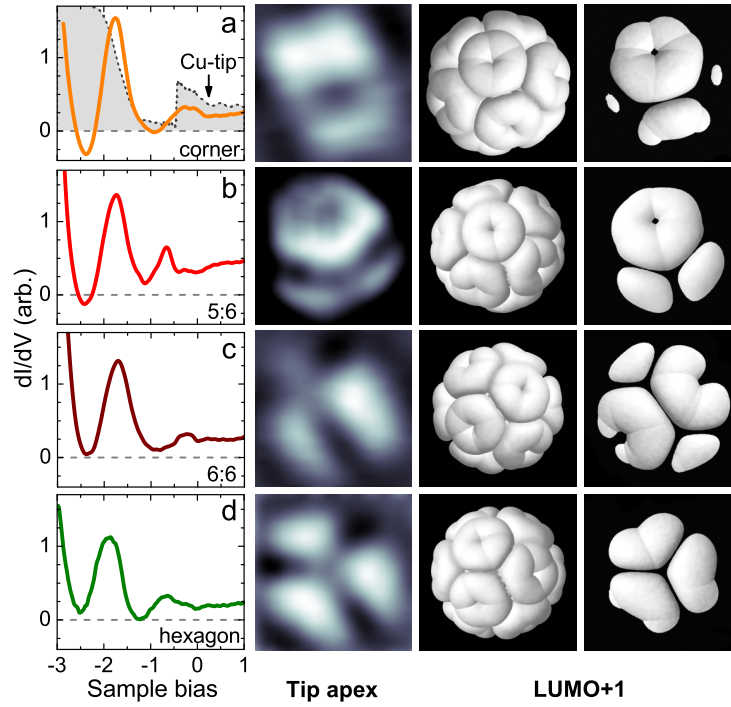


Figure 5.4: (a)—(d)  $dI/dV$  over Cu(111) for various  $C_{60}$  tips (1.0 V, 0.1 nA). The orientation of  $C_{60}$  at each tip apex is determined by constant-current images over a Au atom (sample bias:  $-2.0$  V, current: 0.1 nA, size:  $12 \times 12 \text{ \AA}^2$ ). Each orientation is flanked by a Hückel simulation of the LUMO+1 orbital, and for better visibility, by the same orbital cut along the  $xy$  plane (the LUMO+1 orbital is localized on the pentagons forming the  $C_{60}$  skeleton). Panel (a) present also a  $dI/dV$  spectrum over Cu(111) acquired with a copper-coated W tip (dashed line, feedback loop opened at  $-3.0$  V and 5 nA).

### 5.2.1 Influence of molecular orientation

We explored NDC occurrence for several orientations of  $C_{60}$  at the tip apex: corner, 5:6, 6:6, hexagon and pentagon. The tip apex was monitored through constant-current images of a Au atom, the image exhibiting a molecular pattern matching the LUMO+1 for biases close to  $-1.9$  V. After picking up the  $C_{60}$  on the tip, we can change the orientation of  $C_{60}$  at the tip apex by slightly touching the atom to study with the differently oriented  $C_{60}$  tips. Figure 5.4(a) presents the electronic structure of the Cu(111) surface acquired with a metal tip (dashed line). Known spectroscopic features are evidenced [231]. The steplike feature at  $-0.45$  V is associated to Shockley surface states, which are an experimental realization of a nearly two-

<sup>1</sup>Donostia International Physics Center (DIPC) at Donostia-San Sebastián in Spain

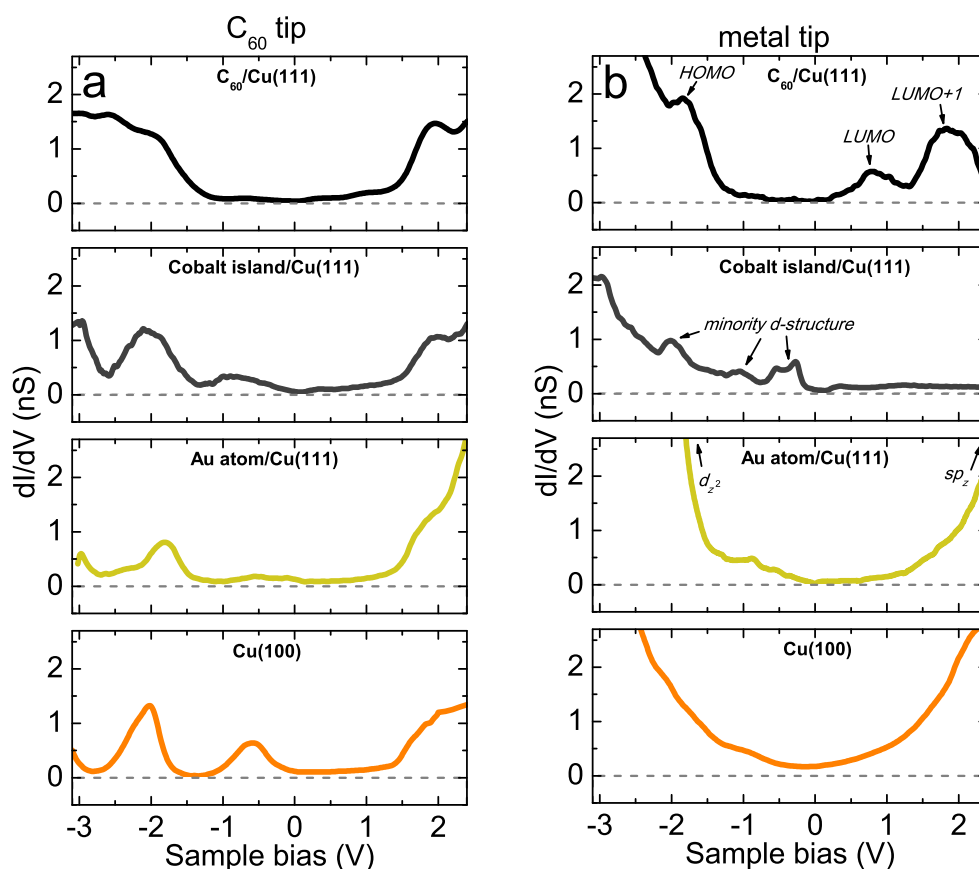


Figure 5.5: (a)  $dI/dV$  spectra acquired with a  $C_{60}$ -terminated tip (corner orientation) above, from top to bottom, a  $C_{60}$  molecule on Cu(111), a cobalt island on Cu(111), a Au atom on Cu(111), and a Cu(100) surface (feedback loop opened at 1.0 V, 0.1 nA). (b) Same spectra as in (a) but acquired with a copper-coated W tip. The arrows highlight the electronic structure of these nanoscale objects.

dimensional electron gas; the marked upturn below  $-0.9$  V is due to copper  $d$ -bulk states present below the (111) band gap. Figure 5.4 provides a conductance spectrum acquired with a  $C_{60}$  tip over Cu(111) for four different orientations of  $C_{60}$  as shown in the corresponding inverted images. The spectrum is nearly mirror symmetric to the spectrum acquired with a metallic tip positioned above a  $C_{60}$  molecule [compare with Fig. 5.3(c) and Fig. 5.5(b)]. The lowest unoccupied molecular orbitals are located at negative bias (LUMO:  $-0.5$  V, LUMO+1:  $-1.9$  V), while the highest occupied orbitals are at positive bias (HOMO:  $2.0$  V, not shown). The widths of the molecular states are typically  $0.5$  V and compare well with a  $C_{60}$  molecule adsorbed on a metal surface [232–234]. Most importantly, NDC is detected below the LUMO+1.

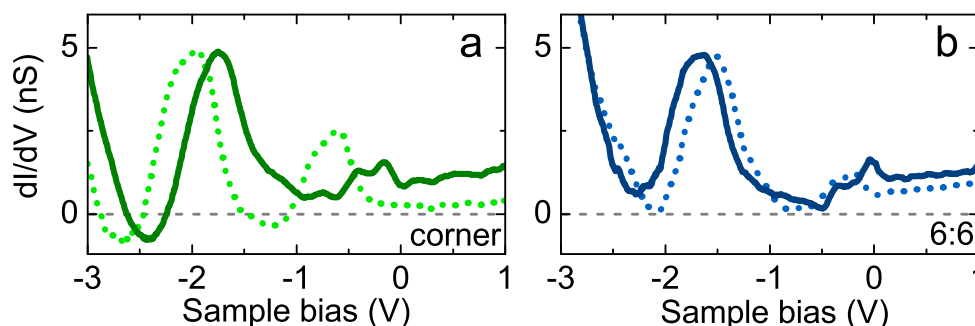


Figure 5.6:  $dI/dV$  acquired above Cu(111) with two different tips (1.0 V, 1.0 nA), having (a) same corner orientation for  $C_{60}$  [as in Fig. 5.4(a)], (b) same 6:6 orientation for  $C_{60}$  [as in Fig. 5.4(c)].

Among the numerous  $C_{60}$  tips investigated, the ones producing NDC had a specific  $C_{60}$  orientation relative to the copper surface. Figures 5.4(a)–(d) summarize our findings. As shown, counter images of the tip apex exhibit a molecular pattern matching the LUMO+1 for biases close to  $-1.9$  V. The orientations reported in Fig. 5.4 correspond to a  $C_{60}$  adsorbed on a carbon atom [labeled corner in Fig. 5.4(a)], on a pentagon-hexagon bond [5:6 in Fig. 5.4(b)], on a hexagon-hexagon bond [6:6 in Fig. 5.4(c)] and on a hexagonal ring [hexagon in Fig. 5.4(d)]. The apex  $C_{60}$  was rotated by performing a tip contact with a Au atom [114]. While the corner and the 5:6 adsorptions favor NDC, other orientations tend to suppress it.

We also found that the interface structure between the  $C_{60}$  molecule and the copper tip has only a limited impact on NDC. Typical spectra acquired with different  $C_{60}$ -tips, but with the same corner or 6:6 orientation are presented in Figs. 5.6(a) and 5.6(b), respectively. Despite the  $C_{60}$ -copper interface changes in these tips, as indicated by the shift of the LUMO and LUMO+1 (of the order of 0.5 and 0.2 V, respectively) [234], the dominant mechanism leading to NDC is still the  $C_{60}$  orientation.

Along with molecular orientation, counterelectrode selection is extremely crucial to NDC. In our setup, the counterelectrode can be conveniently chosen by positioning a  $C_{60}$  tip above nanoscale objects supported by Cu(111) or by changing the metal surface. In order to verify if counterelectrode selection is crucial to NDC, several counterelectrodes were inspected, either having a featureless electronic structure over the energy range of interest such as a Au atom on Cu(111) or the Cu(100) surface, either presenting a marked electronic structure such as a cobalt islands on Cu(111) [131], or a  $C_{60}$  molecule on Cu(111). We positioned the  $C_{60}$ -terminated

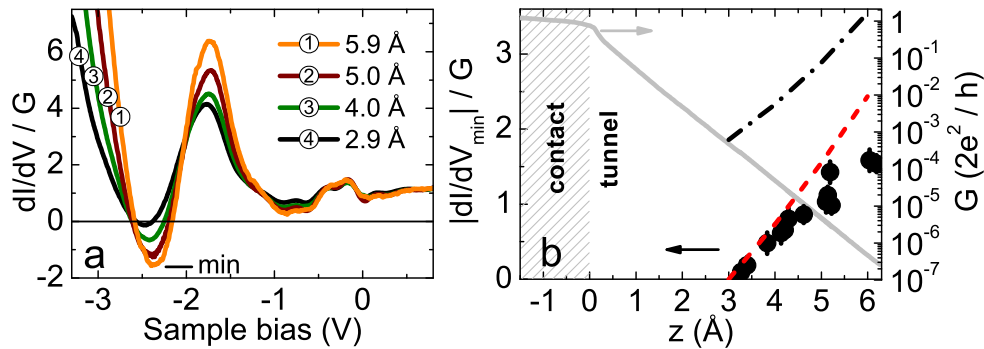


Figure 5.7: (a)  $dI/dV$  spectra for various barrier thicknesses. The spectra are normalized by the conductance ( $G = I/V$ ) at which the feedback loop was opened, respectively from top to bottom: 0.01, 0.1, 1 and 10 nS. (b) NDC intensity versus tip-sample distance (left vertical axis) and corresponding changes of  $G$  (right vertical axis). From the tunneling regime, we extract an apparent-barrier height of  $\Phi = 5$  eV. The distance is estimated by taking  $z = 0$  for the contact conductance ( $G$  vs  $z$  curve acquired at 1 V), the dashed area highlighting the contact regime. The NDC intensity corresponds to the minimum of the  $dI/dV$  curves in (a). The lines correspond to the simulation detailed in the text: a realistic DOS (dashed line) and a stepped DOS without  $d$ -bulk contribution (dash-dotted line).

tip above a Au atom adsorbed on Cu(111), or cobalt islands grown on Cu(111) as well as  $C_{60}$  molecules adsorbed on Cu(111) or on the cobalt islands. We also replaced the Cu(111) surface with a Cu(100) surface. The corresponding  $dI/dV$  spectra are presented in Fig. 5.5(a). The LUMO+1 is still detected, but the spectroscopic fingerprint changes with counterelectrode nature. In Fig. 5.5(b), we present for the sake of comparison the same spectra acquired with a copper-coated tip. The  $C_{60}$  molecule is governed by the HOMO, LUMO and LUMO+1 molecular resonances [232], the cobalt islands by minority  $d$ -resonances [131], the Au atom by atomic-like resonances ( $d_{z^2}$  resonance below  $-2$  V,  $sp_z$  resonance above 2 V) [235, 236]. The Cu(100) surface, on the contrary, has a featureless electronic structure. From Fig. 5.5(a), it is evident that no NDC is present below the LUMO+1. The fact that NDC is instead observed on Au(111) as on Cu(111) [237], tells us that electron tunneling into the Shockley surface states is likely a key mechanism behind NDC. This clearly indicates that the electronic structure of Cu(111) favors NDC despite the absence of narrow energy states on this surface.

For completeness, we investigated the influence of barrier thickness on NDC in the line of recent studies [228, 229, 238]. Figure 5.7(a) presents a typical set of spectra acquired at various distances, while Fig. 5.7(b) quantifies the changes in NDC with distance (noted  $z$ )



for a collection of  $C_{60}$ -tips. The d-bulk states and Shockley surface states have the opposite effect inducing the peculiar decay in NDC as a function of the tip displacement. Through a tip displacement it is possible to tune NDC and, unlike previous work, even switch it off well within the tunneling regime at a distance of 3 Å from surface. [we extract an apparent-barrier height of  $\Phi = 5$  eV from Fig. 5.7(b)]. As established below, NDC extinction is a general property of our simplified setup not exclusive to  $C_{60}$ .

### 5.2.2 WKB simulation and selection rules

We discuss the origin of the NDC with emphasis on the central role played by the Shockley surface states. To successfully engineer NDC, an accurate choice of the counterelectrode, of molecular orientation and of barrier thickness turns out to be crucial. To start, we adopt a WKB framework and focus on a junction comprising a sample metal surface and a  $C_{60}$  tip with density of states (DOS)  $\rho_s$  and  $\rho_t$ , respectively. The zero-temperature current  $I$  as a function of sample voltage  $V$  is then

$$I(V, z) \propto \int_{E_F-V}^{E_F} \sum_m \rho_s^m(E+V) \rho_t^m(E) T(E, V, z) dE, \quad (5.7)$$

where  $T(E, V, z) = \exp(-2\sqrt{2(\Phi - V/2 - E)}z)$  is the transmission function in Hartree atomic units. The explicit summation over magnetic quantum numbers  $m$  (projection of electron angular momentum on the common symmetry axis) excludes the extremely small probability for tunneling between states with different  $m$  [226,239]. For an accurate description of the tunneling current, we need just to distinguish between  $m = 0$  and  $m \neq 0$  in the DOS. This distinction is necessary as, near  $\Gamma$ , the  $sp$ -like Shockley surface states of Cu(111) only couple to the  $m = 0$  component of the tip states. To model the sample DOS, we thus take a stepped function centered at  $-0.45$  eV for the surface states and a low-energy exponential upturn for the copper bulk  $d$ -states to represent  $\rho_s^{m=0}$  [dashed line, negative half-plane, Fig. 5.8(a)] and a constant background plus exponential upturn for  $\rho_s^{m \neq 0}$  [dotted line, negative half-plane, Fig. 5.8(a)]. The total DOS (dash-dotted line) roughly mimics the electronic structure evidenced in Fig. 5.4(a). For the  $C_{60}$ -tip we represent  $\rho_t$  as a set of three Lorentzian peaks for the HOMO, LUMO, and LUMO+1 as described in the Fig. 5.8(a). Three Lorentzian peaks represent the HOMO ( $-2.0$  eV), LUMO ( $0.4$  eV) and LUMO+1 ( $1.9$  eV) with widths  $0.5$  eV,  $1.0$  eV, and  $0.5$  eV, respectively. The  $m = 0$  (dashed line) and  $m \neq 0$  (dotted line) components sum up (thick line)

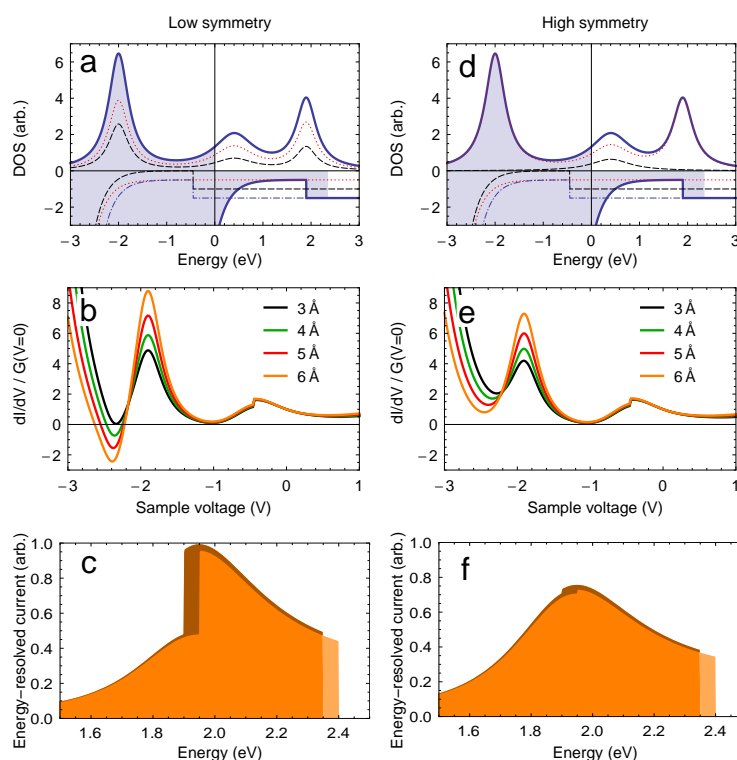


Figure 5.8: (a) DOS of low-symmetry  $C_{60}$ -tip (upper half-plane, thick line) and Cu(111) surface (lower half-plane, dash-dotted line:  $V = 0$  V, thick line:  $V = -2.35$  V) used in the WKB simulation ( $m = 0$  and  $m \neq 0$  components shown with dashed and dotted lines, respectively). (b) Simulated  $dI/dV$  for (a) via Eq. (5.7). (c) Energy-resolved current for  $V = -2.35$  V (dark orange) and  $V = -2.40$  V (light orange) for  $z = 6$  Å. (d)–(f) Similar to (a)–(c) but for a high-symmetry  $C_{60}$  orientation where the  $m = 0$  component is suppressed for HOMO and LUMO+1.

to amplitudes proportional to the free-molecule degeneracies. The occupied states are indicated by the shaded blue areas for the sample voltage  $V = -2.35$  V where the Shockley surface state edge matches the LUMO+1 resonance.

As shown in Fig. 5.8(b), the corresponding simulated  $dI/dV$  captures the essential experimental facts. There is indeed NDC in the spectrum just below the LUMO+1 down to distances close to  $z = 3$  Å. The role of the Shockley surface states in the NDC is evident from the energy-resolved current shown in Fig. 5.8(c): At a sample voltage  $V = -2.35$  V, the surface state onset matches the LUMO+1 resonance [221,222]. Upon a slight increase in the voltage the surface state step feature moves away from the molecular resonance. The associated loss in energy-resolved current (dark orange area) is only partially compensated by the corresponding

	isolated	5:6/corner	6:6	hexagon	pentagon
	$I_h$	$C_s$	$C_{2v}$	$C_{3v}$	$C_{5v}$
HOMO	$H_u$	$2A'+3A''$	$A_1+2A_2+B_1+B_2$	$A_2+2E$	$A_2+E_1+E_2$
LUMO	$T_{1u}$	$2A'+A''$	$A_1+B_1+B_2$	$A_1+E$	$A_1+E_1$
LUMO+1	$T_{1g}$	$A'+2A''$	$A_2+B_1+B_2$	$A_2+E$	$A_2+E_1$

Table 5.1:  $C_{60}$  orbitals in different local symmetries imposed by molecular orientation with respect to an isotropic surface.

shift of the sample chemical potential (light orange area), the tunnel current effectively *decreases* thus giving rise to NDC. Simulations also show that NDC is favoured when the energy position of the surface-state onset is comparable to the width of the LUMO+1, which is indeed the case in the present setup. The comparison to our experimental results is also satisfying as shown by the dashed line in Fig. 5.7(b), where we also include the NDC produced by a stepped function (dash-dotted line) without the *d*-bulk upturn. The increased NDC intensity without the *d*-states highlights that *d*-bulk states are detrimental to NDC. The peculiar decay reported in Fig. 5.7(b) is therefore the result of a competition between opposite effects for *d*-states and Shockley surface states.

Another salient experimental finding is the impact of  $C_{60}$  orientation on NDC, which was set aside in the above discussion. In Fig. 5.4, it was found that NDC occurs with  $C_{60}$  in low-symmetry configurations (e.g., corner orientation) but disappears in high-symmetry configurations (e.g., hexagon orientation). Our NDC originates from the Shockley surface states which select  $m = 0$  tip states. This suggests that for the high-symmetry  $C_{60}$  orientations, the  $m = 0$  component of the LUMO+1 vanishes. Indeed such an effect can be rationalized by considering the transformation properties of the  $C_{60}$  tip orbitals using group theory as follows.

For isolated  $C_{60}$  molecules of icosahedral symmetry  $I_h$ , the HOMO is a fivefold degenerate state of  $H_u$  symmetry while the LUMO and LUMO+1 are triply degenerate states of  $T_{1u}$  and  $T_{1g}$  symmetry, respectively. When the molecule is adsorbed on a surface, these degeneracies will be reduced [240], and, importantly here, the orbital angular momentum components onto the common symmetry axis perpendicular to the surface will depend on the molecular orientation. In Tab. 5.1 we list how the orbitals are split in different relevant local symmetry environments. For instance, a  $C_{60}$  molecule adsorbed with a hexagon on an isotropic surface possesses a threefold rotation axis and can thus be considered as belonging to the  $C_{3v}$  group. As a consequence it can be shown that the  $T_{1g}$  LUMO+1 splits into  $A_2+E$  representations [241]. However, from the

character table of  $C_{3v}$ , it is evident that  $s$ ,  $p_z$ , and  $d_{z^2}$  orbitals do not transform according to those representations. In other words, the LUMO+1 does not have a  $m = 0$  component for the hexagon orientation. Contrarily, a  $C_{60}$  molecule adsorbed on a 5:6 bond or a corner atom only possesses bilateral symmetry as described by  $C_s$ , and the LUMO+1 is split into  $A' + 2A''$ . As  $s$ ,  $p_z$ , and  $d_{z^2}$  do transform in  $C_s$  according to those representations, the LUMO+1 consequently contains a  $m = 0$  component in these low-symmetry configurations.

More generally, based on Tab. 5.1 we can conclude that tunneling into the surface state is symmetry forbidden for orbitals which do not transform as the totally symmetric representation ( $A'/A_1$ ), *i. e.*, the HOMO for pentagon and hexagons orientations and the LUMO+1 for 6:6, pentagon, and hexagon orientations. Note also that there are no such symmetry constraints for the LUMO orbital. To simulate the  $dI/dV$  recorded with  $C_{60}$  tips with high-symmetry orientation, we therefore eliminated the  $\rho_t^{m=0}$  component in HOMO and LUMO+1 [Fig. 5.8(d)]. As shown in Fig. 5.8(e)—(f), indeed this leads to the disappearance of NDC as was observed experimentally [Fig. 5.4(c)—(d)].

To summarize, we have shown that electron tunneling between a well calibrated molecule and a two-dimensional electron gas produces a tunable NDC. By controlling both tip and sample states and accounting for their symmetries, we demonstrated the concept of local orbital symmetry matching [226]. Barrier thickness or symmetry matching between the molecule and the counterelectrode can be used to switch the NDC on and off. As dispersive two-dimensional electronic states are widely available in metals and semiconductors, and moreover may be controllably modified through artificial nanostructures or molecular adlayers, our findings should simplify NDC engineering in atomic-scale metal-organic junctions.

### 5.3 Evolution of the Kondo resonance in a $C_{60}$ -Co contact

The symmetry of the local environment of atoms and molecules influences their electronic structure. An artificial manipulation of this environment can be pursued by attaching atoms and molecules together to form new metal complexes. This procedure can change the symmetry of the ground state and lift the degeneracy of magnetic energy levels. The Kondo physics as well as vibrational excitations and molecular magnetism can therefore be affected [26–28, 30, 242–244]. Although significant experimental progress has been made, there is a general lack of control over the response of the system. Control can be gained through the tip contact to adsorbates

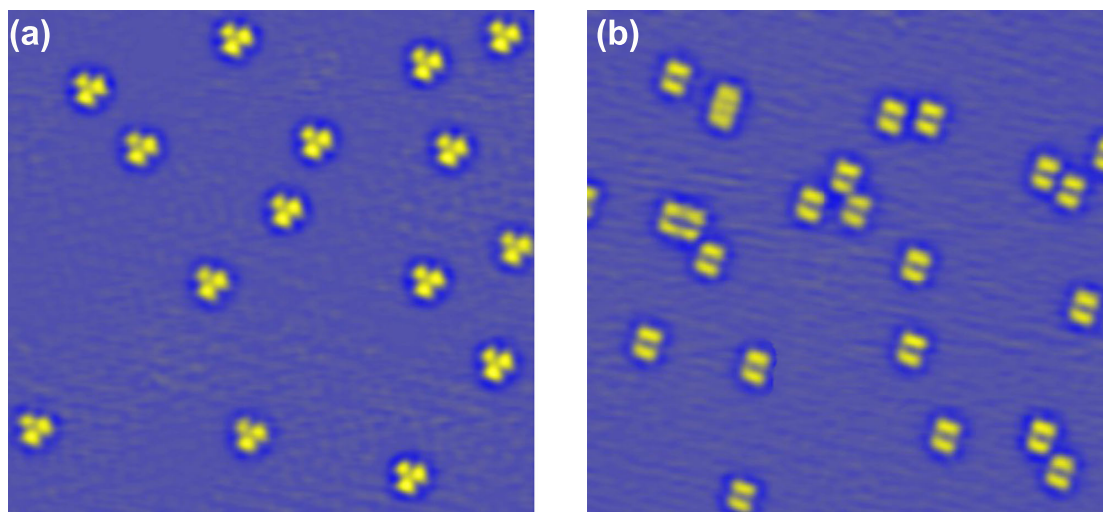


Figure 5.9: Counter images of Co adatoms on Cu(100) using a  $C_{60}$  terminated tip. (a) Hexagon orientation and (b) 6:6 orientation of  $C_{60}$  on the tip. The images were taken at  $V = -1.9$  V and  $I = 0.5$  nA [scan size:  $8.5 \times 8.5$  nm<sup>2</sup>].

on a surface using STM. We have seen in Chapter 3 how it is possible with an atom. Here, we explore the electron transport on a molecular complex using a Co adatom on Cu(100) in contact with a  $C_{60}$ -terminated tip. Preliminary results show that the Kondo effect of Co is modified in a  $C_{60}$ -Co complex.

### 5.3.1 Conductance of the $C_{60}$ -Co junction

To build the molecular junction, we start by preparing the  $C_{60}$ -terminated tip as described in Section 5.1. For all the tips used, counter images of single atoms were acquired to determine the orientation of  $C_{60}$  at the tip apex as shown in Fig. 5.9. For example,  $C_{60}$  is clearly adsorbed on the tip with a hexagonal facet in Fig. 5.9(a), and is instead adsorbed on 6:6 bond in Fig. 5.9(b). Having identified the molecular orientations of  $C_{60}$ , we then systematically carried out conductance versus tip displacement measurements above a single Co atom. Figure 5.10(a) presents the typical dependence of the conductance in units of  $G_0$  on  $z$  ( $C_{60}$  orientation had only a minor impact on these measurements). The displacement axis shows the tip excursion towards the atom and  $z = 0$  corresponds to the position of the tip before opening the feedback loop. The tip is then moved towards the atom ( $z < 0$ ) by more than  $4.5$  Å, while the current is simultaneously recorded to explore the evolution of the conductance. Typical characteristics

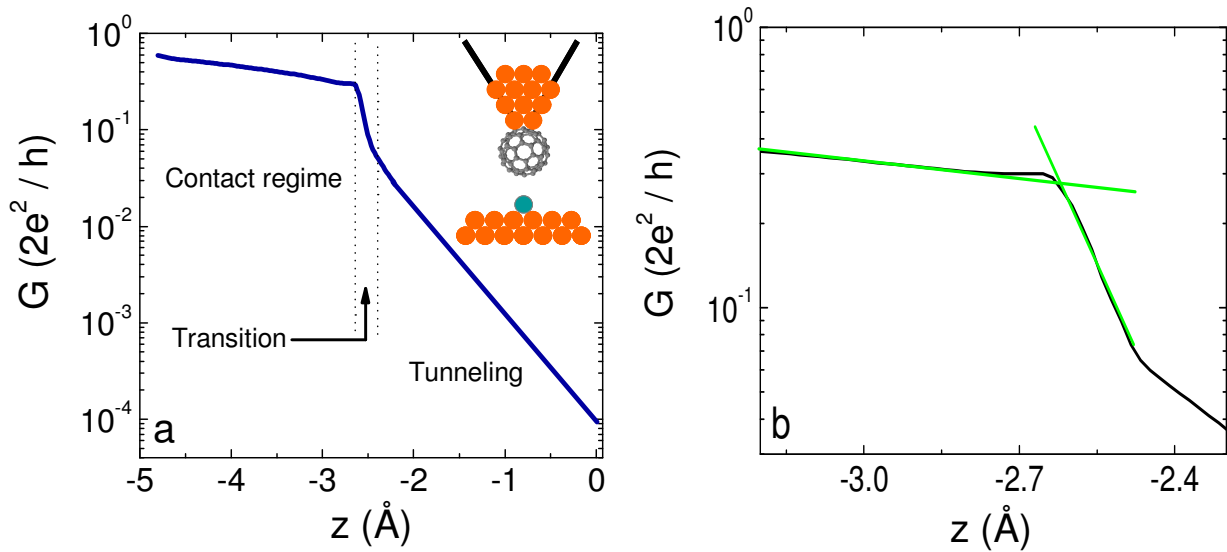


Figure 5.10: (a) Conductance versus tip displacement of a Co adatom/Cu(100) using a pentagon oriented C<sub>60</sub> tip ( $V = 200$  mV). The curve is an average of 20 measurements. The dotted lines indicate the boundaries among the three different conductance regimes. Inset: sketch of the Co-C<sub>60</sub> junction used. (b) Zoom-in on the transition to contact regime. The green lines are used to estimate the contact conductance ( $G_c$ ). The conductance overshoots just after contact.

of the conductance curve are as follows. Between  $z = 0$  and  $z = -2.3$  Å the conductance varies exponentially from  $10^{-4} G_0$  to  $0.03 G_0$  consistent with electron tunneling between tip and sample states. The apparent barrier height is  $\Phi = 5.8$  eV. The value is higher than the one of the bare copper surface (5 eV, see Fig. 5.7) due to the charge transfer between the atom and the surface as discussed in Section 3.1.1. Starting from  $z = -2.3$  Å, we observe a deviation from exponential behavior. A sharp increase of the conductance by a factor of ten occurs within a displacement interval of 0.4 Å. This interval corresponds to the transition regime [110] and is considerably smaller than the one observed with a metallic tip [see Fig. 5.10(b)]. In single conductance curves, the transition actually corresponds to a jump-to-contact, but due to the small variation in the exact location of this increase, averaging leads to some broadening. Upon further approach, the conductance exhibits a small increase with decreasing tip-molecule distance—the system enters the contact regime. For tip excursions  $z < -4.8$  Å, instabilities and/or damage to the tip were often observed in agreement with a previous study [114].

The contact conductance amounts to  $G_c = 0.3 \pm 0.05 G_0$  for all orientations observed. Figure 5.10(b) shows the graphical definition of the contact conductance  $G_c$ . This contact

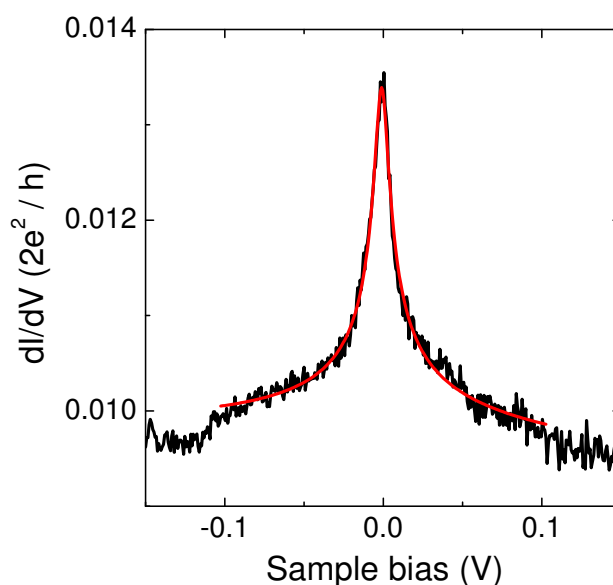


Figure 5.11: Tunneling spectrum of a Co adatom using an hexagon-oriented  $C_{60}$  tip. The red line corresponds to a Frota fit, and yields  $T_K = 37$  K. A Lorentzian fit gives  $T_K = 78$  K (factor 2 difference).

conductance is consistent with recent finding of Schull *et al.* who reported that the contact conductance in  $C_{60}$  junctions is not an intrinsic properties of the molecule, but can be related to the interfacial properties with the metal electrodes [216]. They observed a variation of the conductance up to a factor 20 when increasing the number of metal atoms in contact with  $C_{60}$ . In an asymmetric junction where  $C_{60}$  is in contact with a surface on one side, and in contact with a cluster comprising a finite number of atoms on the other side, charge injection into the molecule is limited by the size of the cluster. To attain a diffusive regime, the cluster must comprise at least 5 atoms and below this “critical” value, the contact conductance decreases due to the bottle neck structure of a constriction. The contact conductance is then  $2G_0$  in the diffusive regime, where the molecule orbital governs transport. This  $2G_0$  contact value reflects the splitting of the three fold degeneracy of the LUMO, which governs the electron transport of the junction near  $E_F$ .

### 5.3.2 Impact of the molecular tip on the Kondo resonance

The Kondo effect of Co on Cu(100) exhibits substantial differences when a  $C_{60}$ -tip is employed instead of a metal tip as discussed in Chapter 3. Differences already appear in the tunneling

regime, but are extremely striking when a  $C_{60}$ -Co contact is established. As shown in Fig. 5.11, in the tunneling regime, the resonance is peak-like for all orientations, and is no longer step-like as previously found with a metallic tip (Figs. 2.9 and 3.10). The peak-like shape is well described by a Frota function (see Section 3.3.4), which closely reproduces the ASK resonance calculated by numerical renormalization group theory. The Kondo temperature extracted amounts to  $T_K = 40$  K. When using a Lorentzian fit,  $T_K$  amounts to 80 K—a factor 2 difference is indeed expected for  $T_K$  between the two fits [147]. The Kondo effect of Co on Cu(100) is therefore same as previously evidenced with a metallic tip, but the molecular apex modifies the way electrons tunnel into the Kondo impurity given the change in the lineshape of the resonance. Such a change may be interpreted by recalling the Fano theory introduced in Section 2.4.1. Electrons can tunnel from the  $C_{60}$  tip directly into the Kondo resonance, but can also tunnel into the surface. The ratio between these pathways determines the Fano parameter  $q$  and changes the shape of the Kondo resonance. The peak-like shape detected would then reflect an enhancement of the tip-atom tunneling matrix element. The tunneling matrix element between a tip and a surface is known to be dependent on the nature of the tip state. Chen has for example shown that the tunneling matrix element is enhanced for  $d_{z^2}$  tip states compared to  $s$  tip states [239]. Similarly, the LUMO of  $C_{60}$  which is present near  $E_F$  may favor an enhancement of the tunneling into the Kondo resonance of the Co atom compared to a metallic tip. To fully validate this interpretation, a theoretical analysis is required.

The most striking and new results are obtained at contact (Fig. 5.12). At first glance, the spectral lineshape in the contact regime could be interpreted as a dip-like Kondo resonance, but this viewpoint is inconsistent with the results shown in Chapter 3. There we showed that  $T_K$  increases as a function of tip displacement, which then would imply that the dipped feature should increase with tip displacement at variance with observations. Our results rather show a splitting of a peak-like resonance and finally restoring of the Kondo resonance, all occurring in the contact regime. The resonance right after the contact splits apart by 30 meV, and is progressively restored as the tip excursion increases. Our findings are independent on molecular orientation.

A fascinating scenario to describe our results is to assume that the  $C_{60}$ -Co system is a two impurity-Kondo system, as described in Sections 1.3.3 and 2.4.2. Within this scenario, the cobalt atom carries a Kondo ground state, as well as  $C_{60}$ .  $C_{60}$  has been indeed shown to possess a Kondo effect [9, 245]. Assuming that the Kondo temperature of  $C_{60}$  is much lower than for Co ( $T_K(C_{60}) \ll T_K(\text{Co})$ ), the feature detected corresponds to the ASK resonance



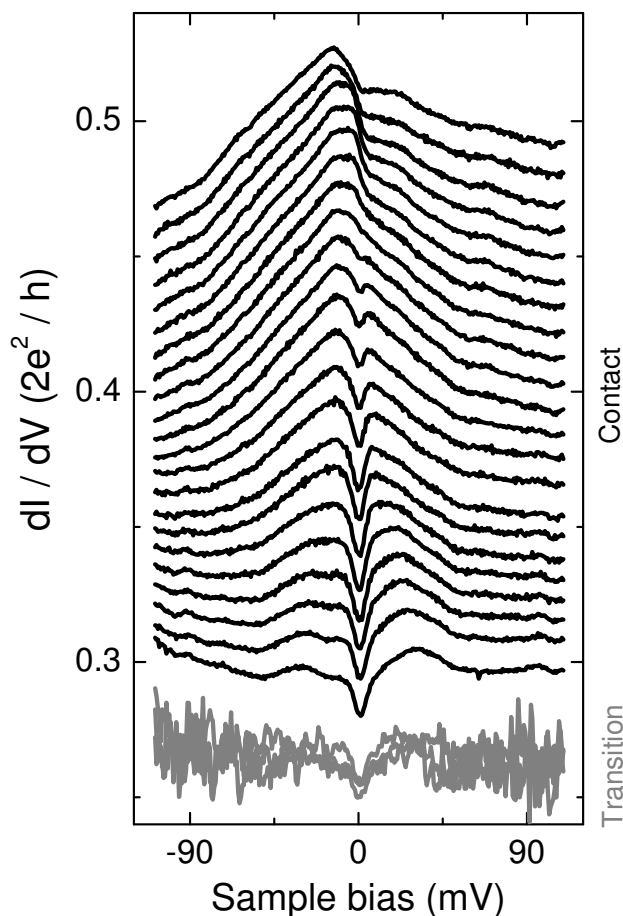


Figure 5.12: Evolution of the  $dI/dV$  spectra of a Co adatom in contact with  $C_{60}$  tip from transition to contact. The color code corresponds to the conductance regimes: transition (gray) and contact (black). In the transition regime, the sharp change in the conductance reduces the signal-to-noise ratio.

of Co, perturbed by the magnetic interaction with  $C_{60}$ . The  $C_{60}$ -Co interaction needs to be antiferromagnetic (AFM) in order to explain the resonance splitting observed (Section 1.3.3). The splitting of the resonance and then the restoring correspond to a cobalt moving from an AFM ground state to a Kondo ground state, driven by the tip-assisted displacement of Co into the surface. To support this scenario, we therefore need to verify two things. First of all,  $C_{60}$  should carry a spin and secondly the coupling between  $C_{60}$  and Co should be AFM. DFT calculations regarding the Co- $C_{60}$  junction are currently being carried out by **Aran Garcia Lekue** and **Thomas Frederiksen**<sup>1</sup> to understand what we observed experimentally.

## Summary and conclusions

In this Chapter, we investigated electron transport using a  $C_{60}$ -terminated tip.  $C_{60}$  is a highly promising candidate molecule for molecular electronics. After detailing how to prepare and characterize such a tip, we presented a detailed spectroscopic study focused on NDC. In particular, low-temperature STM and STS were employed to investigate electron tunneling from a  $C_{60}$ -terminated tip into a Cu(111) surface. Tunneling between a  $C_{60}$  orbital and a two-dimensional electron gas hosted by copper surface is shown to produce NDC contrary to conventional mechanisms. We showed that NDC is observed only with low symmetry orientations of  $C_{60}$  at the tip apex. This orientation dependence is a result of a symmetry matching between the molecular tip and the surface states of Cu(111). Barrier thickness can also be used to tune NDC.

In the second part of this Chapter, we presented preliminary results on the Kondo effect in a  $C_{60}$ -Co junction. Contrary to the Kondo resonance detected above Co adatom on Cu(100) with a metallic tip, a peak-like shape is obtained in the tunneling regime with a  $C_{60}$  terminated tip. The modified lineshape is assigned to an increase tip-atom coupling probably due to the presence of the  $C_{60}$  LUMO at  $E_F$ . In the contact regime, the splitting and the restoring of the Kondo resonance are evidenced, which might be explained within a two impurity-Kondo problem.



# Conclusion and perspectives

Spintronic devices are based on the control and manipulation of spin degrees of freedom in solid-state systems and show promising advantages compared to current devices such as non-volatility, faster data processing speed and efficient power consumption. Spin transport, spin dynamics as well as spin relaxation time should be well understood to functionalize these devices. Moreover, spin injection is needed to write and store the data, and spin detection is required to read out the data. This is possible through the giant magnetoresistive (GMR) or tunneling magnetoresistive (TMR) effects which were discovered in sandwiched ferromagnet/nonmagnet/ferromagnet structures [176, 177], and in ferromagnet/insulator/ferromagnet structures [174, 175], respectively. Since then, many studies have been pioneered. A growing issue in spintronics is to reduce the size of the devices to boost data storage. In this respect, the IBM group of the Almaden Research Center discovered recently that an antiferromagnetic array of a few Fe atoms can act as one bit in a spintronic device [246]. As size is reduced, both the writing and reading processes become extremely challenging. The read sensor must be downsized to match the dimension of the magnetic bit, but at the same time, its sensitivity must be improved to compensate the loss in signal-to-noise ratio produced by the downscaling. For spin detection, the main aim is then to maximize the sensitivity to detect changes of spin states at the smallest possible scale. This Thesis was devoted at mounting such a challenge by exploiting the Kondo effect of a single atom.

When the scale of the objects becomes smaller, the physics of nanostructures reveals several remarkable quantum effects such as the Kondo effect. The Kondo effect, which involves electron-electron correlations, occurs when a localized magnetic moment is screened by the spins of the host metal conduction electrons. Below a typical temperature known as Kondo temperature, this many-body interaction results in the emergence of a resonance in the density of states located near the Fermi energy level. In Chapter 1, we presented an overview of the Kondo effect. For more than a decade, such a resonance has been investigated by transport

measurements in single Kondo impurities, consisting of magnetic atoms or artificial quantum dots (QD). Of particular interest for the emerging field of spintronics is the interaction of single Kondo impurities with their magnetic surroundings since the Kondo resonance is sensitive to this environment. By using a scanning tunneling microscope (STM), we then showed how spin transport may be detected also with a Kondo resonance. The STM is an ideal tool to study the physical properties of nanostructure since it allows manipulating the system easily as well as provides spectroscopic information (STS) which is related to the density of states. The experimental setup we used was detailed in Chapter 2 including the working principle of STM and acquisition of topography and spectroscopy.

To enable the detection of the spin transport, we showed that it is necessary to build well-controlled single atom junctions. In Chapter 3, we exploited the ability of an STM to form quantum point contacts with microscopic control. We focused on the evolution of the Kondo effect of a Co atom from the tunneling to the contact regime. The width of the Kondo resonance was shown to vary exponentially with the ballistic conductance for all tips employed. Using a theoretical description based on the Anderson model, we showed that the Kondo effect and the total conductance are related through the atomic relaxations affecting the environment of a Co atom.

Having mastered the Kondo effect of a single Co atom, we used it for an atomic scale detection of the spin injection. We reported in Chapter 4, the detection of a spin-polarized current flowing across a Co by exploiting the interplay between Kondo correlations and itinerant-electron ferromagnetism. Detection is achieved with a quantum-point contact comprising a single Kondo impurity, where current densities are sufficiently high to promote a splitting of the Kondo resonance. To understand the system from a theoretical point of view, calculations were also performed and showed a nice agreement with the experimental observations. Our findings showed that spin injection into a single atom is feasible and, moreover, that it can be controlled by altering the chemical properties of the contact.

Beyond the scope of spintronics, we extended our finding to a molecular system in Chapter 5. Instead of studying a single molecule on the surface, we picked up a single molecule on the tip and employed it to form hybrid metal-molecule junctions exhibiting a Kondo effect. Prior to this study, we showed how such a tip may be exploited to tackle fundamental aspects of molecular electronics. We then focused on the quantum point contact between the molecular tip and a single Co atom carrying a Kondo effect. A splitting and restoring of the Kondo resonance were detected at contact, which we interpreted in terms of a two Kondo impurity

problem. Calculations are currently being performed to validate this scenario.

Spin injection and detection at the atomic scale were demonstrated in this Thesis using the Kondo effect. Fulfilling the demand to decrease the size of the spintronic devices, the Kondo effect can be the perfect probe to detect the changes of magnetic states at the atomic scale. In this respect, we can also apply this approach to the molecular system to inject and detect the spins through a molecular complex or a single molecule for the advancement of molecular spintronics.



# Bibliography

- [1] W. Meissner and B. Voigt. Measurements with the aid of liquid helium: Xi. resistance of pure metals at low temperatures. *Annalen der Physik*, **399**(8):892–936, 1930.
- [2] J. Kondo. Resistance Minimum in Dilute Magnetic Alloys. *Prog. Theor. Phys.*, **32**(1):37–49, 1964.
- [3] J. Kondo. Effect of Ordinary Scattering on Exchange Scattering from Magnetic Impurity in Metals. *Phys. Rev.*, **169**(2):437–440, 1968.
- [4] M. D. Daybell and W. A. Steyert. Localized Magnetic Impurity States In Metals: Some Experimental Relationships. *Rev. Mod. Phys.*, **40**(2):380–389, 1968.
- [5] D. Goldhaber-Gordon, H. Shtrikman, D. Mahalu, D. Abusch-Magder, U. Meirav, and M. A. Kastner. Kondo effect in a single-electron transistor. *Nature*, **391**:156–159, 1998.
- [6] Sara M. Cronenwett, Tjerk H. Oosterkamp, and Leo P. Kouwenhoven. A Tunable Kondo Effect in Quantum Dots. *Science*, **281**(5376):540–544, 1998.
- [7] V. Madhavan, W. Chen, T. Jamneala, M. F. Crommie, and N. S. Wingreen. Tunneling into a Single Magnetic Atom: Spectroscopic Evidence of the Kondo Resonance. *Science*, **280**(5363):567–569, 1998.
- [8] Jiutao Li, Wolf-Dieter Schneider, Richard Berndt, and Bernard Delley. Kondo Scattering Observed at a Single Magnetic Impurity. *Phys. Rev. Lett.*, **80**(13):2893–2896, 1998.
- [9] Abhay N. Pasupathy, Radoslaw C. Bialczak, Jan Martinek, Jacob E. Grose, Luke A. K. Donev, Paul L. McEuen, and Daniel C. Ralph. The Kondo effect in the Presence of Ferromagnetism. *Science*, **306**(5693):86–89, 2004.
- [10] H. B. Heersche, Z. de Groot, J. A. Folk, L. P. Kouwenhoven, and H. S. J. van der Zant. Kondo Effect in the Presence of Magnetic Impurities. *Phys. Rev. Lett.*, **96**(1):017205, 2006.
- [11] Gavin David Scott and Douglas Natelson. Kondo Resonances in Molecular Devices. *ACS Nano*, **4**(7):3560–3579, 2010.
- [12] M. Reyes Calvo, Joaquín Fernández-Rossier, Juan José Palacios, David Jacob, Douglas Natelson, and Carlos Untiedt. The Kondo effect in ferromagnetic atomic contacts. *Nature*, **458**:1150–



- 1153, 2009.
- [13] Jascha Repp, Gerhard Meyer, Sladjana M. Stojković, André Gourdon, and Christian Joachim. Molecules on Insulating Films: Scanning-Tunneling Microscopy Imaging of Individual Molecular Orbitals. *Phys. Rev. Lett.*, **94**(2):026803, 2005.
- [14] Leo Gross, Nikolaj Moll, Fabian Mohn, Alessandro Curioni, Gerhard Meyer, Felix Hanke, and Mats Persson. High-Resolution Molecular Orbital Imaging Using a p-Wave STM tip. *Phys. Rev. Lett.*, **107**(8):086101, 2011.
- [15] P.W. Anderson. Localized Magnetic States in Metals. *Phys. Rev.*, **124**(1):41–53, 1961.
- [16] A. A. Abrikosov. Renormalization Group from Diagrammatic Calculations with Kondo Spin Represented by a Pseudofermion. *Physics*, **2**:5, 1965.
- [17] Gerd Bergmann. Quantitative calculation of the spatial extension of the Kondo cloud. *Phys. Rev. B*, **77**(10):104401, 2008.
- [18] Erik S. Sørensen and Ian Affleck. Scaling theory of the Kondo screening cloud. *Phys. Rev. B*, **53**(14):9153–9167, 1996.
- [19] C. A. Büsser, G. B. Martins, L. Costa Ribeiro, E. Vernek, E. V. Anda, and E. Dagotto. Numerical analysis of the spatial range of the Kondo effect. *Phys. Rev. B*, **81**(81):045111, 2010.
- [20] J. R. Schrieffer and P. A. Wolff. Relation between the Anderson and Kondo Hamiltonians. *Phys. Rev.*, **149**(2):491–492, 1966.
- [21] James S. Schilling and W. B. Holzapfel. Effect of Pressure on the Kondo Temperature of Cu:Fe-Existence of a universal resistivity curve. *Phys. Rev. B*, **8**(3):1216, 1973.
- [22] F. D. M. Haldane. Scaling Theory of the Asymmetric Anderson Model. *Phys. Rev. Lett.*, **40**(6):416–419, 1978.
- [23] Leo Kouwenhoven and Leonid Glazman. Revival of the Kondo effect. *Physics World*, **14**(1):33–38, 2001.
- [24] O. Újsághy, J. Kroha, L. Szunyogh, and A. Zawadowski. Theory of the Fano Resonance in the STM Tunneling Density of States due to a Single Kondo Impurity. *Phys. Rev. Lett.*, **85**(12):2557, 2000.
- [25] Jesper Nygård, David Henry Cobden, and Poul Erik Lindelof. Kondo physics in carbon nanotubes. *Nature*, **408**:342–346, 2000.
- [26] Jiwoong Park, Abhay N. Pasupathy, Jonas I. Goldsmith, Connie Chang, Yuval Yaish, Jason R. Petta, Marie Rinkoski, James P. Sethna, Héctor D. Abruña, Paul L. McEuen, and Daniel C. Ralph. Coulomb blockade and the Kondo effect in single-atom transistors. *Nature*, **417**:722–725, 2002.
- [27] Wenjie Liang, Matthew P. Shores, Marc Bockrath, Jeffrey R. Long, and Hongkun Park. Kondo resonance in a single-molecule transistor. *Nature*, **417**:725–729, 2002.

- 
- [28] Lam H. Yu and Douglas Natelson. The Kondo Effect in  $C_{60}$  Single-Molecule Transistors. *Nano Lett.*, **4**(1):79–83, 2004.
- [29] J. J. Parks, A. R. Champagne, G. R. Hutchison, S. Flores-Torres, H. D. Abruña, and D. C. Ralph. Tuning the Kondo effect with a Mechanically Controllable Break Junction. *Phys. Rev. Lett.*, **99**(2):026601, 2007.
- [30] J. J. Parks, A. R. Champagne, T. A. Costi, W. W. Shum, A. N. Pasupathy, E. Neuscamman, S. Flores-Torres, P. S. Cornaglia, A. A. Aligia, C. A. Balseiro, G. K.-L. Chan, H. D. Abruña, and D. C. Ralph. Mechanical Control of Spin States in Spin-1 Molecules and the Underscreened Kondo Effect. *Science*, **328**(5984):1370, 2010.
- [31] M. Pustilnik and L. I. Glazman. Kondo Effect in Real Quantum Dots. *Phys. Rev. Lett.*, **87**(21):216601, 2001.
- [32] K. Nagaoka, T. Jamneala, M. Grobis, and M. F. Crommie. Temperature Dependence of a Single Kondo Impurity. *Phys. Rev. Lett.*, **88**(7):077205, 2002.
- [33] Markus Ternes, Andreas J Heinrich, and Wolf-Dieter Schneider. Spectroscopic manifestations of the Kondo effect on single adatoms. *J. Phys.: Condens. Matter*, **21**(5):053001, 2009.
- [34] T. A. Costi. Kondo Effect in a Magnetic Field and the Magnetoresistivity of Kondo Alloys. *Phys. Rev. Lett.*, **85**(7):1504–1507, 2000.
- [35] Joel A. Appelbaum. Exchange Model of Zero-Bias Tunneling Anomalies. *Phys. Rev.*, **154**(3):633–643, 1967.
- [36] S. Doniach. The kondo lattice and weak antiferromagnetism. *Phys. B*, **91**:231–234, 1977.
- [37] J. Martinek, M. Sindel, L. Borda, J. Barnaś, J. König, G. Schön, and J. von Delft. Kondo Effect in the Presence of Itinerant-Electron Ferromagnetism Studied with the Numerical Renormalization Group Method. *Phys. Rev. Lett.*, **91**(24):247202, 2003.
- [38] J. R. Hauptmann, J. Paaske, and P. E. Lindelof. Electric-field-controlled spin reversal in a quantum dot with ferromagnetic contacts. *Nature Physics*, **4**:373–376, 2008.
- [39] J. Martinek, Y. Utsumi, H. Imamura, J. Barnaś, S. Maekawa, J. König, and G. Schön. Kondo Effect in Quantum Dots Coupled to Ferromagnetic Leads. *Phys. Rev. Lett.*, **91**(12):127203, 2003.
- [40] Mahn-Soo Choi, David Sánchez, and Rosa López. Kondo Effect in a Quantum Dot Coupled to Ferromagnetic Leads: A Numerical Renormalization Group Analysis. *Phys. Rev. Lett.*, **92**(5):056601, 2004.
- [41] M. A. Ruderman and C. Kittel. Indirect Exchange Coupling of Nuclear Magnetic Moments by Conduction Electrons. *Phys. Rev.*, **96**(1):99–102, 1954.
- [42] Tadao Kasuya. A Theory of Metallic Ferro- and Antiferromagnetism on Zener’s Model. *Prog. Theor. Phys.*, **16**(1):45–57, 1956.

- [43] Kei Yosida. Magnetic Properties of Cu-Mn Alloys. *Phys. Rev.*, **106**(5):893–898, 1957.
- [44] Neil W. Ashcroft and N. David Mermin. *Solid State Physics*. Saunders College, Cengage Learning, 1976.
- [45] A.C. Hewson. *The Kondo problem to heavy fermions*. Cambridge University Press, Cambridge, 1993.
- [46] H. R. Krishna-murthy, J. W. Wilkins, and K. G. Wilson. Renormalization-group approach to the Anderson model of dilute magnetic alloys. i. static properties for the symmetric case. *Phys. Rev. B*, **21**(3):1003–1043, 1980.
- [47] C. Jayaprakash, H. R. Krishna-murthy, and J. W. Wilkins. Two-Impurity Kondo Problem. *Phys. Rev. Lett.*, **47**(10):737–740, 1981.
- [48] B. A. Jones and C. M. Varma. Study of two magnetic impurities in a Fermi gas. *Phys. Rev. Lett.*, **58**(9):843–846, 1987.
- [49] B. A. Jones and C. M. Varma. Critical point in the solution of the two magnetic impurity problem. *Phys. Rev. B*, **40**(1):324–329, 1989.
- [50] Ian Affleck and Andreas W. W. Ludwig. Exact critical theory of the two-impurity Kondo model. *Phys. Rev. Lett.*, **68**(7):1046–1049, 1992.
- [51] Ian Affleck, Andreas W. W. Ludwig, and Barbara A. Jones. Conformal-field-theory approach to the two-impurity Kondo problem: Comparison with numerical renormalization-group results. *Phys. Rev. B*, **52**(13):9528–9546, 1995.
- [52] H. Jeong, A. M. Chang, and M. R. Melloch. The Kondo Effect in an Artificial Quantum Dot Molecule. *Science*, **293**(5538):2221–2223, 2001.
- [53] J. C. Chen, A. M. Chang, and M. R. Melloch. Transition between Quantum States in a Parallel-Coupled Double Quantum Dot. *Phys. Rev. Lett.*, **92**(17):176801, 2004.
- [54] N. J. Craig, J. M. Taylor, E. A. Lester, C. M. Marcus, M. P. Hanson, and A. C. Gossard. Tunable Nonlocal Spin Control in a Coupled-Quantum Dot System. *Science*, **304**(5670):565–567, 2004.
- [55] Pascal Simon, Rosa López, and Yuval Oreg. Ruderman-Kittel-Kasuya-Yosida and Magnetic-Field Interactions in Coupled Kondo Quantum Dots. *Phys. Rev. Lett.*, **94**(8):086602, 2005.
- [56] Lorenzo De Leo and Michele Fabrizio. Spectral properties of a two-orbital Anderson impurity model across anon-Fermi-liquid fixed point. *Phys. Rev. B*, **69**(24):245114, 2004.
- [57] Eran Sela and Ian Affleck. Nonequilibrium Transport through Double Quantum Dots: Exact Results near a Quantum Critical Point. *Phys. Rev. Lett.*, **102**(4):047201, 2009.
- [58] Eran Sela and Ian Affleck. Nonequilibrium critical behavior for electron tunneling through quantum dots in an aharonov-bohm circuit. *Phys. Rev. B*, **79**(12):125110, 2009.
- [59] C. J. Chen. *Introduction to Scanning Tunneling Microscopy*. Oxford University Press, Oxford, 1993.

- 
- [60] L. Limot, J. Kröger, R. Berndt, A. Garcia-Lekue, and W. A. Hofer. Atom transfer and single-adatom contacts. *Phys. Rev. Lett.*, **94**(12):126102, 2005.
- [61] G. Binnig, H. Rohrer, Ch. Gerber, and E. Weibel. Tunneling through a controllable vacuum gap. *Appl. Phys. Lett.*, **40**(2):178, 1982.
- [62] G. Binnig, H. Rohrer, Ch. Gerber, and E. Weibel. Surface Studies by Scanning Tunneling Microscopy. *Phys. Rev. Lett.*, **49**(1):57–61, 1982.
- [63] G. Binnig, H. Rohrer, Ch. Gerber, and E. Weibel.  $7 \times 7$  Reconstruction on Si(111) Resolved in Real Space. *Phys. Rev. Lett.*, **50**(2):120, 1983.
- [64] J. Bardeen. Tunnelling from a Many-Particle Point of View. *Phys. Rev. Lett.*, **6**(2):57–59, 1961.
- [65] Joel A. Appelbaum and W. F. Brinkman. Theory of Many-Body Effects in Tunneling. *Physical Review*, **186**(2):464–470, 1969.
- [66] J. Tersoff and D. R. Hamann. Theory and Application for the Scanning Tunneling Microscope. *Phys. Rev. Lett.*, **50**(25):1998, 1983.
- [67] J. Tersoff and D. R. Hamann. Theory of the scanning tunneling microscope. *Phys. Rev. B*, **31**(2):805, 1985.
- [68] Roland Wiesendanger. *Scanning Probe Microscopy and Spectroscopy: Methods and Applications*. Cambridge University Press, Cambridge, 1994.
- [69] Vladimir A. Ukraintsev. Data evaluation technique for electron-tunneling spectroscopy. *Phys. Rev. B*, **53**(16):11176, 1996.
- [70] C. Iacovita. *Spin-dependent tunneling into single cobalt-phthalocyanine molecules*. PhD thesis, Université de Strasbourg, 2009.
- [71] M. E. Taylor. Dynamics of piezoelectric tube scanners for scanning probe microscopy. *Rev. Sci. Instrum.*, **64**(1):154–158, 1993.
- [72] Benjamin W. Heinrich, Cristian Iacovita, Thomas Brumme, Deung-Jang Choi, Laurent Limot, Mircea V. Rastei, Werner A. Hofer, Jens Kortus, and Jean-Pierre Bucher. Direct Observation of the Tunneling Channels of a Chemisorbed Molecule. *J. Phys. Chem. Lett.*, **1**(10):1517–1523, 2010.
- [73] J. Kröger, L. Limot, H. Jensen, R. Berndt, S. Crampin, and E. Pehlke. Surface state electron dynamics of clean and adsorbate-covered metal surfaces studied with the scanning tunnelling microscope. *Progress in Surface Science*, **80**(1-2):26–48, 2005.
- [74] J. A. Stroscio and R. M. Feenstra. *Scanning Tunneling Microscopy*, volume 27. Academic, New York, 1993.
- [75] M. Ziegler, N. Néel, A. Sperl, J. Kröger, and R. Berndt. Local density of states from constant-current tunneling spectra. *Phys. Rev. B*, **80**(12):125402, 2009.
- [76] Nikolaus Knorr, M. Alexander Schneider, Lars Diekhöner, Peter Wahl, and Klaus Kern. Kondo

- Effect of Single Co Adatoms on Cu Surfaces. *Phys. Rev. Lett.*, **88**(9):096804, 2002.
- [77] A. Gumbsch, G. Barcaro, M. G. Ramsey, S. Surnev, A. Fortunelli, and F. P. Netzer. Kondo effect of cobalt adatoms on nanostructured Cu-O surfaces: Scanning tunneling spectroscopy experiments and first-principles calculations. *Phys. Rev. B*, **81**(16):165420, 2010.
- [78] P. Wahl, L. Diekhöner, M. A. Schneider, L. Vitali, G. Wittich, and K. Kern. Kondo Temperature of Magnetic Impurities at Surfaces. *Phys. Rev. Lett.*, **93**(17):176603, 2004.
- [79] J. Merino and O. Gunnarsson. Simple model for scanning tunneling spectroscopy of noble metal surfaces with adsorbed Kondo impurities. *Phys. Rev. B*, **69**(11):115404, 2004.
- [80] Chiung-Yuan Lin, A. H. Castro Neto, and B. A. Jones. Microscopic theory of the single impurity surface Kondo resonance. *Phys. Rev. B*, **71**(3):035417, 2005.
- [81] Gianfranco Pacchionia, Markus Mayerb, Sven Krügerb, and Notker Rösch. Bonding and adsorbate core level shifts of transition metal atoms on the Al(100) surface from density functional calculations. *Chem. Phys. Lett.*, **299**(2):137–144, 1999.
- [82] José A. Rodriguez. Metal-metal bonding on surfaces: molecular orbital study of Pd/Ti(001) and Pd/Ru(001). *Surf. Sci.*, **303**(3):366–376, 1994.
- [83] M. C. Desjonqueres. A simple chemisorption theory and its application to transition adatoms on transition metals. *J. Phys. C: Solid State Phys.*, **15**(18):4007, 1982.
- [84] U. Fano. Effects of Configuration Interaction on Intensities and Phase Shifts. *Phys. Rev.*, **124**(6):1866–1878, 1961.
- [85] V. Madhavan, W. Chen, T. Jamneala, M. F. Crommie, and Ned S. Wingreen. Local spectroscopy of a Kondo impurity: Co on Au(111). *Phys. Rev. B*, **64**(16):165412, 2001.
- [86] M. Plihal and J. W. Gadzuk. Nonequilibrium theory of scanning tunneling spectroscopy via adsorbate resonances: Nonmagnetic and Kondo impurities. *Phys. Rev. B*, **63**(8):085404, 2001.
- [87] D. M. Eigler and E. K. Schweizer. Positioning single atoms with a scanning tunnelling microscope. *Nature*, **344**:524–526, 1990.
- [88] P. Wahl, P. Simon, L. Diekhöner, V. S. Stepanyuk, P. Bruno, M. A. Schneider, and K. Kern. Exchange Interaction between Single Magnetic Adatoms. *Phys. Rev. Lett.*, **98**(5):056601, 2007.
- [89] N. Néel, R. Berndt, J. Kröger, T. O. Wehling, A. I. Lichtenstein, and M. I. Katsnelson. Two-Site Kondo Effect in Atomic Chains. *Phys. Rev. Lett.*, **107**(10):106804, 2011.
- [90] Jakob Bork, Yong hui Zhang, Lars Diekhöner, László Borda, Pascal Simon, Johann Kroha, Peter Wahl, and Klaus Kern. A tunable two-impurity Kondo system in an atomic point contact. *Nature Physics*, **7**:901–906, 2011.
- [91] N. Agraït, J. G. Rodrigo, and S. Vieira. Conductance steps and quantization in atomic-size contacts. *Phys. Rev. B*, **47**(18):12345, 1993.
- [92] J. C. Maxwell. *A Treatise on Electricity and Magnetism*. Dover Publication, New York, 1954.

- 
- [93] Yu. V. Sharvin. A Possible Method for Studying Fermi Surfaces. *Soviet Physics JETP*, **21**:655, 1965.
  - [94] J. Kröger, N. Néel, and L. Limot. Contact to single atoms and molecules with the tip of a scanning tunnelling microscope. *J. Phys.: Condens. Matter*, **20**(22):223001, 2008.
  - [95] R. Landauer. Spatial Variation of Currents and Fields Due to Localized Scatterers in Metallic Conduction. *IBM J. Res. Dev.*, **1**(3):223–231, 1957.
  - [96] S. Datta. *Electronic Transport in Mesoscopic Systems*. Cambridge University Press, Cambridge, 1995.
  - [97] M. Büttiker. Coherent and sequential tunneling in series barriers. *IBM J. Res. Dev.*, **32**(1):63, 1988.
  - [98] R. Landauer. Electrical resistance of disordered one-dimensional lattices. *Philos. Mag.*, **21**(172):863–867, 1970.
  - [99] R. Landauer. Can a length of perfect conductor have a resistance? *Phys. Lett. A*, **85**(2):91–93, 1981.
  - [100] M. Büttiker, Y. Imry, R. Landauer, and S. Pinhas. Generalized many-channel conductance formula with application to small rings. *Phys. Rev. B*, **31**(10):6207, 1985.
  - [101] M. Brandbyge and K. W. Jacobsen. *Proceedings of the NATO Advanced Research Workshop on Nanowires*. NATO Advanced Studies Institute, Series E: Applied Sciences. 1997.
  - [102] E. N. Bogachev, A. N. Zagorin, and I. O. Kulik. Conductance jumps and magnetic flux quantization in ballistic point contacts. *Sov. J. Low. Temp. Phys.*, **16**:796, 1990.
  - [103] J. A. Torres, J. L. Pascual, and J. J. Sáenz. Theory of conduction through narrow constrictions in a three-dimensional electron gas. *Phys. Rev. B*, **49**(23):16581, 1994.
  - [104] M. Brandbyge, J. Schiøtz, M. R. Sørensen, P. Stoltze, K. W. Jacobsen, J. K. Nørskov, L. Olesen, E. Lægsgaard, I. Stensgaard, and F. Besenbacher. Quantized conductance in atom-sized wires between two metals. *Phys. Rev. B*, **52**(11):8499, 1995.
  - [105] M. Brandbyge, K. W. Jacobsen, and J. K. Nørskov. Scattering and conductance quantization in three-dimensional metal nanocontacts. *Phys. Rev. B*, **55**(4):2637, 1997.
  - [106] J. I. Pascual, J. Méndez, J. Gómez-Herrero, A. M. Baró, N. García, and V. Thien Binh. Quantum contact in gold nanostructures by scanning tunneling microscopy. *Phys. Rev. Lett.*, **71**(12):1852, 1993.
  - [107] L. Olesen, E. Lægsgaard, I. Stensgaard, F. Besenbacher, J. Schiøtz, P. Stoltze, K. W. Jacobsen, and J. K. Nørskov. Quantized conductance in an atom-sized point contact. *Phys. Rev. Lett.*, **72**(14):2251, 1994.
  - [108] Z. Gai, Y. He, H. Yu, and W. S. Yang. Observation of conductance quantization of ballistic metallic point contacts at room temperature. *Phys. Rev. B*, **53**(3):1042, 1996.

- [109] N. Néel, J. Kröger, L. Limot, K. Palotas, W. A. Hofer, and R. Berndt. Conductance and Kondo effect in a controlled single-atom contact. *Phys. Rev. Lett*, **98**(1):016801, 2007.
- [110] N. Néel, J. Kröger, L. Limot, T. Frederiksen, M. Brandbyge, and R. Berndt. Controlled contact to a  $C_{60}$  molecule. *Phys. Rev. Lett.*, **98**(6):065502, 2007.
- [111] J. Kröger, H. Jensen, and R. Berndt. Conductance of tip-surface and tip-atom junction on Au(111) explored by a scanning tunnelling microscope. *New J. Phys.*, **9**(5):153, 2007.
- [112] N. Néel, J. Kröger, L. Limot, and R. Berndt. Conductance of single atoms and molecules studied with a scanning tunnelling microscope. *Nanotechnol.*, **18**(4):044027, 2007.
- [113] H. Jensen, J. Kröger, N. Néel, and R. Berndt. Silver oligomer and single fullerene electronic properties revealed by a scanning tunnelling microscope. *Eur. Phys. J. D*, **45**(3):465–469, 2007.
- [114] N. Néel, L. Limot, J. Kröger, and R. Berndt. Rotation of  $C_{60}$  in a single-molecule contact. *Phys. Rev. B*, **77**(12):125431, 2008.
- [115] N. Néel, J. Kröger, L. Limot, and R. Berndt. Conductance of oriented  $C_{60}$  molecules. *Nano Lett.*, **8**(5):1291, 2008.
- [116] J. Kröger. Nonadiabatic effects on surfaces: Kohn anomaly, electronic damping of adsorbate vibrations, and local heating of single molecules. *J. Phys.: Condens. Matter*, **20**(22):224015, 2008.
- [117] A. Yazdani, D. M. Eigler, and N. D. Lang. Off-resonance conduction through atomic wires. *Science*, **272**(5270):1921, 1996.
- [118] N. Néel, J. Kröger, and R. Berndt. Quantized Conductance of a Single Magnetic Atom. *Phys. Rev. Lett.*, **102**(8):086805, 2009.
- [119] Néel N., J. Kröger, and R. Berndt. Kondo effect of a Co atom on Cu(111) in contact with an iron tip. *Phys. Rev. B*, **82**(23):233401, 2010.
- [120] J. G. Simmons. Generalized formula for the electric tunnel effect between similar electrodes separated by a thin insulating film. *J. Appl. Phys.*, **34**(6):1793, 1963.
- [121] W. A. Hofer, A. Garcia-Lekue, and H. Brune. The role of surface elasticity in giant corrugations observed by scanning tunneling microscopes. *Chem. Phys. Lett.*, **397**(4-6):354, 2004.
- [122] C. Untiedt, M. J. Caturla, M. R. Calvo, J. J. Palacios, R. C. Segers, and J. M. van Ruitenbeek. Formation of a Metallic Contact: Jump to Contact Revisited. *Phys. Rev. Lett.*, **98**(20):206801, 2007.
- [123] J. K. Gimzewski and R. Möller. Transition from the tunneling regime to point contact studied using scanning tunneling microscopy. *Phys. Rev. B*, **36**(2):1284, 1987.
- [124] U. Dürig, O. Züger, and D. W. Pohl. Observation of metallic adhesion using the scanning tunneling microscope. *Phys. Rev. Lett.*, **65**(3):349, 1990.
- [125] S. Ciraci and E. Tekman. Theory of transition from the tunneling regime to point contact in

- scanning tunneling microscopy. *Phys. Rev. B*, **40**(17):11969, 1989.
- [126] Markus Ternes, César González, Christopher P. Lutz, Prokop Hapala, Franz J. Giessibl, Pavel Jelínek, and Andreas J. Heinrich. Interplay of Conductance, Force, and Structural Change in Metallic Point Contacts. *Phys. Rev. Lett.*, **106**(1):016802, 2011.
  - [127] L. Olesen, M. Brandbyge, M. R. Sørensen, K. W. Jacobsen, E. Lægsgaard, I. Stensgaard, and F. Besenbacher. Apparent Barrier Height in Scanning Tunneling Microscopy Revisited. *Phys. Rev. Lett.*, **76**(9):1485, 1996.
  - [128] N. D. Lang. Apparent barrier height in scanning tunneling microscopy. *Phys. Rev. B*, **37**(17):10395, 1988.
  - [129] J. Ferrer, A. Martín-Rodero, and F. Flores. Contact resistance in the scanning tunneling microscope at very small distances. *Phys. Rev. B*, **38**(14):10113, 1988.
  - [130] Jose Manuel Blanco, Cesar González, Pavel Jelínek, José Ortega, Fernando Flores, and Rubén Pérez. First-principles simulations of STM images: From tunneling to the contact regime. *Phys. Rev. B*, **70**(8):085405, 2004.
  - [131] M. V. Rastei, B. Heinrich, L. Limot, P. A. Ignatiev, V. S. Stepanyuk, P. Bruno, and J. P. Bucher. Size-Dependent Surface States of Strained Cobalt Nanoislands on Cu(111). *Phys. Rev. Lett.*, **99**(24):246102, 2007.
  - [132] A. Schirmeisen, G. Cross, A. Stalder, P. Grutter, and U. Durig. Metallic adhesion and tunnelling at the atomic scale. *New J. Phys.*, **2**(1):29, 2000.
  - [133] G. Rubio-Bollinger, P. Joyez, and N. Agrait. Metallic adhesion in atomic-size junctions. *Phys. Rev. Lett.*, **93**(11):116803, 2004.
  - [134] Y. Sun, H. Mortensen, S. Schär, A.-S. Lucier, Y. Miyahara, P. Grütter, and W. Hofer. From tunneling to point contact: Correlation between forces and current. *Phys. Rev. B*, **71**(19):193407, 2005.
  - [135] Markus Ternes, Christopher P. Lutz, Cyrus F. Hirjibehedin, Franz J. Giessibl, and Andreas J. Heinrich. The Force Needed to Move an Atom on a Surface. *Science*, **319**(5866):1066, 2008.
  - [136] Daisuke Sawada, Yoshiaki Sugimoto, Ken ichi Morita, Masayuki Abe, and Seizo Morita. Simultaneous measurement of force and tunneling current at room temperature. *Appl. Phys. Lett.*, **94**(17):173117, 2009.
  - [137] L. Limot, T. Maroutian, P. Johansson, and R. Berndt. Surface-State Stark Shift in a Scanning Tunneling Microscope. *Phys. Rev. Lett.*, **91**(19):196801, 2003.
  - [138] J. Kröger, L. Limot, H. Jensen, and R. Berndt. Stark effect in Au(111) and Cu(111) surface states. *Phys. Rev. B*, **70**(3):033401, 2004.
  - [139] S. Ciraci and E. Tekman. Relationship between strain and the surface electronic structure of Cu(111) films on Ru(0001): Theory and experiment. *Phys. Rev. B*, **71**(12):125412, 2005.



- [140] N. Quaas, M. Wenderoth, A. Weismann, and R. G. Ulbrich. Kondo resonance of single Co atoms embedded in Cu(111). *Phys. Rev. B*, **69**(20):201103, 2004.
- [141] N. Néel, J. Kröger, R. Berndt, T. O. Wehling, A. I. Lichtenstein, and M. I. Katsnelson. Controlling the Kondo effect in  $\text{CoCu}_n$  clusters atom by atom. *Phys. Rev. Lett.*, **101**(26):266803, 2008.
- [142] I. K. Yanson, V. V. Fisun, R. Hesper, A. V. Khotkevich, J. M. Krans, J. A. Mydosh, and J. M. van Ruitenbeek. Size Dependence of Kondo Scattering in Point Contacts. *Phys. Rev. Lett.*, **74**(2):302, 1995.
- [143] Lucia Vitali, Robin Ohmann, Sebastian Stepanow, Pietro Gambardella, Kun Tao, Renzhong Huang, Valeri S. Stepanyuk, Patrick Bruno, and Klaus Kern. Kondo Effect in Single Atom Contacts: The Importance of the Atomic Geometry. *Phys. Rev. Lett.*, **101**(21):216802, 2008.
- [144] Procolo Lucignano, Riccardo Mazzarello, Alexander Smogunov, Michele Fabrizio, and Erio Tosatti. Kondo conductance in an atomic nanocontact from first principles. *Nat. Mater.*, **8**:563, 2009.
- [145] D. Jacob, K. Haule, and G. Kotliar. Kondo Effect and Conductance of Nanocontacts with Magnetic Impurities. *Phys. Rev. Lett.*, **103**(1):016803, 2009.
- [146] H. O. Frota. Shape of the Kondo resonance. *Phys. Rev. B*, **45**(3):1096, 1992.
- [147] Henning Prüser, Martin Wenderoth, Piet E. Dargel, Alexander Weismann, Robert Peters, Thomas Pruschke, and Rainer G. Ulbrich. Long-range Kondo signature of a single magnetic impurity. *Nature Physics*, **7**:203–206, 2011.
- [148] R. Z. Huang, V. S. Stepanyuk, A. L. Klavsyuk, W. Hergert, P. Bruno, and J. Kirschner. Atomic relaxations and magnetic states in a single-atom tunneling junction. *Phys. Rev. B*, **73**(15):153404, 2006.
- [149] Rossitza Pentcheva and Matthias Scheffler. Initial adsorption of Co on Cu(001): A first-principles investigation. *Phys. Rev. B*, **65**(15):155418, 2002.
- [150] L. I. Glazman and M. E. Raikh. Nonmagnetic spin-polaron in a generalized Hubbard model for  $\text{CuO}_2$  planes. *JETP Lett.*, **47**:452, 1988.
- [151] Tai Kai Ng and Patrick A. Lee. On-Site Coulomb Repulsion and Resonant Tunneling. *Phys. Rev. Lett.*, **61**(15):1768, 1988.
- [152] P. Wahl, A. P. Seitsonen, L. Diekhöner, M. A. Schneider, and K Kern. Kondo-effect of substitutional cobalt impurities at copper surfaces. *New J. Phys.*, **11**:113015, 2009.
- [153] V. Zlatić, B. Horvatić, and D. Šokčević. Density of states for intermediate valence and Kondo systems. *Phys. B*, **59**(2):151, 1985.
- [154] M.-C. Desjonqueres and D. Spanjaard. *Concepts in Surface Physics*. Springer, Berlin, 1993.
- [155] P. W. Anderson, E. Abrahams, and T. V. Ramakrishnan. Possible Explanation of Nonlinear

- 
- Conductivity in Thin-Film Metal Wires. *Phys. Rev. Lett.*, **43**(10):718–720, 1979.
- [156] M. L. Roukes, M. R. Freeman, R. S. Germain, R. C. Richardson, and M. B. Ketchen. Hot electrons and energy transport in metals at millikelvin temperatures. *Phys. Rev. Lett.*, **55**(4):422–425, 1985.
  - [157] J. F. DiTusa, M. Park M. S. Isaacson K. Lin, and J. M. Parpia. Role of phonon dimensionality on electron-phonon scattering rates. *Phys. Rev. Lett.*, **68**(8):1156–1159, 1992.
  - [158] M. Büttiker, Y. Imry, R. Landauer, and S. Pinhas. Inelastic Lifetimes of Hot Electrons in Real Metals. *Phys. Rev. Lett.*, **83**(11):2230–2233, 1999.
  - [159] A. Sperl, J. Kröger, and R. Berndt. Direct observation of conductance fluctuations of a single-atom tunneling contact. *Phys. Rev. B*, **81**(3):035406, 2010.
  - [160] M Tsutsui, S Kurokawa, and A Sakai. Bias-induced local heating in au atom-sized contacts. *Nanotechnology*, **17**(21):5334, 2006.
  - [161] K. S. Ralls, D. C. Ralph, and R. A. Buhrman. Individual-defect electromigration in metal nanobridges. *Phys. Rev. B*, **40**(17):11561, 1989.
  - [162] P. A. M. Holweg, J. Caro, A. H. Verbruggen, and S. Radelaar. Ballistic electron transport and two-level resistance fluctuations in noble-metal nanobridges. *Phys. Rev. B*, **45**(16):9311, 1992.
  - [163] Ragnar Holm. *Electric Contacts : Theory and Application*. Springer, Berlin, 1967.
  - [164] T. N. Todorov, J. Hoekstra, and A. P. Sutton. Current-induced embrittlement of atomic wires. *Phys. Rev. Lett.*, **86**(16):3606, 2001.
  - [165] Yu-Chang Chen, Michael Zwolak, and Massimiliano Di Ventra. Local Heating in Nanoscale Conductors. *Nano Lett.*, **3**(12):1691, 2003.
  - [166] Bailey C. Hsu, Yu-Shen Liu, Sheng Hsien Lin, and Yu-Chang Chen. Seebeck coefficients in nanoscale junctions: Effects of electron-vibration scattering and local heating. *Phys. Rev. B*, **83**(4):041404(R), 2011.
  - [167] Ralf Bulla, Matthew T. Glossop, David E. Logan, and Thomas Pruschke. The soft-gap Anderson model: comparison of renormalization group and local moment approaches. *J. Phys.: Condens. Matter*, **12**(23):4899, 2000.
  - [168] Rok Žitko and Thomas Pruschke. Energy resolution and discretization artifacts in the numerical renormalization group. *Phys. Rev. B*, **79**(8):085106, 2009.
  - [169] H. O. Frota and L. N. Oliveira. Photoemission spectroscopy for the spin-degenerate Anderson model. *Phys. Rev. B*, **33**(11):7871, 1986.
  - [170] Rok Žitko. Kondo resonance lineshape of magnetic adatoms on decoupling layers. *Phys. Rev. B*, **84**(19):195116, 2011.
  - [171] R. Meservey, P. M. Tedrow, and P. Fulde. Magnetic Field Splitting of the Quasiparticle States in Superconducting Aluminum Films. *Phys. Rev. Lett.*, **25**(18):1270–1272, 1970.

- [172] P. M. Tedrow and R. Meservey. Spin-Dependent Tunneling into Ferromagnetic Nickel. *Phys. Rev. Lett.*, **26**(4):192–195, 1999.
- [173] M. Julliere. Tunneling between ferromagnetic films. *Phys. Lett. A*, **54**(3):225–226, 1975.
- [174] J. S. Moodera, Lisa R. Kinder, Terrilyn M. Wong, and R. Meservey. Large Magnetoresistance at Room Temperature in Ferromagnetic Thin Film Tunnel Junctions. *Phys. Rev. Lett.*, **74**(16):3273–3276, 1995.
- [175] T. Miyazaki and N. Tezuka. Giant magnetic tunneling effect in Fe/Al<sub>2</sub>O<sub>3</sub>/Fe junction. *J. Magn. Magn. Mater.*, **139**(2):L231–L234, 1995.
- [176] M. N. Baibich, J. M. Broto, A. Fert, F. Nguyen Van Dau, F. Petroff, P. Etienne, G. Creuzet, A. Friederich, and J. Chazelas. Giant Magnetoresistance of (001)Fe/(001)Cr Magnetic Superlattices. *Phys. Rev. Lett.*, **61**(21):2472–2475, 1988.
- [177] G. Binasch, P. Grünberg, F. Saurenbach, and W. Zinn. Enhanced magnetoresistance in layered magnetic structures with antiferromagnetic interlayer exchange. *Phys. Rev. B*, **39**(7):4828–4830, 1989.
- [178] B. Dieny, V. S. Speriosu, S. S. P. Parkin, B. A. Gurney, D. R. Wilhoit, and D. Mauri. Giant magnetoresistive in soft ferromagnetic multilayers. *Phys. Rev. B*, **43**(1):1297–1300, 1991.
- [179] R. Meservey and P. M. Tedrow. Spin-polarized electron tunneling. *Phys. Rep.*, **238**(4):173–243, 1994.
- [180] R. J. Soulen Jr., J. M. Byers, M. S. Osofsky, B. Nadgorny, T. Ambrose, S. F. Cheng, P. R. Broussard, C. T. Tanaka, J. Nowak, J. S. Moodera, A. Barry, and J. M. D. Coey. Measuring the Spin Polarization of a Metal with a Superconducting Point Contact. *Science*, **282**(5386):85–88, 1998.
- [181] J. M. D. Coey and S. Sanvito. Magnetic semiconductors and half-metals. *J. Phys. D: Appl. Phys.*, **37**(7):988–993, 2004.
- [182] I. I. Mazin. How to Define and Calculate the Degree of Spin Polarization in Ferromagnets. *Phys. Rev. Lett.*, **83**(7):1427–1430, 1999.
- [183] A. Fert, J.-M. George, H. Jaffres, and G Faini. Spin injection and experimental detection of spin accumulation. *J. Phys. D: Appl. Phys.*, **35**(19):2443–2447, 2002.
- [184] J. F. Gregg, I. Petej, E. Jouguelet, and C. Dennis. Spin electronics-a review. *J. Phys. D: Appl. Phys.*, **35**(18):R121, 2002.
- [185] Jack Bass and William P. Pratt Jr. Spin-diffusion lengths in metals and alloys, and spin-flipping at metal/metal interfaces: an experimentalist's critical review. *J. Phys. D: Cond. Matt.*, **19**(18):183201, 2007.
- [186] T. Valet and A. Fert. Theory of the perpendicular magnetoresistance in magnetic multilayers. *Phys. Rev. B*, **48**(10):7099–7113, 1993.

- 
- [187] D.-J. Choi, M. V. Rastei, P. Simon, and L. Limot. Conductance-driven Change of the Kondo Effect of a Single Cobalt Atom. *Phys. Rev. Lett.*, **108**:xxxxxx, Apr 2012.
  - [188] H. Jeong, A. M. Chang, and M. R. Melloch. The Kondo Effect in an Artificial Quantum Dot Molecule. *Science*, **293**(5538):2221–2223, 2001.
  - [189] J. C. Chen, A. M. Chang, and M. R. Melloch. Transition between Quantum States in a Parallel-Coupled Double Quantum Dot. *Phys. Rev. Lett.*, **92**:176801, 2004.
  - [190] A. F. Otte, M. Ternes, S. Loth, C. P. Lutz, C. F. Hirjibehedin, and A. J. Heinrich. Spin Excitations of a Kondo-Screened Atom Coupled to a Second Magnetic Atom. *Phys. Rev. Lett.*, **103**:107203, 2009.
  - [191] N. J. Craig, J. M. Taylor, E. A. Lester, C. M. Marcus, M. P. Hanson, and A. C. Gossard. Tunable Nonlocal Spin Control in a Coupled-Quantum Dot System. *Science*, **304**(5670):565–567, 2004.
  - [192] Kun Tao, I. Rungger, S. Sanvito, and V. S. Stepanyuk. Quantum conductance of a single magnetic atom: An *ab initio* study. *Phys. Rev. B*, **82**:085412, 2010.
  - [193] Kenneth G. Wilson. The renormalization group: Critical phenomena and the Kondo problem. *Rev. Mod. Phys.*, **47**:773–840, 1975.
  - [194] A. G. Aronov and G. E. Pikus. Spin injection into semiconductors. *Sov. Phys. Semicond.*, **10**:698–700, 1976.
  - [195] Mark Johnson and R. H. Silsbee. Interfacial charge-spin coupling: Injection and detection of spin magnetization in metals. *Phys. Rev. Lett.*, **55**:1790–1793, 1985.
  - [196] P. C. van Son, H. van Kempen, and P. Wyder. Boundary Resistance of the Ferromagnetic-Nonferromagnetic Metal Interface. *Phys. Rev. Lett.*, **58**:2271–2273, 1987.
  - [197] T. Valet and A. Fert. Theory of the perpendicular magnetoresistance in magnetic multilayers. *Phys. Rev. B*, **48**:7099–7113, 1993.
  - [198] Focko Meier, Lihui Zhou, Jens Wiebe, and Roland Wiesendanger. Revealing Magnetic Interactions from Single-Atom Magnetization Curves. *Science*, **320**(5872):82–86, 2008.
  - [199] O. O. Brovko, P. A. Ignatiev, V. S. Stepanyuk, and P. Bruno. Tailoring Exchange Interactions in Engineered Nanostructures: An *Ab Initio* Study. *Phys. Rev. Lett.*, **101**:036809, 2008.
  - [200] P. Bruno and C. Chappert. Oscillatory coupling between ferromagnetic layers separated by a nonmagnetic metal spacer. *Phys. Rev. Lett.*, **67**:1602–1605, 1991.
  - [201] P. Bruno and C. Chappert. Ruderman-Kittel theory of oscillatory interlayer exchange coupling. *Phys. Rev. B*, **46**:261–270, 1992.
  - [202] Takashi Uchihashi, Jianwei Zhang, Jörg Kröger, and Richard Berndt. Quantum modulation of the Kondo resonance of Co adatoms on Cu/Co/Cu(100): Low-temperature scanning tunneling spectroscopy study. *Phys. Rev. B*, **78**:033402, 2008.
  - [203] Ying-Shuang Fu, Qi-Kun Xue, and Roland Wiesendanger. Spin-Resolved Splitting of Kondo

- Resonances in the Presence of RKKY-Type Coupling. *Phys. Rev. Lett.*, **108**:087203, 2012.
- [204] M. Pajda, J. Kudrnovský, I. Turek, V. Drchal, and P. Bruno. *Ab initio* calculations of exchange interactions, spin-wave stiffness constants, and Curie temperatures of Fe, Co, and Ni. *Phys. Rev. B*, **64**:174402, 2001.
- [205] T. Kobayashi, S. Tsuruta, S. Sasaki, T. Fujisawa, Y. Tokura, and T. Akazaki. Kondo Effect in a Semiconductor Quantum Dot with a Spin-Accumulated Lead. *Phys. Rev. Lett.*, **104**:036804, 2010.
- [206] Nicolás Agraita, Alfredo Levy Yeyatib, and Jan M. van Ruitenbeek. Quantum properties of atomic-sized conductors. *Physics Reports*, **377**(2-3):81–279, 2003.
- [207] B. W. Heinrich, C. Iacovita, M. V. Rastei, L. Limot, J. P. Bucher, P. A. Ignatiev, V. S. Stepanyuk, and P. Bruno. Spin structure of an atomic protrusion: Probing single atoms on cobalt nanoislands. *Phys. Rev. B*, **79**(11):1134015, 2009.
- [208] N. Néel, J. Kröger, L. Limot, and R. Berndt. Conductance of single atoms and molecules studied with a scanning tunnelling microscope. *J. Scann. Probe Microsc.*, **3**(4):9, 2008.
- [209] C. Joachim, J. K. Gimzewski, R. R. Schlittler, and C. Chavy. Electronic transparency of a single C<sub>60</sub> molecule. *Phys. Rev. Lett.*, **74**(11):2102, 1995.
- [210] Rui Qiao, Aaron P. Roberts, Andrew S. Mount, Stephen J. Klaine, and Pu Chun Ke. Translocation of C<sub>60</sub> and Its Derivatives Across a Lipid Bilayer. *Nano Lett.*, **7**(3):614–619, 2007.
- [211] G. Schull and R. Berndt. Orientationally ordered (7 × 7) superstructure of C<sub>60</sub> on Au(111). *Phys. Rev. Lett.*, **99**(22):226105, 2007.
- [212] Eric I. Altman and Richard J. Colton. Determination of the orientation of C<sub>60</sub> adsorbed on Au(111) and Ag(111). *Phys. Rev. B*, **48**(24):18244–18249, 1993.
- [213] Tomihiro Hashizume, K. Motai, X. D. Wang, H. Shinohara, Y. Saito, Y. Maruyama, K. Ohno, Y. Kawazoe, Y. Nishina, H. W. Pickering, Y. Kuk, and T. Sakurai. Intramolecular structures of C<sub>60</sub> molecules adsorbed on the Cu(111)-(1 × 1) surface. *Phys. Rev. Lett.*, **71**(18):2959–2962, 1993.
- [214] M. Abel, A. Dmitriev, R. Fasel, N. Liu, J. V. Barth, and K. Kern. Scanning tunneling microscopy and X-ray photoelectron diffraction investigation of C<sub>60</sub> films on Cu(100). *Phys. Rev. B*, **67**(24):245407, 2003.
- [215] Guillaume Schull, Thomas Frederiksen, Mads Brandbyge, and Richard Berndt. Passing Current through Touching Molecules. *Phys. Rev. Lett.*, **103**(20):206803, 2009.
- [216] Guillaume Schull, Thomas Frederiksen, Andres Arnau, Daniel Sanchez-Portal, and Richard Berndt. Atomic-scale engineering of electrodes for single-molecule contacts. *Nature Nanotech.*, **6**(1):23–27, 2011.
- [217] J. Chen, M. A. Reed, A. M. Rawlett, and J. M. Tour. Large On-Off Ratios and Negative

- Differential Resistance in a Molecular Electronic Device. *Science*, **286**(5444):1550, 1999.
- [218] J. Gaudioso, L. J. Lauhon, and W. Ho. Vibrationally Mediated Negative Differential Resistance in a Single Molecule. *Phys. Rev. Lett.*, **85**(9):1918, 2000.
- [219] N. J. Tao. Electron transport in molecular junctions. *Nat. Nanotech.*, **1**:173–181, 2006.
- [220] L. Esaki. New Phenomenon in Narrow Germanium p-n Junctions. *Phys. Rev.*, **109**(2):603, 1958.
- [221] I.-W. Lyo and P. Avouris. Negative Differential Resistance on the Atomic Scale: Implications for Atomic Scale Devices. *Science*, **245**(4924):1369, 1989.
- [222] P. Bedrossian, D. M. Chen, K. Mortensen, and J. A. Golovchenko. Demonstration of the tunnel-diode effect on an atomic scale. *Nature*, **342**:258, 1989.
- [223] L. Chang, E. Mendez, and C. Tejedor. *Resonant Tunneling in Semiconductors: physics and applications*. Plenum Press, New York, 1991.
- [224] Yongqiang Xue, Supriyo Datta, Seunghun Hong, R. Reifenberger, Jason I. Henderson, and Clifford P. Kubiak. Negative differential resistance in the scanning-tunneling spectroscopy of organic molecules. *Phys. Rev. B*, **59**(12):R7852–R7855, 1999.
- [225] Nathan P. Guisinger, Mark E. Greene, Rajiv Basu, Andrew S. Baluch, and Mark C. Hersam. Room Temperature Negative Differential Resistance through Individual Organic Molecules on Silicon Surfaces. *Nano Lett.*, **4**(1):55–59, 2004.
- [226] Lan Chen, Zhenpeng Hu, Aidi Zhao, Bing Wang, Yi Luo, Jinlong Yang, and J. G. Hou. Mechanism for Negative Differential Resistance in Molecular Electronic Devices: Local Orbital Symmetry Matching. *Phys. Rev. Lett.*, **99**(14):146803, 2007.
- [227] Changgan Zeng, Haiqian Wang, Bing Wang, Jinlong Yang, and J. G. Hou. Negative differential-resistance device involving two C<sub>60</sub> molecules. *Appl. Phys. Lett.*, **77**(22):3595, 2000.
- [228] K. J. Franke, G. Schulze, N. Henningsen, I. Fernández-Torrente, J. I. Pascual, S. Zarwell, K. Rück-Braun, M. Cobian, and N. Lorente. Reducing the Molecule-Substrate Coupling in C<sub>60</sub>-Based Nanostructures by Molecular Interactions. *Phys. Rev. Lett.*, **100**(3):036807, 2008.
- [229] M. Grobis, A. Wachowiak, R. Yamachika, and M. F. Crommie. Tuning negative differential resistance in a molecular film. *Appl. Phys. Lett.*, **86**(20):204102, 2005.
- [230] Frederico D. Novaes, Manuel Cobian, Alberto Garcia, Pablo Ordejon, Hiromu Ueba, and Nicolas Lorente. Negative differential resistance in scanning tunneling microscopy: simulations on C<sub>60</sub>-based molecular overlayers. *arXiv:1101.3714v1*, 2011.
- [231] S. D. Kevan and R. H. Gaylord. High-resolution photoemission study of the electronic structure of the noble-metal (111) surfaces. *Phys. Rev. B*, **36**(11):5809, 1987.
- [232] Xinghua Lu, M. Grobis, K. H. Khoo, Steven G. Louie, and M. F. Crommie. Spatially Mapping the Spectral Density of a Single C<sub>60</sub> Molecule. *Phys. Rev. Lett.*, **90**(9):096802, 2003.

- [233] C. Silien, N. A. Pradhan, W. Ho, and P. A. Thiry. Influence of adsorbate-substrate interaction on the local electronic structure of  $C_{60}$  studied by low-temperature STM. *Phys. Rev. Lett.*, **69**(11):115434, 2004.
- [234] Woei Wu Pai, H. T. Jeng, C.-M. Cheng, C.-H. Lin, Xudong Xiao, Aidi Zhao, Xieqiu Zhang, Geng Xu, X. Q. Shi, M. A. Van Hove, C.-S. Hsue, and K.-D. Tsuei. Optimal Electron Doping of a  $C_{60}$  Monolayer on Cu(111) via Interface Reconstruction. *Phys. Rev. Lett.*, **104**(3):036103, 2010.
- [235] F. E. Olsson, M. Persson, A. G. Borisov, J.-P. Gauyacq, J. Lagoute, and S. Fölsch. Localization of the Cu(111) Surface State by Single Cu Adatoms. *Phys. Rev. Lett.*, **93**(20):206803, 2004.
- [236] J. Lagoute, X. Liu, and S. Fölsch. Link between Adatom Resonances and the Cu(111) Shockley Surface State. *Phys. Rev. Lett.*, **95**(13):136801, 2005.
- [237] G. Schull and R. Berndt. private communication.
- [238] X. W. Tu, G. R. Mikaelian, and W. Ho. Controlling Single-Molecule Negative Differential Resistance in a Double-Barrier Tunnel Junction. *Phys. Rev. Lett.*, **100**(12):126807, 2008.
- [239] C. J. Chen. Tunneling matrix elements in three-dimensional space: The derivative rule and the sum rule. *Phys. Rev. B*, **42**(14):8841, 1990.
- [240] I. D. Hands, J. L. Dunn, and C. A. Bates. Calculation of images of oriented  $C_{60}$  molecules using molecular orbital theory. *Phys. Rev. B*, **81**(20):205440, 2010.
- [241] Robert L. Carter. *Molecular Symmetry and Group Theory*. John Wiley & Sons Inc., 1998.
- [242] X. H. Qiu, G. V. Nazin, and W. Ho. Vibronic States in Single Molecule Electron Transport. *Phys. Rev. Lett.*, **92**(20):206102, 2004.
- [243] Moon-Ho Jo, Jacob E. Grose, Kanhayalal Baheti, Mandar M. Deshmukh, Jennifer J. Sokol, Evan M. Rumberger, David N. Hendrickson, Jeffrey R. Long, Hongkun Park, and D. C. Ralph. Signatures of molecular magnetism in single-molecule transport spectroscopy. *Nano Lett.*, **6**(9):2014–2020, 2006.
- [244] H. B. Heersche, Z. de Groot, J. A. Folk, H. S. J. van der Zant, C. Romeike, M. R. Wegewijs, L. Zobbi, D. Barreca, E. Tondello, and A. Cornia. Electron Transport through Single  $Mn_{12}$  Molecular Magnets. *Phys. Rev. Lett.*, **96**(20):206801, 2006.
- [245] Nicolas Roch, Serge Florens, Vincent Bouchiat, Wolfgang Wernsdorfer, and Franck Balestro. Quantum phase transition in a single-molecule quantum dot. *Nature*, **453**:633–637, 2008.
- [246] Sebastian Loth, Susanne Baumann, Christopher P. Lutz, D. M. Eigler, and Andreas J. Heinrich. Bistability in Atomic-Scale Antiferromagnets. *Science*, **335**(6065):196–199, 2012.

# List of Figures

1.1	The energy levels without and with the $s - d$ mixing . . . . .	7
1.2	Schematics of the Kondo ground state and spin-flip process . . . . .	9
1.3	The spectral function of a Kondo impurity at $T = 4$ K . . . . .	10
1.4	Kondo temperature and $J$ of transition elements in gold and copper . . . . .	11
1.5	Schematic of a single-electron transistor and the zero-bias ASK resonance . . .	12
1.6	Schematics of a break junction and $dI/dV$ spectra at various temperatures . .	13
1.7	Calculated splitting of the Kondo resonance under a magnetic field . . . . .	15
1.8	Zeeman splitting of a molecular Kondo device . . . . .	16
1.9	Schematics and conductance curves of a Ni-C <sub>60</sub> -Ni break junction at $T = 1.5$ K	17
1.10	Schematics of magnetic interactions . . . . .	19
1.11	DOS in the case of an AFM interaction among two Kondo impurities . . . . .	21
1.12	Resonance splitting and restoring in a magnetic field . . . . .	22
2.1	UHV system and facility . . . . .	26
2.2	STM schematic diagram . . . . .	27
2.3	Homebuilt molecular and metal evaporators . . . . .	29
2.4	Energy diagram for positive and negative bias applied respect to the sample . .	31
2.5	Schematics of the experiment setup . . . . .	32
2.6	Constant-current topography and chemical structure of CoPc . . . . .	33
2.7	Broadening functions in STM . . . . .	35
2.8	$dI/dV$ with constant-current and constant-height modes . . . . .	36
2.9	$dI/dV$ spectra of Co atom on various copper surfaces . . . . .	37
2.10	$T_K$ and $\epsilon_K$ as a function of the occupation of d level $n$ . . . . .	38



2.11 Schematic of the tunneling paths with a magnetic impurity on a non-magnetic surface . . . . .	39
2.12 Simulated Fano line shapes for different values of $q$ . . . . .	40
2.13 Differential conductance of a Kondo impurity for different $M_{at}$ . . . . .	41
2.14 Kondo resonance measured on Co dimers on Cu(100) and $\text{CoCu}_n\text{Co}$ chains on Cu(111) . . . . .	43
3.1 Schematics of a diffusive and a ballistic transport . . . . .	46
3.2 Conductance quantization in an atomic-sized conductor between two electrodes (tip and sample). . . . .	47
3.3 Transmission probability as a function of $\Gamma_L/\Gamma_R$ . . . . .	48
3.4 Current as a function of the tip displacement . . . . .	50
3.5 Conductance versus tip displacement of Cu atom on a Cu(111) surface . . . . .	51
3.6 The collapse of the tunnel barrier and the calculated conductance . . . . .	53
3.7 Atomic relaxations near point contact . . . . .	54
3.8 $dI/dV$ above Co nanoislands of increasing size . . . . .	55
3.9 Evolution of the conductance on Co atom-Cu(100) . . . . .	57
3.10 Evolution of the ASK resonance on Co atom-Cu(100) . . . . .	58
3.11 ASK resonance from transition to contact . . . . .	59
3.12 Evolution of the Kondo temperature on Co atom-Cu(100) . . . . .	61
3.13 Density of $d$ states of a Co adatom on Cu(100) for different tip displacements . . . . .	62
3.14 Relative coupling $\Gamma_t/\Gamma_s$ for various tips . . . . .	63
3.15 Electron density of Cu and Co adatoms on Cu(100) . . . . .	64
3.16 Time resolved two-level fluctuations of the conductance and $T_{\text{eff}}$ . . . . .	67
3.17 Simulation of $T_{\text{eff}}$ and Frota fitting of the ASK resonance as a function of bias . . . . .	68
3.18 $dI/dV$ acquired with increasing bias ranges . . . . .	69
4.1 Schematics of the density of states (DOS) and spin-polarized tunneling in a parallel and antiparallel alignment of the magnetizations of two FMs . . . . .	72
4.2 Schematics of spin-polarized transport for parallel and antiparallel alignments of FMs in GMR devices . . . . .	73
4.3 The density of states in a ferromagnet . . . . .	74
4.4 Spin junction at the interface of a cobalt FM and a copper NM . . . . .	76

4.5	Engineering a single-atom junction . . . . .	78
4.6	ASK resonance in the presence of a spin-polarized current . . . . .	80
4.7	$T_K$ versus current for a WCu tip and evolution of $dI/dV$ spectra for a FeCu tip . . . . .	81
4.8	$\Delta$ versus current . . . . .	82
4.9	Schematics of a spin polarized transport for parallel and anti-parallel alignments of FMs in GMR devices . . . . .	84
4.10	ASK resonance in the presence of a spin-polarized current and ferromagnetism . . . . .	85
4.11	Relative coupling $\Gamma_t/\Gamma_s$ for pristine Ni tips . . . . .	86
4.12	Illustration of $H_s$ and $H_{FM}$ showing how ASK resonance changes and theoretical simulation of the differential conductance . . . . .	87
4.13	Theoretical simulation of the differential conductance in the presence of a spin-polarized current . . . . .	88
4.14	Schematics of the junction employed and $dI/dV$ spectrum in comparison with Pasupathy <i>et al.</i> case . . . . .	90
4.15	Comparison with the experiment by Calvo <i>et al.</i> . . . . .	91
5.1	Top view of the $C_{60}$ structure, of the LUMO+1 isosurface and images of $C_{60}$ . . . . .	97
5.2	Topography before and after picking up the $C_{60}$ on the tip . . . . .	99
5.3	Topography and spectroscopy using a metallic and a $C_{60}$ terminated tip . . . . .	100
5.4	$dI/dV$ over Cu(111) for various $C_{60}$ tips and counter image of Au atom . . . . .	102
5.5	$dI/dV$ spectra acquired with a $C_{60}$ -terminated tip and a copper-coated W tip . . . . .	103
5.6	$dI/dV$ acquired above Cu(111) with two different tips . . . . .	104
5.7	$dI/dV$ spectra for various barrier thicknesses and NDC intensity versus tip-sample distance . . . . .	105
5.8	WKB simulation of DOS, $dI/dV$ and energy-resolved current . . . . .	107
5.9	Counter image using a $C_{60}$ terminated tip . . . . .	110
5.10	Conductance versus tip displacement of a Co adatom/Cu(100) using a pentagon oriented $C_{60}$ tip . . . . .	111
5.11	Tunneling spectrum of a Co adatom using an hexagon-oriented $C_{60}$ tip . . . . .	112
5.12	Evolution of the $dI/dV$ spectra of a Co adatom in contact with $C_{60}$ tip from transition to contact . . . . .	114



## Curriculum Vitae

### Personal

Born on July 14<sup>th</sup>, 1985.

### Education

- 12/2008-06/2012 Ph.D. in Department of Physics and Chemical physics  
Institut de Physique et Chimie des Matériaux de Strasbourg (IPCMS-CNRS),  
Université de Strasbourg, Strasbourg, France  
Thesis: *Kondo effect and detection of a spin-polarized current  
in a quantum point contact*
- 08/2007-12/2008 M.S. in Department of Physics  
Ewha Womans University, Seoul, Korea  
Thesis: *Role of Interface Properties on Spin Polarized Tunneling  
in Magnetic Tunnel Junctions*
- 04/2004-08/2007 B.S. in Department of Physics  
Ewha Womans University, Seoul, Korea

### Awards and Honors

Master degree Academic Scholarship at Ewha Womans University, 2007-2008  
MAGNA CUM LAUDE, Awarded an honor graduate prize at Ewha Womans University, 2007  
Undergraduate Academic Scholarship at Ewha Womans University, 2004-2007

